U.S. Department of Transportation
Federal Railroad Administration

A Comparison of Model and Field Test Dynamic Performance Data for a Two-Axle Freight Car

Track Safety Research Division
Washington, DC 20590

D. N. Wormley
J. R. Bailey

Department of Mechanical Engineering
Massachusetts Institute of Technology
Cambridge, MA 02139

DOT/FRA/~~89~~-92/10
DOT-VNTSC-FRA-91-2

Final Report
January 1989

This document is available to the public through the National Technical Information Service, Springfield, VA 22161

03 - Rail Vehicles & Components

Technical Report Documentation Page

1. Report No.	2. Government Accession No.	3. Recipient's Catalog No.
4. Title and Subtitle A Comparison of Model and Field Test Dynamic Performance Data for a Two-Axle Freight Car		5. Report Date January 1989
		6. Performing Organization Code DTS-76
7. Author(s) D.N. Wormley and J.R. Bailey*		8. Performing Organization Report No. DOT-VNTSC-FRA-92-2
9. Performing Organization Name and Address U.S. Department of Transportation Research and Special Programs Administration John A. Volpe National Transportation Systems Center Cambridge, MA 02142		10. Work Unit No. (TRAIS)
		11. Contract or Grant No. DTRS-57-85-C-00102TTD4
12. Sponsoring Agency Name and Address U.S. Department of Transportation Federal Railroad Administration Track Safety Research Division Washington, DC 20139		13. Type of Report and Period Covered Final March 1988 - November 1988
		14. Sponsoring Agency Code RRS-31

15. Supplementary Notes

*Department of Mechanical Engineering
Massachusetts Institute of Technology
Cambridge, MA 02142

16. Abstract

A microcomputer based simulation has been developed for predicting the safety related dynamic performance of rail cars. The simulation has been implemented specifically for a two-axle rail vehicle. Model data for test scenarios prescribed by the Association of American Railroads' (AAR) Chapter XI requirements have been compared with experimental test data obtained for the vehicle in hunting, steady-state curving vertically perturbed track, laterally perturbed track, and dynamic curving tests. The simulation model and test data are in excellent agreement for vehicle response to vertical track perturbations. In the response to lateral perturbations and in curving, the general trends of the model and test data are similar. The test and model data are in good agreement in identification of operating conditions approaching safety limits.

17. Key Words Rail Vehicle Dynamics Rail Vehicle Safety		18. Distribution Statement DOCUMENT IS AVAILABLE TO THE PUBLIC THROUGH THE NATIONAL TECHNICAL INFORMATION SERVICE, SPRINGFIELD, VA 22161	
19. Security Classification (of this report) UNCLASSIFIED	20. Security Classification (of this page) UNCLASSIFIED	21. No. of Pages 160	22. Price

Form DOT F 1700.7 (8/72) Reproduction of this completed page authorized

Preface

The research described in this report compares experimentally obtained test data on a two-axle rail vehicle with computer simulation models to assess the current capabilities of rail vehicle dynamic simulations. The research has been supported by the Federal Railroad Administration with direct technical monitoring of the research performed by the Transportation Systems Center. The research has drawn on the cooperation of a number of individuals and organizations. Experimental data for the comparisons has been provided by the Association of American Railroads under contract to the Federal Railroad Administration. Mr. John Elkins and Mr. Nicholas Wilson were extremely helpful in providing data and interpreting the data from the field tests on the two-axle vehicle. Additionally, Dr. Fred Blader of TRANSANGLE was very helpful in determining the fidelity of the computer simulation model used in this report.

The authors also wish to acknowledge Dr. Herbert Weinstock of the Transportation Systems Center, who was the Technical Monitor for the research and provided significant technical direction, and Mr. Richard Scharr, of the Federal Railroad Administration, who established the research objectives and successfully coordinated the effort among the participating organizations.

The authors are indebted to all the individuals cited. The successful accomplishment of the research tasks would not have been possible without the cooperation of this wide range of individuals.

METRIC / ENGLISH CONVERSION FACTORS

ENGLISH TO METRIC

LENGTH (APPROXIMATE)

1 inch (in) = 2.5 centimeters (cm)
1 foot (ft) = 30 centimeters (cm)
1 yard (yd) = 0.9 meter (m)
1 mile (mi) = 1.6 kilometers (km)

AREA (APPROXIMATE)

1 square inch (sq in, in^2) = 6.5 square centimeters (cm^2)
1 square foot (sq ft, ft^2) = 0.09 square meter (m^2)
1 square yard (sq yd, yd^2) = 0.8 square meter (m^2)
1 square mile (sq mi, mi^2) = 2.6 square kilometers (km^2)
1 acre = 0.4 hectares (he) = 4,000 square meters (m^2)

MASS - WEIGHT (APPROXIMATE)

1 ounce (oz) = 28 grams (gr)
1 pound (lb) = .45 kilogram (kg)
1 short ton = 2,000 pounds (lb) = 0.9 tonne (t)

VOLUME (APPROXIMATE)

1 teaspoon (tsp) = 5 milliliters (ml)
1 tablespoon (tbsp) = 15 milliliters (ml)
1 fluid ounce (fl oz) = 30 milliliters (ml)
1 cup (c) = 0.24 liter (l)
1 pint (pt) = 0.47 liter (l)
1 quart (qt) = 0.96 liter (l)
1 gallon (gal) = 3.8 liters (l)
1 cubic foot (cu ft, ft^3) = 0.03 cubic meter (m^3)
1 cubic yard (cu yd, yd^3) = 0.76 cubic meter (m^3)

TEMPERATURE (EXACT)

$[(x - 32)(5/9)]\,°F = y\,°C$

METRIC TO ENGLISH

LENGTH (APPROXIMATE)

1 millimeter (mm) = 0.04 inch (in)
1 centimeter (cm) = 0.4 inch (in)
1 meter (m) = 3.3 feet (ft)
1 meter (m) = 1.1 yards (yd)
1 kilometer (km) = 0.6 mile (mi)

AREA (APPROXIMATE)

1 square centimeter (cm^2) = 0.16 square inch (sq in, in^2)
1 square meter (m^2) = 1.2 square yards (sq yd, yd^2)
1 square kilometer (km^2) = 0.4 square mile (sq mi, mi^2)
1 hectare (he) = 10,000 square meters (m^2) = 2.5 acres

MASS - WEIGHT (APPROXIMATE)

1 gram (gr) = 0.036 ounce (oz)
1 kilogram (kg) = 2.2 pounds (lb)
1 tonne (t) = 1,000 kilograms (kg) = 1.1 short tons

VOLUME (APPROXIMATE)

1 milliliter (ml) = 0.03 fluid ounce (fl oz)
1 liter (l) = 2.1 pints (pt)
1 liter (l) = 1.06 quarts (qt)
1 liter (l) = 0.26 gallon (gal)
1 cubic meter (m^3) = 36 cubic feet (cu ft, ft^3)
1 cubic meter (m^3) = 1.3 cubic yards (cu yd, yd^3)

TEMPERATURE (EXACT)

$[(9/5)\,y + 32]\,°C = x\,°F$

QUICK INCH-CENTIMETER LENGTH CONVERSION

INCHES	0	1	2	3	4	5	6	7	8	9	10

CENTIMETERS 0 1 2 3 4 5 6 7 8 9 10 11 12 13 14 15 16 17 18 19 20 21 22 23 24 25 | 25.40

QUICK FAHRENHEIT-CELCIUS TEMPERATURE CONVERSION

°F	-40°	-22°	-4°	14°	32°	50°	68°	86°	104°	122°	140°	158°	176°	194°	212°
°C	-40°	-30°	-20°	-10°	0°	10°	20°	30°	40°	50°	60°	70°	80°	90°	100°

For more exact and/or other conversion factors, see NBS Miscellaneous Publication 286, Units of Weights and Measures. Price $2.50. SD Catalog No. C13 10 286.

Table of Contents

List of Figures

List of Tables

Executive Summary

The objective of this study has been to develop analysis tools for predicting the safety related performance of rail cars. An analytical framework has been developed for simulating rail vehicle response to extreme track conditions, including those prescribed by the Association of American Railroads' (AAR) in Chapter XI of Reference [1]. The analysis has been implemented for a prototype two-axle, trailer-on-flat-car rail vehicle, which has been tested extensively over Chapter XI track conditions at the AAR Transportation Test Center.

Computer simulations of the unloaded vehicle, for which a complete set of vehicle parameters has been determined by the AAR from component tests, have been compared directly with field test results. Additionally, both the model and field data have been reviewed to identify potentially unsafe conditions. The results of the comparisons for the unloaded baseline vehicle, where the simulations are based upon track representations using measured track data are summarized below:

(1) Hunting - Field tests on tangent track identified no hunting in tests up to 90 mph, while simulations indicated that hunting commenced above 105 mph. Simulations have indicated a decrease in hunting speed to 35 mph when the hydraulic longitudinal suspension yaw damper is reduced to 25-percent effectiveness.

(2) Steady-State Curving - Field tests on constant radius curved track have indicated maximum wheel lateral-to-vertical force (L/V) ratios of 0.1, 0.51, and 0.6 on 5 degree, 7.5 degree and 10 degree curves, respec-

tively, while simulations for these degree curves indicated L/V ratios of 0.05, 0.36, and 0.51 respectively. The trends of field test and simulation wheel L/V ratios with respect to speed are similar. Additional simulations have indicated maximum wheel L/V ratios of less than 0.6 for baseline wheel-rail conditions for curves from 5 to 15 degrees. They have also shown that changes in rail conditions from new to worn may change L/V ratios measurably in a manner similar to that observed in the field tests.

(3) Yaw-Sway on Track with 39 Foot Wavelength, 1.25-Inch Amplitude Sinusoidal Perturbations - Field tests conducted at speeds of10 mph to 80 mph on laterally perturbed track indicated a maximum axle L/V ratio of 0.95, while corresponding simulations indicated a maximum axle L/V ratio of 0.98 at these speeds. Additionally, simulations for 78-ft wavelength perturbations indicated axle L/V ratios of less than 1.0 at 20 mph to 70 mph but a ratio of 1.3 at 80 mph.

(4) Dynamic Curving on Curved Track with Alignment and Crosslevel Perturbations - In field tests axle L/V ratios above 1.35 were reached at speeds between 20 mph and 23 mph, the speed at which the tests were terminated. In corresponding simulations, axle L/V ratios above 1.2 were reached at 23 mph and severe wheel climb approaching derailment occurred at 26 mph.

(5) Rock and Roll on Track with 0.75-Inch Crosslevel Perturbations - In field tests conducted on track with crosslevel perturbations at speeds of 36 mph to 60 mph, a maximum carbody roll angle of 2.1 degrees was

measured. In simulations conducted at speeds of 15 mph to 75 mph, a maximum carbody roll angle of 2.2 degrees was computed.

(6) Bounce and Pitch on 0.75-Inch Amplitude 39 Foot In-Phase Vertical Perturbations - Both field tests and simulations indicated that on vertical perturbed track wheel unloading increased as vehicle speed increased. At 70 mph, full wheel unloading occurred for short periods of time corresponding to 3 feet of travel.

(7) Bounce and Pitch in Negotiation of a Single 2-Inch Vertical Bump - Field tests over a single vertical bump have shown that full wheel unloading occurs momentarily at speeds above 38 mph, while corresponding simulations have indicated that at speeds above 40 mph full wheel unloading occurs for short time periods corresponding to a travel distance of approximately 4 feet.

Overall, the baseline vehicle model closely agrees with field tests conducted on vertical and crosslevel track perturbations thereby validating the representation of the vehicle vertical suspension and carbody mass and inertial characteristics. The model also has good agreement with field data in predicting trends and identifying conditions approaching wheel climb derailments for conditions exciting lateral motions through wheel-rail interactions. However, the lateral plane model does not closely agree with several specific test measurements including the lateral suspension stroke in sinusoidal alignment tests and wheelset angular alignment in the 10-degree curve. These conditions have been shown to be very sensitive to the wheel-rail profile and friction coefficient.

Both the analysis and test data identified only one set of conditions, dynamic curving where tests were stopped at 23 mph under which a potential wheel climb derailment was approached. Under these conditions, cars equipped with standard three-piece freight trucks would also be expected to experience severe wheel climb at the same speeds.

This study has illustrated the importance of complementary experimental and analytical evaluation of rail vehicle safety performance. Field tests are indispensible in vehicle evaluation but are necessarily limited by time and cost constraints. Thus, the tests represent the vehicle behavior for only the specific set of conditions which exist for the tests. Analyses are valuable to explore vehicle operating conditions which are not tested and may result from changes in vehicle characteristics, wheel-rail profiles, or track conditions not available for tests. The study scope has been limited to unloaded vehicle tests and simulations which correspond to relatively small wheel loads. It is recommended that further effort be undertaken to conduct detailed comparisons of test and simulation data for fully loaded vehicles so that simulation model validity may be assessed over the complete range of wheel loads occurring in the rail industry.

1. INTRODUCTION

1.1 BACKGROUND

A significant number of new freight car designs have been developed in the last few years to provide improved productivity in the rail industry, particularly for intermodal transport. The increased rate at which new types of cars are being introduced requires the ability to assess the safety related dynamic performance of new cars critically and rapidly.

The Federal Railroad Administration (FRA) is conducting research to develop analytical and experimental techniques to aid in the assessment of the safety related performance of new types of rail vehicles. The following efforts have been conducted over the past five years in cooperation with the Association of American Railroads (AAR) to develop criteria for the evaluation of new types of vehicles:

(1) Establishment of Recommended Safety Test Conditions [1]

(2) The Vehicle/Track Interaction Assessment Program [2]

(3) Perturbed Track Tests on Freight Locomotives [3]

(4) Track Geometry Specification Research [4,5]

(5) Vehicle Safety Tests on Two-Axle Vehicles [6]

The evaluation of vehicle safety requires a combined analytical and experimental approach. Tests conducted on a vehicle on any given day represent an evaluation for a specific set of track conditions and vehicle state. Test results may be strongly influenced by the presence or lack of track lubrication, by the amount of wear on the rail head and wheels, and by many other factors. It is not economically feasible to test a vehicle over all possible operating scenarios. Thus, while track tests are indispensible to vehicle safety evaluation, they should be coupled with analytical studies which explore vehicle performance for sets of track and vehicle conditions representing potentially unsafe conditions which cannot be readily evaluated experimentally. For such analytical studies to be meaningful, analytical models which have been carefully validated by experimental data are required.

In the last two years, a combined analytical and experimental approach for assessing vehicle safety has been formulated by the AAR and described in Chapter XI [1]. The FRA has initiated a research program to evaluate the effectiveness of the specific analytical and experimental procedures described in Chapter XI. As a part of this evaluation, a light weight two-axle trailer on flat car was tested at the AAR Test Center over track conditions prescribed by Chapter XI. The results of the test series are described in [6]. As part of the effort to evaluate the capabilities of analytical models to predict vehicle safety performance, the FRA has sponsored, through the Transportation Systems Center, the research compiled in this report.

1.2 STUDY OBJECTIVES

The general objective of the study is to establish experimentally validated analysis tools for evaluation of the safety related performance of rail cars. The scope of the effort is focused on the dynamic performance of a single car, and specifically considers the safety related dynamic performance resulting from vehicle-track interactions. Specific objectives of the work are

(1) Formulation of a general framework for rail vehicle state-of-the-art dynamic modeling

(2) Implementation of a dynamic model for the two-axle vehicle operating on perturbed track

(3) Assessment of the model validity and limitations using test data obtained on the car operating over Chapter XI track scenarios

(4) Determination of the dynamic safety related performance of two-axle vehicles

(5) Formulation of recommendations with respect to evaluation methodologies for vehicle dynamic safety related performance

The overall objective of the study is to provide information to assess the safety performance of a wide variety of rail vehicles. In this study, the specific evaluation of the two-axle freight vehicle is used to illustrate the critical areas which must be addressed during the performance evaluation of a new vehicle.

1.3 SAFETY EVALUATION METHODOLOGY

1.3.1 Vehicle-Track Interactions

Under extreme conditions, the interactions between a rail vehicle and the track can lead to a number of potentially unsafe conditions including:

(1) Incipient derailment in which either a flanging wheel climbs the rail (wheel climb) or a nonflanging wheel displaces sufficiently to drop off the rail (wheel drop).

(2) Large vehicle motions in which carbody displacements are sufficient for the carbody to hit wayside obstacles or another vehicle, to cause separation between the carbody and truck, or to result in permanent damage to car or track components.

The propensity to approach an unsafe condition is a strong function of car characteristics including load, wheel profile, and suspension characteristics; track conditions including curvature, superelevation, track perturbations, and the presence or absence of lubrication and operating conditions including speed and location of a car in the train consist. Unsafe conditions may result from single events, such as when a car encounters an isolated track perturbation sufficient to cause derailment, or from a series of events, such as when a periodic track perturbation excites a vehicle at resonance and leads to carbody motions either sufficiently large to hit an obstruction or derailment. In both single and multiple event cases, the potential to reach an unsafe condition is a result of the combination of car characteristics, track characteristics, and operating conditions.

To assess car safety using a finite set of analytical and experimental studies requires:

(1) The quantitative definition of a set of safety criteria which indicate incipient unsafe conditions and which can be practically measured and computed, and

(2) The definition of a set of safety evaluation scenarios which can define the car safety boundaries for the critical combinations of car characteristics, track charateristics, and operating conditions leading to unsafe conditions.

A number of analytical and experimental studies have been performed to develop both safety criteria and test scenarios [1-6]. A recent document, Chapter XI of the AAR Manual of Standards and Recommended Practice [1], defines a set of quantitative safety criteria and a set of experimental test scenarios and analytical studies to assess car safety performance. Sections 1.3.2 and 1.3.3 discuss the available data and studies relating to safety criteria and safety evaluation scenarios.

1.3.2 Safety Criteria

Incipient derailment may result from wheel drop or wheel climb conditions. In the first condition, derailment occurs because the wheelset has displaced a sufficient lateral distance for the wheel to drop off the rail. This condition is usually associated with sections of track in which the track gage has increased or lateral restraint has decreased because of repeated vehicle loading or environmental conditions. The potential for wheel drop has been considered by F. B. Blader and G. L. Mealy [5], who have defined an incipient wheel drop condition as one in which the inward displaced wheel has less than 1.25-inch overlap with the supporting rails. Thus, any combination of dynamic wheel motion and track gage changes which allow wheel-track overlaps of less than 1.25 inches are considered unsafe. The specific maximum lateral wheel displacement allowable before wheel drop depends upon the wheel profile and the track gage and profile. For a standard AAR wheel and AREA rail with a gage of 59 inches, the wheelset may be displaced 1.5 inches before incipient wheel drop. A significant consideration in assessing wheel drop is the dynamic gage widing due to vehicle loading.

An experimental study [4] of gage spreading on perturbed, curved track and its influence on wheel drop conditions has shown that large lateral forces are generated at low speeds in tight radius curves (12-degree curves) which are relatively insensitive to vehicle velocity at speeds of 5 mph to 20 mph. Additionally, significant lateral forces resulting from crosslevel and alignment variations in curved track, were measured. Thus, potential wheel drop conditions may be expected on curved, perturbed track when large lateral gage spreading forces combine with significant lateral wheelset displacements.

Wheel climb derailments result when a flanging wheel has sufficient lateral force to climb over the rail. As the wheel climbs the rail, usually due to the combination of reduced vertical force and increased lateral force, it reaches a point of maximum angle between the plane of flange-rail contact and the track. Further displacements reduce this angle and eventually lead to derailment. The wheel displacement at the maximum contact angle has been proposed as the limit of displacement for incipient derailment [5,7]. Under field conditions, the small displacements of the wheel relative to the track are difficult to measure; however, lateral and vertical wheel forces can be measured with instrumented wheelsets and wayside measurements. Thus, practical indicators of wheel climb derailment have generally been expressed in terms of the wheel lateral-to-vertical force (L/V) ratio. A number of analytical [5,7] scale model [8] and full-scale field test [4,9,10] studies of the relationship of wheel L/V ratios to incipient derailment have been conducted. A recent review of work has been performed by H. Weinstock [7], who has concluded that a good measure of incipient wheel climb derailment is provided by the instantaneous wheel L/V ratio. The study described in [7] concluded that wheel climb derailment will not occur if any of the following criteria are met:

(1) The L/V ratio on each wheel is less than Nadal's limit.

(2) The sum of the magnitudes of L/V ratios for both wheels on an axle is less than 1.0.

(3) For the case in which the flanging wheel vertical force is less than the nonflanging wheel vertical force, the sum of the magnitudes of L/V ratios for both wheels on the axle is less than the sum of Nadal's limit and the coefficient of friction.

(4) For the case in which the lateral forces on both wheels are in the same direction (a negative angle of attack), the sum of the two wheel L/V ratios for the axle is less than the sum of Nadal's limit and the coefficient of friction.

Criterion (1) represents the classical Nadal's limit, which is appropriate for large effective angle of attack conditions (greater than 1.0 degree). Criteria (2) and (3) represent modifications to Nadal's limit which correct for the conservative nature of Nadal's limit at small positive effective angles of attack, and criterion (4) is formulated for negative effective angles of attack. Most of the scenarios in which wheel climb derailment is considered represent flanging wheel lift, and the vertical force on the flanging wheel is less than the vertical force on the non-flanging wheel. For these cases, criterion (3) is appropriate. Thus for a large number of cases of interest, if the sum of magnitudes of wheel L/V ratios on the axle is less than the sum of Nadal's limit and the coefficient of friction, a wheel climb derailment is not imminent. For a typical U.S. freight car wheelset with a maximum wheel-rail flange contact angle of 65 degrees operating under conditions of varying friction, the sum of L/V magnitude ratios is tabulated as below:

Sum of L/V Magnitudes	Friction Coefficient
1.75	0.1
1.42	0.3
1.30	0.5
1.28	0.7

The limiting values of the sum of L/V magnitudes increase as the friction coefficient decreases. Thus, if a criterion for a friction coefficient of 0.5 is selected as 1.3, the criterion is conservative for conditions with lower friction coefficients.

It is noted that Chapter XI [1] recommends a derailment wheel climb criterion in which the sum of L/V magnitudes is less than 1.3. While this criterion is applicable and conservative for most derailment scenarios of interest, it would not be conservative for cases in which the flanging wheel vertical load is greater than the nonflanging wheel vertical load. For those cases, alternative criteria such as those described in criteria (1) and (2) are appropriate.

Large vehicle motions leading to the vehicle hitting wayside obstructions or other vehicles, to separation of the carbody from the truck, or to damage of car and track components can result from a number of conditions. The establishment of vehicle safety performance criteria in terms of limits to excessive motions during the safety analysis and testing of a car are dependent upon specific car geometry. For example, the motion envelope which can be allowed to avoid wayside obstructions can be established [11]; however, the roll motion limits of a specific vehicle to remain within the envelope are vehicle specific. Additionally, the motions permitted to avoid car-truck separation and excessive vehicle forces are somewhat vehicle dependent. Thus, while detailed criteria must be somewhat vehicle specific, these criteria can be established from consideration of the operating envelope, car-truck separation effects, and excessive forces leading directly to damage.

1.3.3 Test Scenarios and Evaluation Criteria

A defined set of analytical and experimental test conditions and criteria must be established to evaluate the safety performance of a new vehicle critically and rapidly. The number of analyses and tests performed to qualify the safety performance of a new car are limited by both cost and time considerations. Thus, a finite set of test scenarios must be identified which can identify the limits to safety considering the range of vehicle conditions, track conditions, and operating conditions which may occur in practice. Because only limited field testing is feasible, a general goal is first to use critical field tests to establish performance limits of the most critical conditions and then to use analyses which have been confirmed by the field tests to explore conditions which have not been tested and to evaluate the potential for nontested conditions to represent potential problems. As a part of test planning, analyses can provide information concerning the sensitivity of performance to the variations in vehicle parameters expected from vehicle to vehicle in a fleet or as a vehicle has been in service over time. Thus, while it is not possible to conduct field tests for all conditions, a carefully selected set of critical field tests coupled with comprehensive analytical studies can provide a meaningful safety evaluation of new cars.

Efforts to develop a set of critical test scenarios and safety criteria for new cars have been described in the analytical study referenced in [5] and the experimental study referenced in [4] which together with historical field test data have been used to formulate the recommendations of Chapter XI [1].

The test scenarios described in Chapter XI include evaluation of the vehicle on:

(1) Unperturbed tangent track to identify the vehicle lateral stability limits in terms of hunting speed

(2) Unperturbed, spiral entry and constant radius curved track to identify wheel climb derailment propensity

(3) Vertically perturbed track with crosslevel perturbations which excite vehicle rock and roll to determine wheel unloading and maximum car roll angle which could lead to car-track separation or derailment

(4) Vertically perturbed track including a bump to represent grade crossings and a series of periodic in-phase perturbations to excite vehicle pitch and bounce near resonant conditions to determine whether excessive wheel unloading occurs

(5) Laterally perturbed track with periodic 39-foot sinusoidal alignment perturbations under a 1.0 inch wide gage condition. These perturbations are designed to excite vehicle lateral and yaw motions under resonant conditions to determine if wheel climb derailment conditions are approached.

(6) A condition with curved, perturbed track which has in-phase periodic perturbations in both gage and crosslevel to determine if either wheel climb derailment or excessive wheel unloading occurs.

The test scenarios in Chapter XI are designed to represent a combination of conditions which are expected to represent meaningful limits for safety evaluation. A set of tests can only practically evaluate a finite set of conditions. Thus, for a given vehicle, additional conditions to those specified may be important. For example, the yaw-sway tests are conducted only for track disturbances with 39-foot perturbations. For some vehicles, other wavelengths of track perturbation would represent more severe conditions. Thus, experimental tests need to be complemented with analytical studies to explore operating conditions and changes in the vehicle and track which are not represented in the specific safety tests conducted.

2. ANALYTICAL MODEL FORMULATION

2.1 CURRENT STATUS OF RAIL VEHICLE MODELING

In the past few years, several general purpose dynamic simulation programs have been developed for evaluation of rail vehicle dynamic performance. These efforts have built strongly on past work in which models have been developed for a specific vehicle or class of vehicles to assess hunting or curving or the response to track perturbations. Three general purpose programs are

(1) NUCARS, Association of American Railroads

(2) VAMPIRE, British Rail (BR)

(3) MEDYNA, Deutsche Forschungs und Versuchsanstadt fur Luft und Raumfahrt, Munich, West Germany

All three of these programs can construct a dynamic model of a rail vehicle from an assembly of car parts, suspension elements, and wheelsets. The programs contain a wheel-rail interaction model which computes wheel-rail forces and moments based upon Kalker's formulation [15]. These models can represent arbitrary wheel and track profiles and track lateral and longitudinal perturbations and thus are generally useful for evaluation of rail vehicles over a wide range of conditions. While these models are based upon the application of first principles in mechanics and dynamics and have produced results which have been compared with available test data, none have been fully validated in terms of the complete range of conditions approaching the limits to safety. Additionally, the programs currently have some limitations with respect to their ability to represent the types of friction which typically occur in U.S. freight vehicles. While the models represent the current state-of-the-art in rail vehicle modeling and have built strongly upon previous modeling efforts and model validation studies, further effort is still needed in the development of models validated for limiting wheel-rail conditions which occur as safety limits are approached.

In the current research effort, a model is formulated which, like those cited above, employs a state-of-the-art wheel-rail model. (The wheel-rail model is very similar to that utilized in NUCARS.) The current research model was developed in the same time period as NUCARS and VAMPIRE and reflects discussions held with AAR and BR researchers in its formulation. Thus, the model described in this report is representative of the current rail vehicle modeling capability, and the general results of the model are expected to be similar to those of the models cited.

2.2 CONCEPTUAL MODEL FORMULATION

A model has been formulated for a two-axle prototype vehicle tested by the AAR at the Pueblo Test Center. The model for the specific vehicle has been developed within a general model framework using a matrix equation formulation which can be used for the efficient development of models for a spectrum of rail vehicles.

The model framework has been developed specifically to meet a number of objectives. First, the model must represent vehicle dynamic performance in response to tangent and curved superelevated track containing vertical and alignment track perturbations. Second, the model must be valid for extreme conditions involving significant displacements of the vehicle suspension into contact with geometric stops and significant displacements of the wheels with respect to the rail requiring representation of wheel-rail mechanics under wheel climb conditions. Thus, a nonlinear model has been formulated to accurately represent large dynamic motions which occur at safety limits.

The model framework uses a general matrix equation formulation representing Newton's Law equating the sum of the forces on a mass to the mass times the acceleration which may be written in terms of the products of (1) a mass matrix and acceleration vector, (2) a damping matrix and velocity vector, (3) a stiffness matrix and displacement vector, and (4) a number of forces, as shown in the following equation:

$$M \ddot{X} + D \dot{X} + K X = WGW + FGF + FGI + FI + FC$$

The terms in this equation are defined as follows:

M: Mass matrix; contains all mass and moment of inertia terms on the diagonal

$\ddot{X}$: Second derivative of the degree of freedom vector; contains all the states' second derivatives

D: Structural damping matrix; contains damping values of flexible modes on the diagonal

$\dot{X}$: First derivative of degree of fredom vector; contains all the states' first derivatives

K: Structural stiffness matrix; contains stiffness values for the flexible modes on the diagonal

X: Degree of freedom vector; contains all the states

WGW: Weight vector; contains all weight forces

FG: Force geometry matrix; contains all geometry terms pertinent to calculating suspension forces and moments

F: Suspension force vector; contains suspension forces

FG1: Rail force vector; contains rail forces and torques

FI: Inertial force vector; contains purely geometric inertial forces (those that depend upon only track geometry)

FC: Cross term force vector; contains state rate/geometry coupling inertial force terms.

A specific vehicle model is implemented by defining the appropriate model state vector, the mass, the damping and stiffness matrices, and the system forces which represent nonlinear characteristics of wheel-rail interactions and suspension forces.

2.3 WHEEL-RAIL INTERACTION MODEL

Wheel-rail interaction models which represent nonlinear geometry, as well as nonlinear creep force-creepage relationships, have been developed and are currently used in many state-of-the-art models. Forces and torques developed for a wheelset are strongly influenced by local contact geometry,

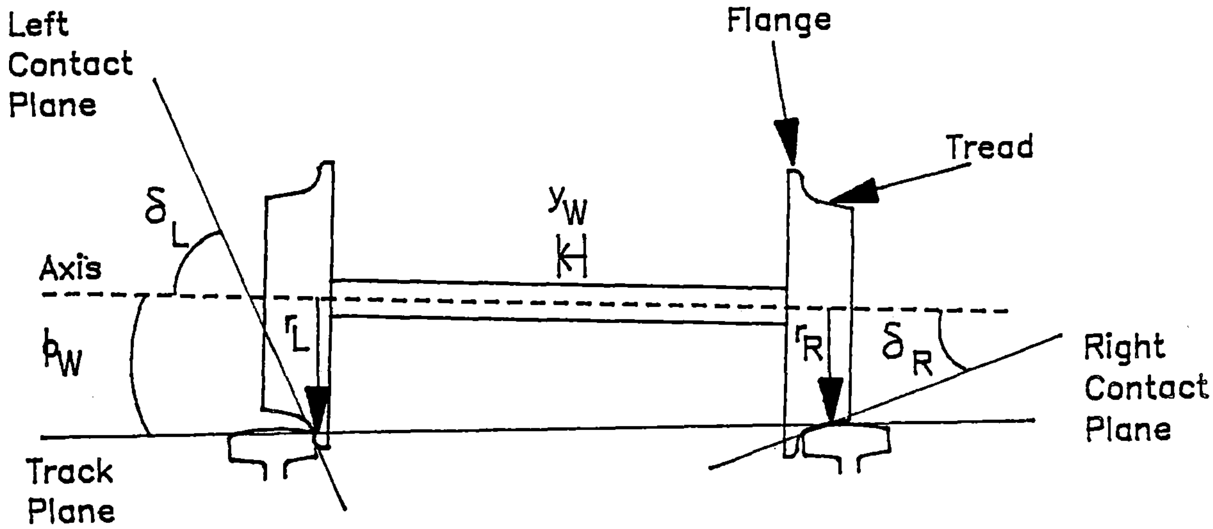

VIEW OF ROLLING RADII AND CONTACT PLANES

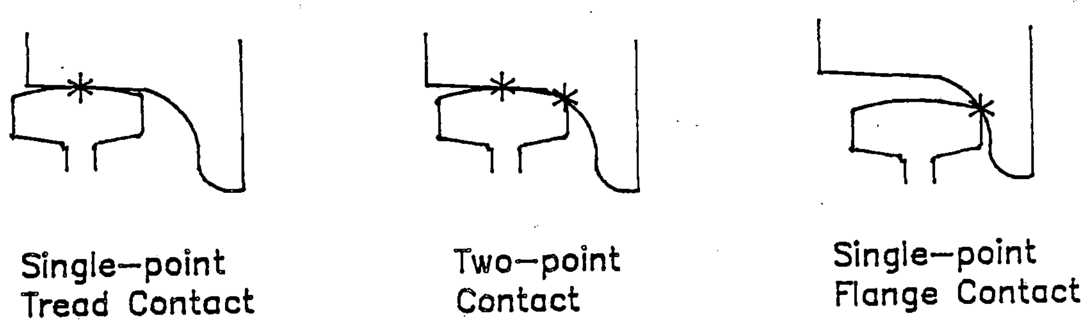

THREE REGIMES OF CONTACT

FIGURE 2-1. WHEEL/RAIL GEOMETRY

as well as by creep force-creepage relationships. As illustrated in Figure 2.1, a rigid wheelset may interact with a rail so that one or more points of contact occur between each wheel and the rail. The resulting contact area geometry depends upon both detailed wheel and track geometry and knowledge of the profiles is required to characterize the interaction. As a wheelset is displaced laterally, wheel-rail contact changes from the wheel tread region to the flange region, where multiple contact points may occur between the wheel and rail. As the flange is approached, significant changes in the contact geometry occur including the wheel rolling radius and the contact angle, as shown in Figures 2.2 through 2.5 respectively for AAR and CN Heumann (CNH) wheel profiles interacting with new rail and measured profiles on 5-degree and 10-degree curves at the Pueblo Test Center. The figures show that there are significant differences in rolling radius and contact angle at the same lateral excursion for the two profiles on new rails. Similarly, for the same CNH wheel profile interacting with new rail in the 5-degree curve and worn rail in the 10-degree curve, significant differences in rolling radius and contact angle occur for the same wheelset displacement. In the simulation model developed, tables of wheel-rail geometry as a function of wheelset displacements for a specific wheelset-rail condition are used to represent the detailed contact area geometry based upon the Hertzian solution to determine the contact area between two elastic bodies in contact.

The forces and torques generated by a wheelset interacting with a rail are a function of the local geometry and the contact patch constitutive relationship between lateral, longitudinal, and spin creep forces and creepages, i.e., local relative lateral, longitudinal and spin velocities in the contact area. The general form of the lateral creep force versus

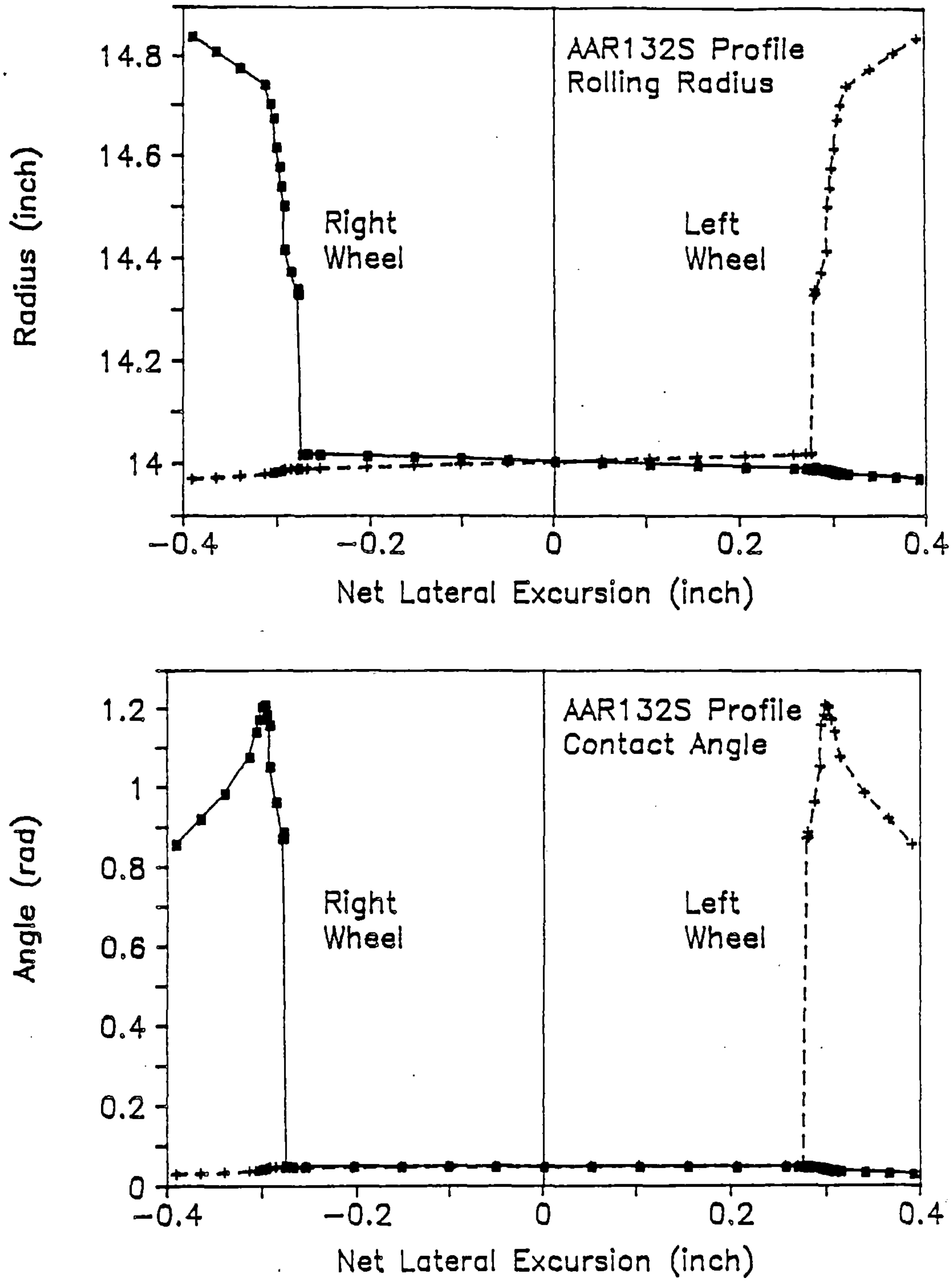

FIGURE 2-2. WHEEL-RAIL GEOMETRY FOR AAR 1.20 PROFILE ON NEW 132-LB RAIL

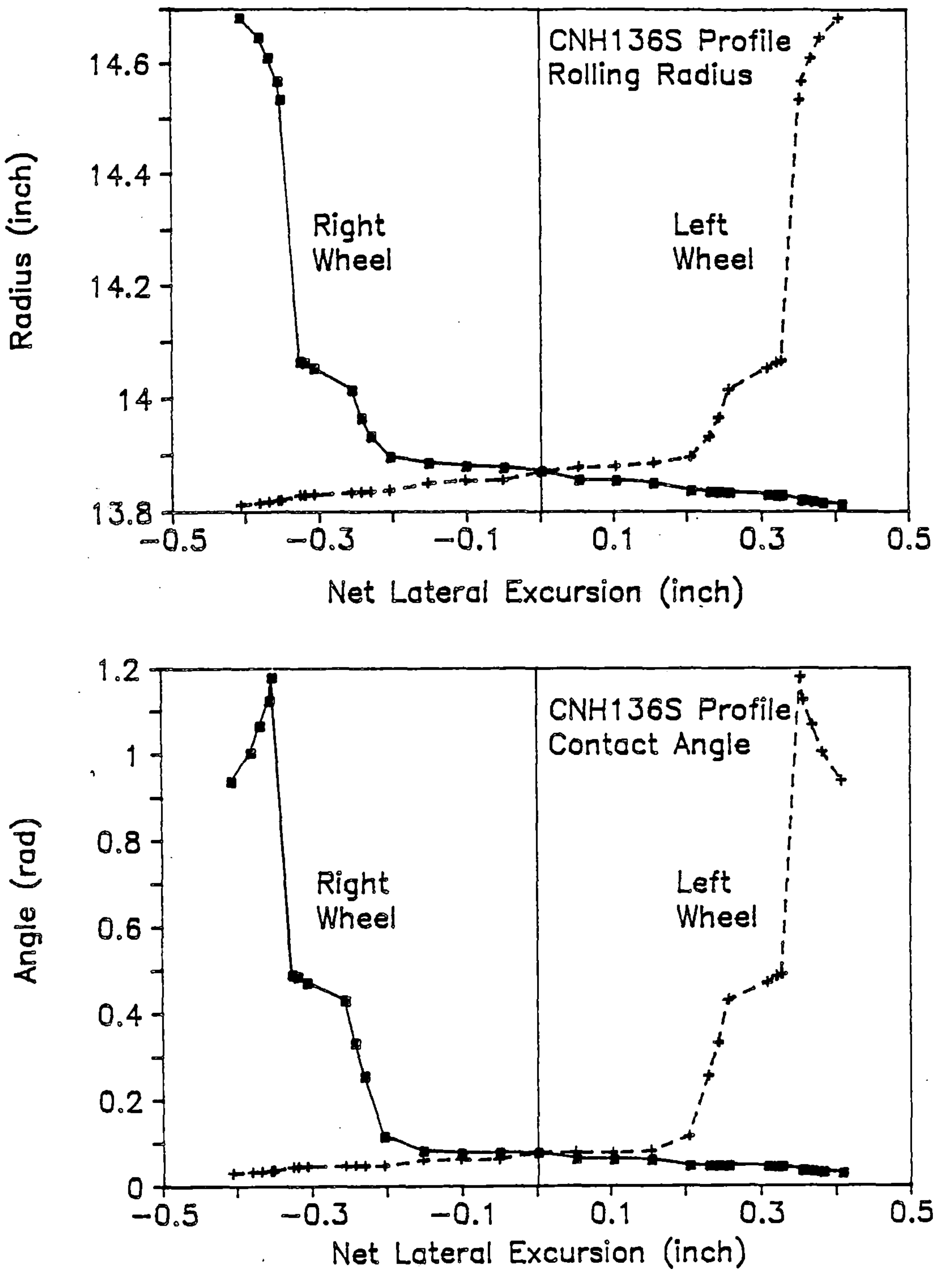

FIGURE 2-3. WHEEL-RAIL GEOMETRY FOR CN HEUMANN (CNH) PROFILE ON NEW 136-LB RAIL

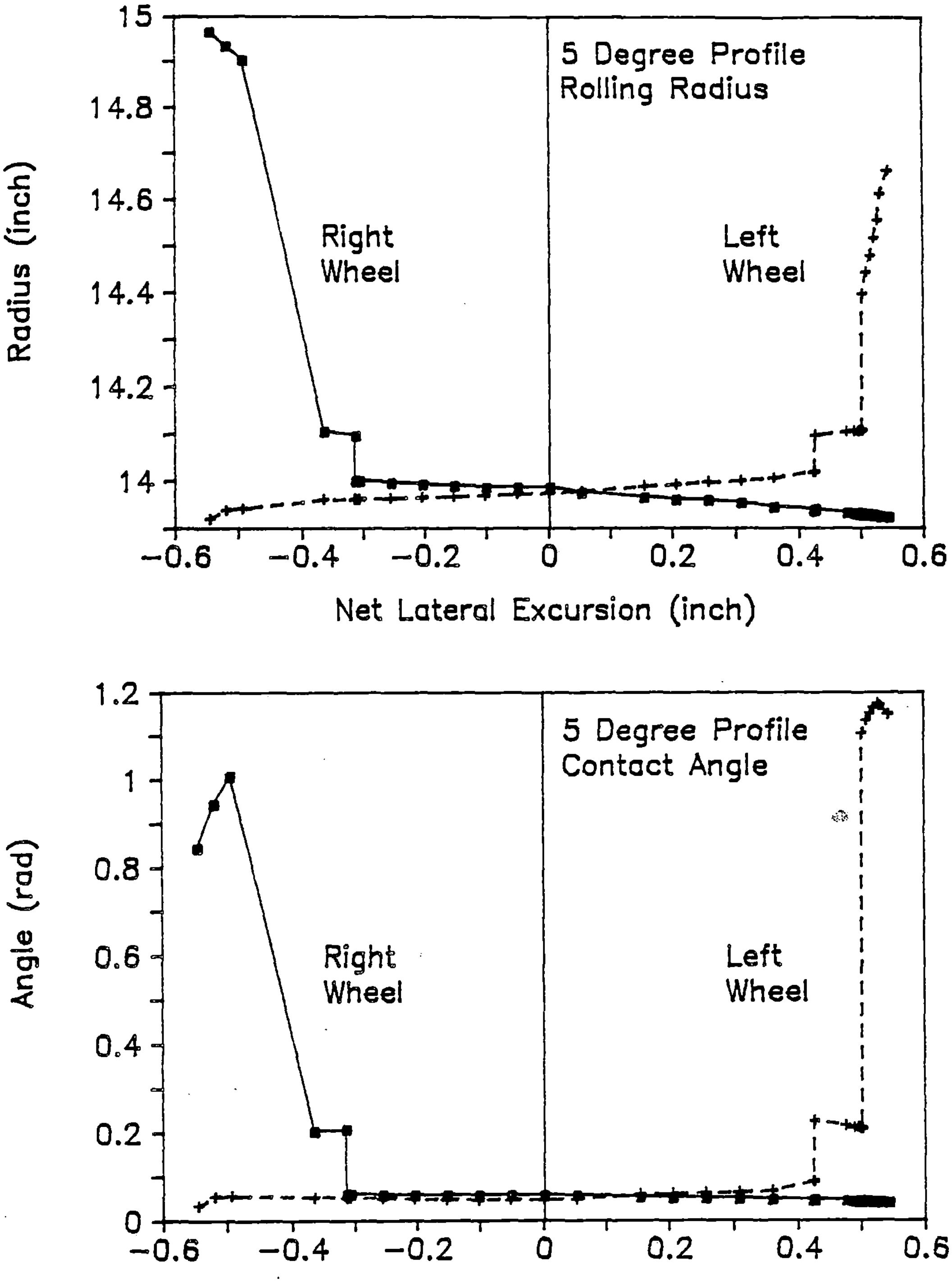

FIGURE 2-4. WHEEL-RAIL GEOMETRY FOR MEASURED PROFILE ON 5-DEGREE CURVE

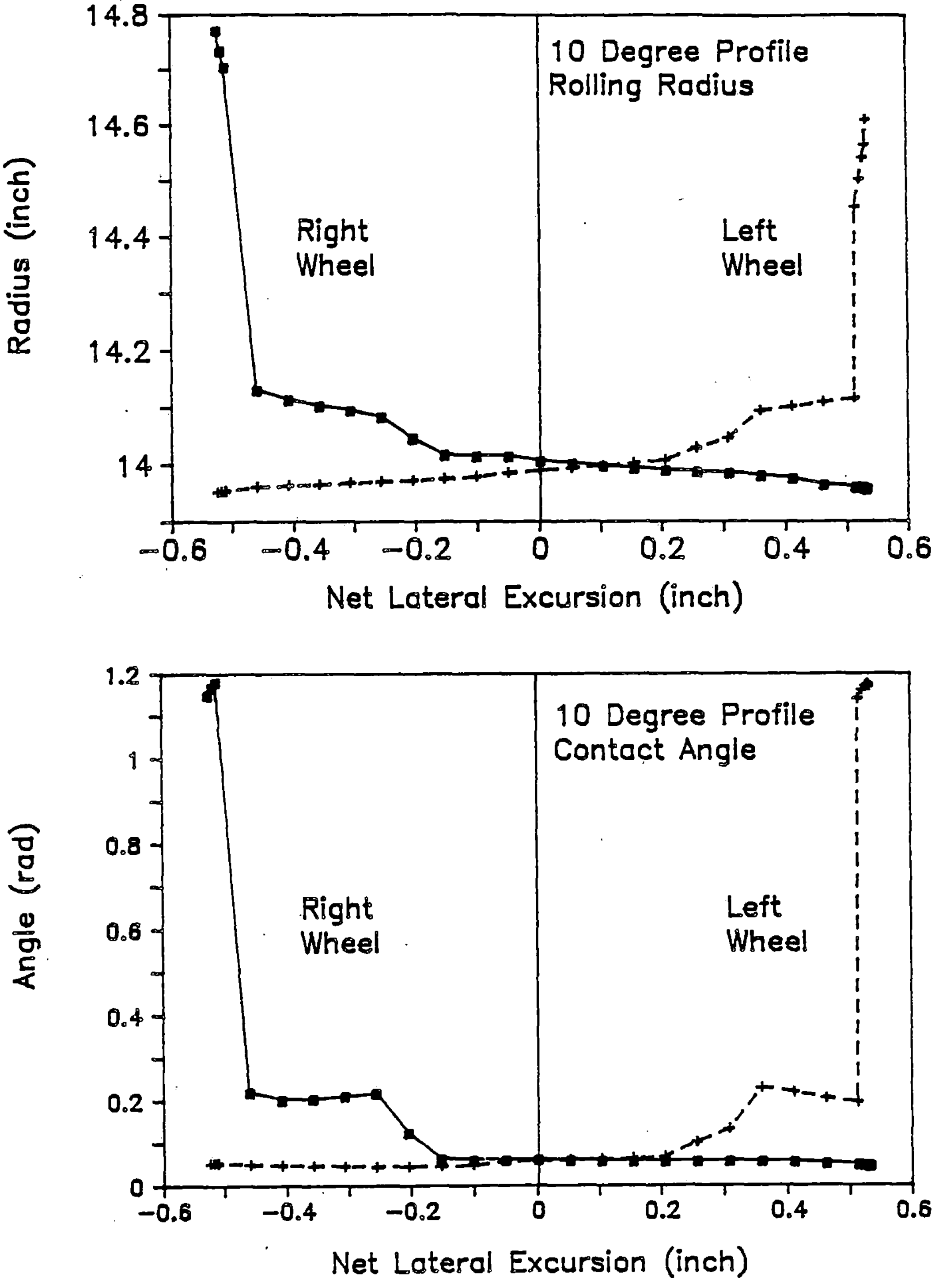

FIGURE 2-5. WHEEL-RAIL GEOMETRY FOR MEASURED PROFILE ON 10-DEGREE CURVE

lateral creepage shown in Figure 2.6 consists of an approximately linear relation between force and creepage, and as an increasing fraction of wheel slippage occurs, a constant saturation creep force is approached with full wheel slip. While the linear portion of the characteristic is generally represented as relatively independent of the sliding friction coefficient, in saturation with full slip, the creep force is a strong function of the sliding friction coefficient. A consistent formulation for computation of the creep forces has been developed by Kalker [15] with creep forces computed as a function of detailed wheel-rail contact geometry, as well as creepages ranging from zero to full slip. The Kalker representation (tables) is used in the model developed in this report with the detailed development of the equations described in Appendix B.

The role of geometry and friction in the generation of wheel-rail interaction forces is illustrated in Figures 2.7 and 2.8, which show the nondimensional moment on the wheelset versus P/W (the ratio of net lateral wheelset force divided by vertical load) for a given set of conditions as a wheelset is displaced laterally through the tread region onto the flange. Data for an AAR wheel profile and CNH wheel profile on new rail for two values of wheel-rail friction coefficient are plotted. The data show that the torque-lateral load characteristic is relatively independent of friction for a wheelset with no yaw angle on tangent track. However for the wheelset with a 10-mrad yaw angle on a 10-degree curve, a significant difference occurs in moment for the same lateral force between the case with a wheel-rail friction coefficient of 0.5 and 0.25. The data show that changes in friction can significantly influence wheel-rail forces under high slip conditions.

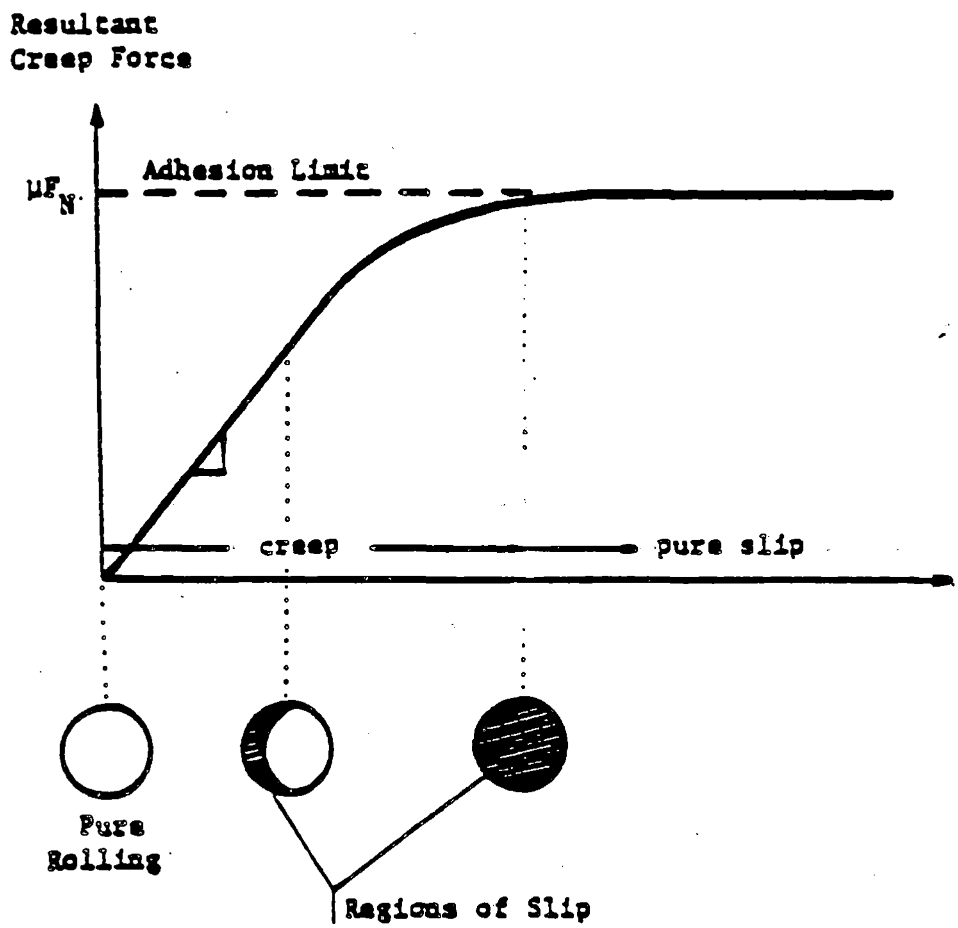

FIGURE 2-6. REGIMES OF CREEP FORCE SATURATION

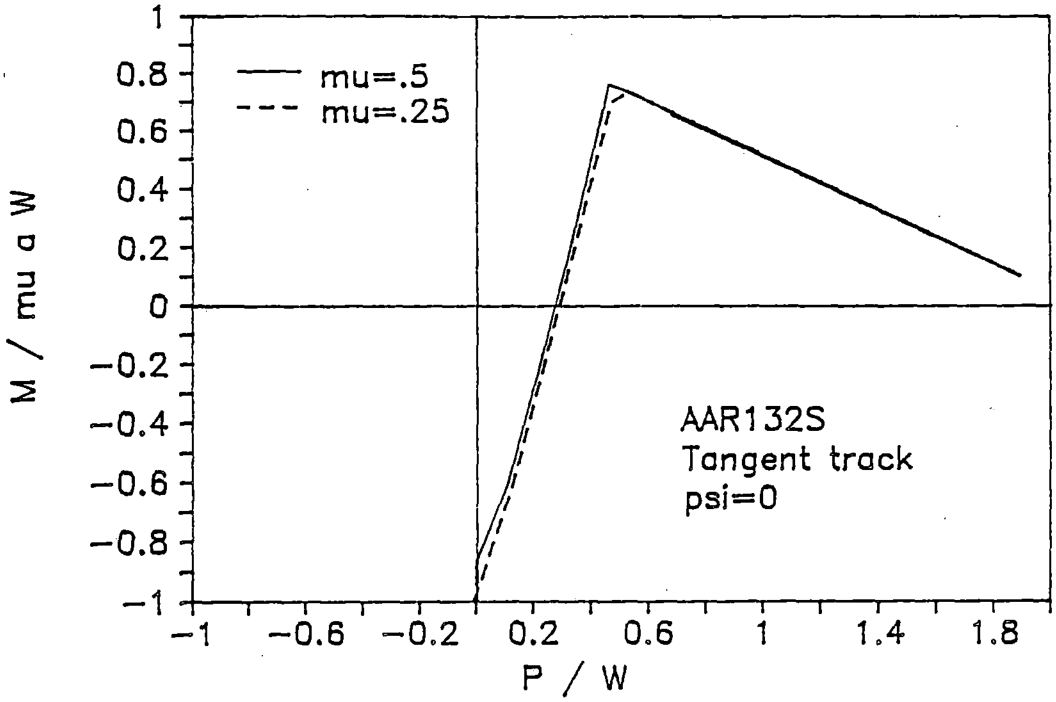

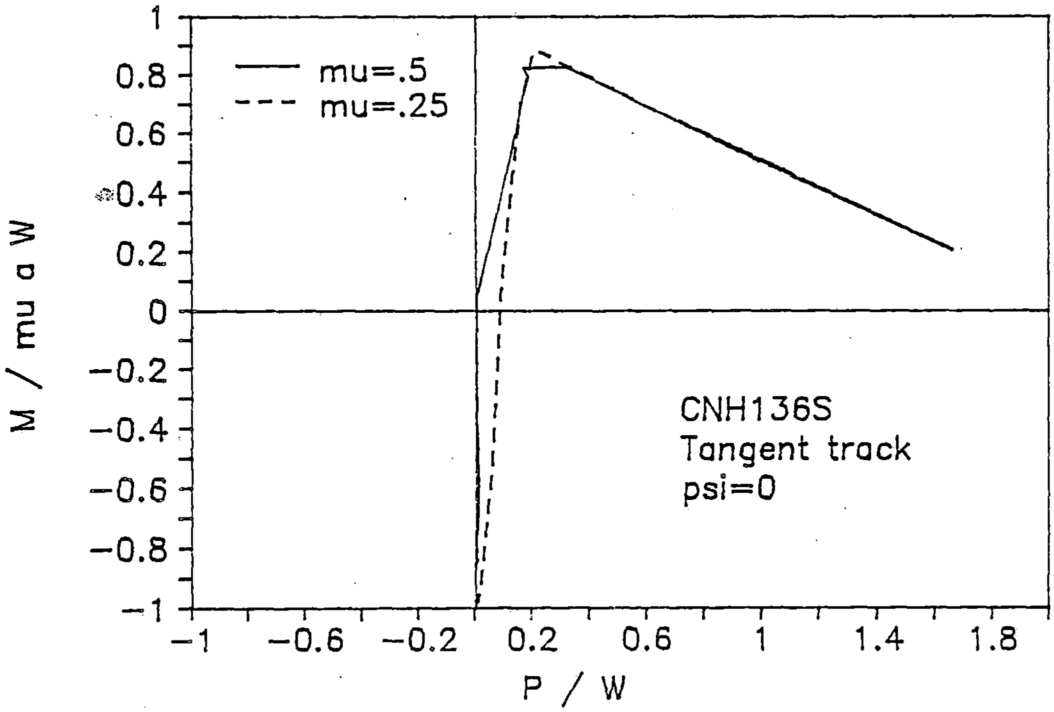

FIGURE 2-7. NONDIMENSIONAL YAW MOMENT VERSUS LATERAL FORCE CHARACTERISTIC ON TANGENT TRACK, NO WHEELSET YAW

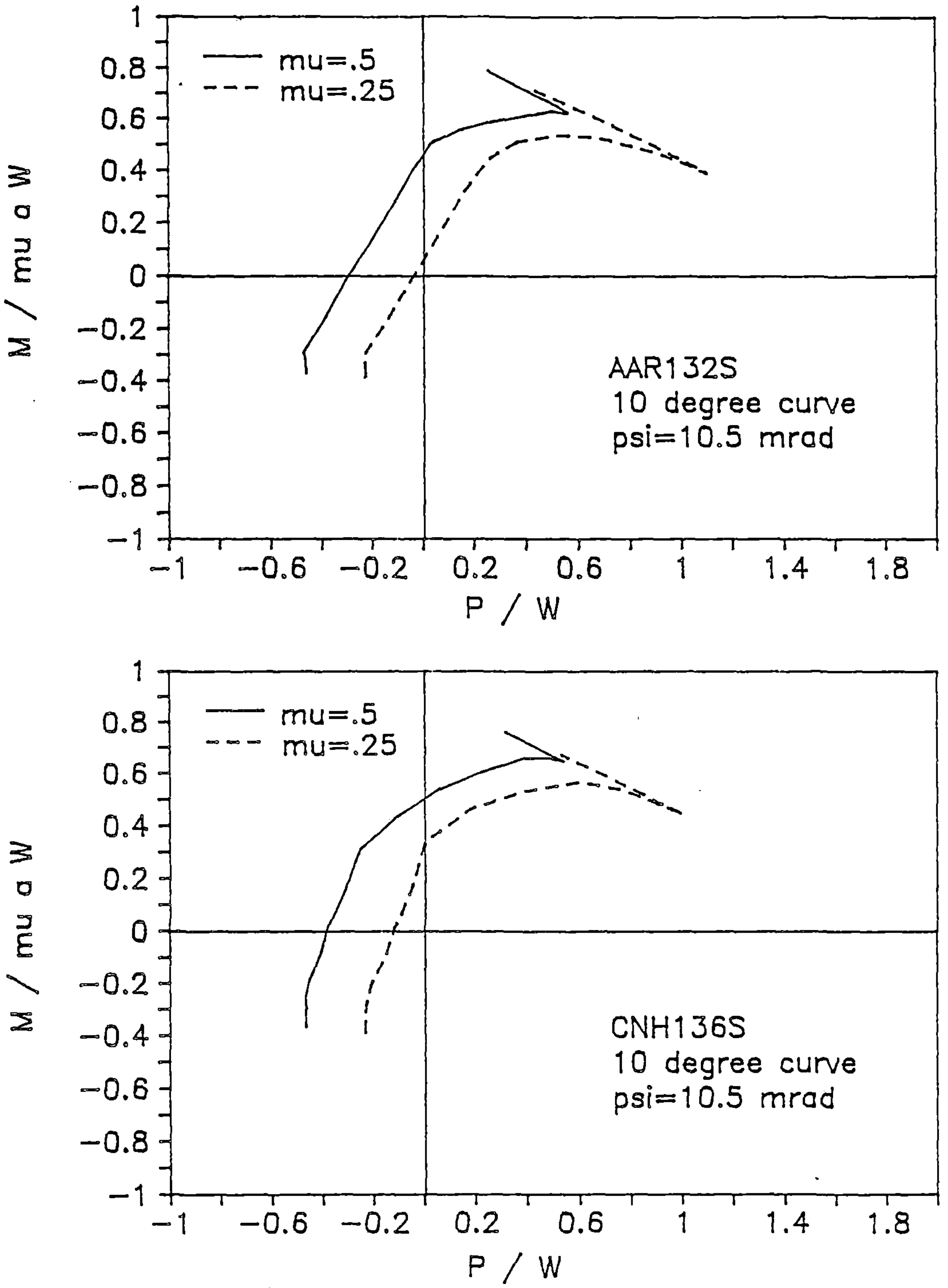

FIGURE 2-8. NONDIMENSIONAL YAW MOMENT VERSUS LATERAL FORCE CHARACTERISTIC ON 10-DEGREE CURVE, 10.5-MRAD ANGLE OF ATTACK

2.4 SIMULATION MODEL FOR PROTOTYPE VEHICLE

A schematic representation of the two-axle prototype vehicle is shown in Figure 2.9. The vehicle consists of a beam-like carbody supported on two axles through swinglink-leaf spring suspensions. A description of the vehicle, which is designed for carrying trailers is contained in Reference [12]. In the model vehicle, the twelve degrees of freedom listed in Table 2.1 have been defined including rigid carbody lateral, vertical, roll, pitch, and yaw displacements, as well as flexible carbody vertical and lateral bending and longitudinal twist motions. Each axle is represented with a lateral and yaw degree of freedom.

In addition to the 12 explicit degrees of freedom, 2 types of implicit degrees of freedom are used--one for each axle rotation in the computation of wheel-rail spin creep and a second for each bushing spring in the computation of the longitudinal damper-bushing forces.

For all rotational and flexible degrees of freedom, small angle assumptions are employed in equation derivations. These are valid even for the current large displacement model, since the angles of the major body components, even under extreme conditions, are small enough for the small angle assumption to be valid. With the small angle assumption, the strokes across the suspensions are directly proportional to angles of rotation, and moment arms used in calculating suspension torques are constant. In addition to the small angle assumption, only first bending modes are considered, since higher body modes have frequencies outside the primary range of model interest.

The suspension of the dual-axle vehicle utilizes a leaf spring for vertical springing and damping. The carbody is hung from the leaf spring through swinglinks which are hinged in the center. The swinglinks provide both the lateral and longitudinal stiffness. The lateral damping is caused

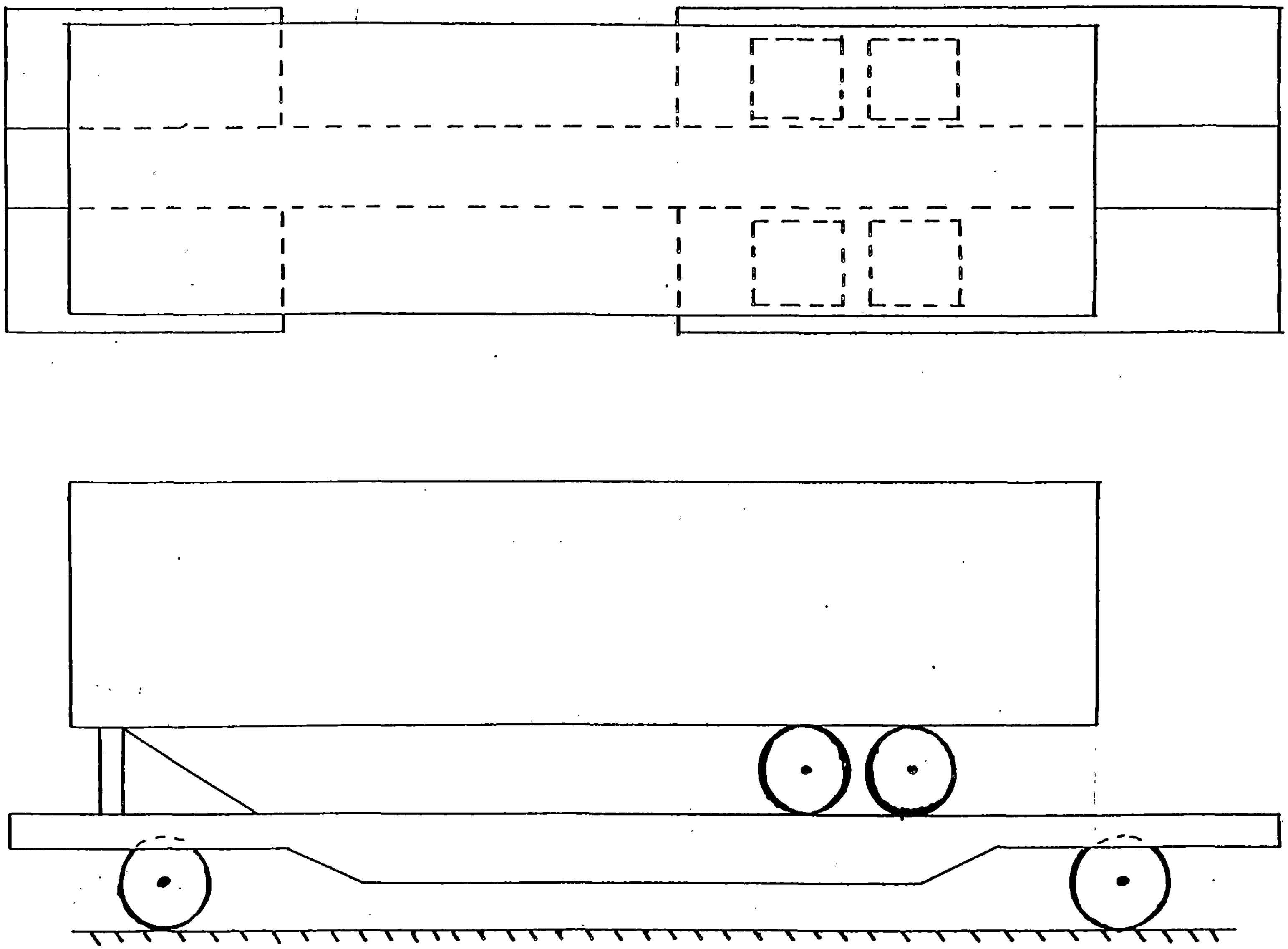

FIGURE 2-9. TWO-AXLE VEHICLE SCHEMATIC

by dry friction in the swinglinks while the longitudinal damping is provided by a hydraulic damper. This damper is connected to the car frame through a rubber bushing. A schematic of the suspension is shown in Figure 2.10.

TABLE 2.1 VEHICLE DEGREES OF FREEDOM

X(1) = Carbody Lateral

X(2) = Carbody Vertical

X(3) = Carbody Roll

X(4) = Carbody Pitch

X(5) = Carbody Yaw

X(6) = Carbody Vertical Bend

X(7) = Carbody Lateral Bend

X(8) = Carbody Longitudinal Twist

X(9) = Leading Wheelset Lateral

X(10) = Leading Wheelset Yaw

X(11) = Trailing Wheelset Lateral

X(12) = Trailing Wheelset Yaw

In this section the elements of the suspensions between the car and wheelsets are described. The detailed suspension force equations are presented in Appendix C. The model incorporates four sets of longitudinal, lateral, and vertical suspension elements, one set associated with each wheel.

2.4.1 Car/Wheel Longitudinal Suspension

The car/wheel longitudinal suspension is a swing hanger suspension which is oriented vertically with the wheelset connection point at the top and the

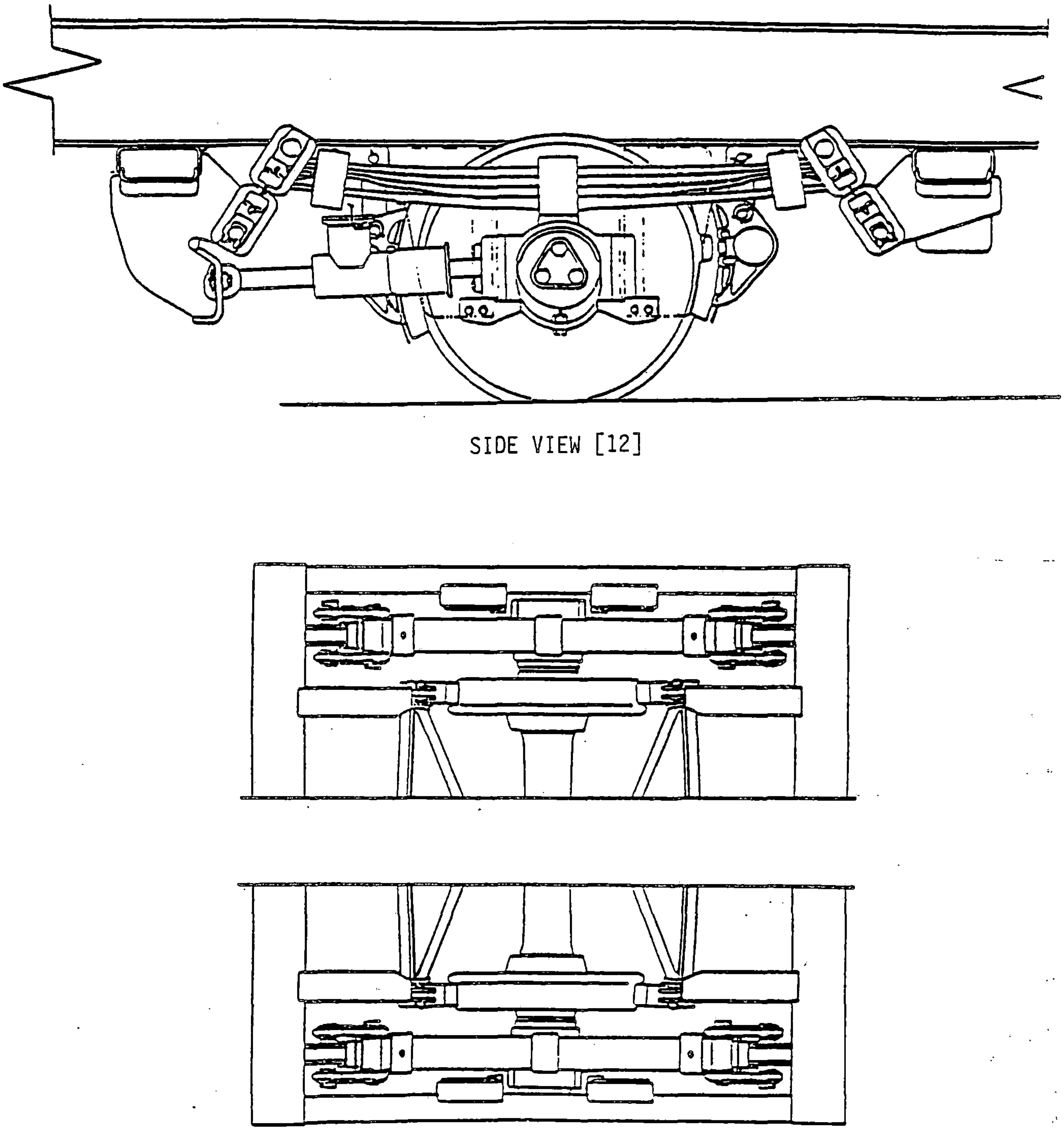

SIDE VIEW [12]

TOP VIEW [12]

FIGURE 2-10. TWO-AXLE VEHICLE SUSPENSION car connection point at the bottom. As the car and wheelset move longitudinally relative to each other, there is an effective pendulum length which affects the stiffness of the suspension. Although the pendulum length is variable, the stiffness of this first stage is represented as constant over the range in which the pendulum swings freely. The pendulum stiffness is:

$$KLON = \frac{WGTCAR}{4 \cdot LLON}$$

where

KLON: Longitudinal swing hanger stiffness

WGTCAR: Car weight

LLON: Effective longitudinal pendulum length

In addition to the pendular spring, an axle guard effectively serves as a very high second-stage stiffness. Damping is provided by a hydraulic damper connected to the carbody through a rubber bushing. The modeling of this series spring-damper element is discussed in Appendix C. Figure 2.11 shows an idealization of the car/wheel longitudinal suspension.

Strokes across the car/wheel longitudinal suspension are considered positive when the wheel connection point is displaced in the positive direction relative to the car connection point.

2.4.2 Car/Wheel Lateral Suspension

The car/wheel lateral suspension is a swing hanger suspension, which is oriented vertically with the wheelset connection point at the top and the car connection point at the bottom. The stiffness of the lateral suspension as the car and wheelset move laterally relative to each other is determined from

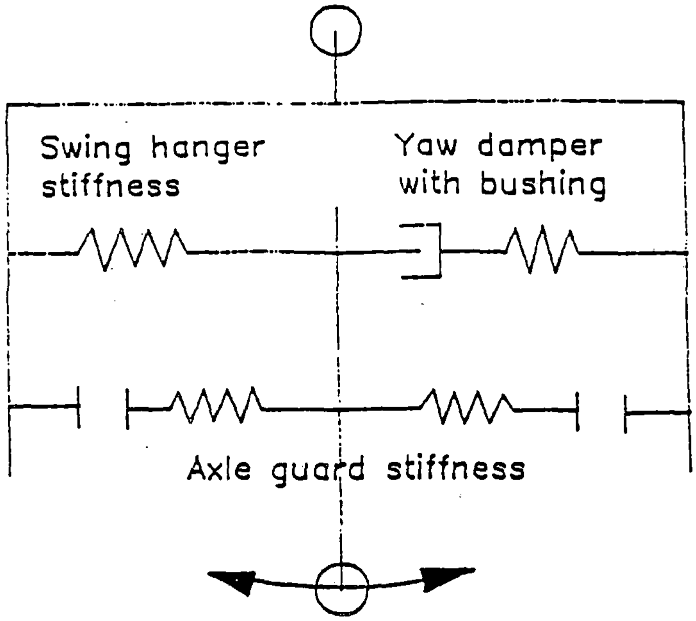

FIGURE 2-11. LONGITUDINAL SUSPENSION SCHEMATIC

the swing hanger pendulum stiffness in a similar manner as the longitudinal suspension.

The first and smallest pendular stiffness occurs during relatively small strokes when the full length of the swinglink is in motion. If the stroke is large enough, a stop is encountered, cutting the swinglink length in half and thereby doubling the theoretical pendular stiffness. Experiments have shown that the leaf spring contacts the axle guard at this point, which leads to a higher second-stage stiffness than that predicted using only the effective pendulum length [13].

The final change in stiffness occurs when the axle guard stop is encountered. This final stiffness is substantially larger than the second-stage stiffness. Damping is provided by coulomb friction in the swinglinks. Figure 2.12 shows an idealization of the car/wheel lateral suspension.

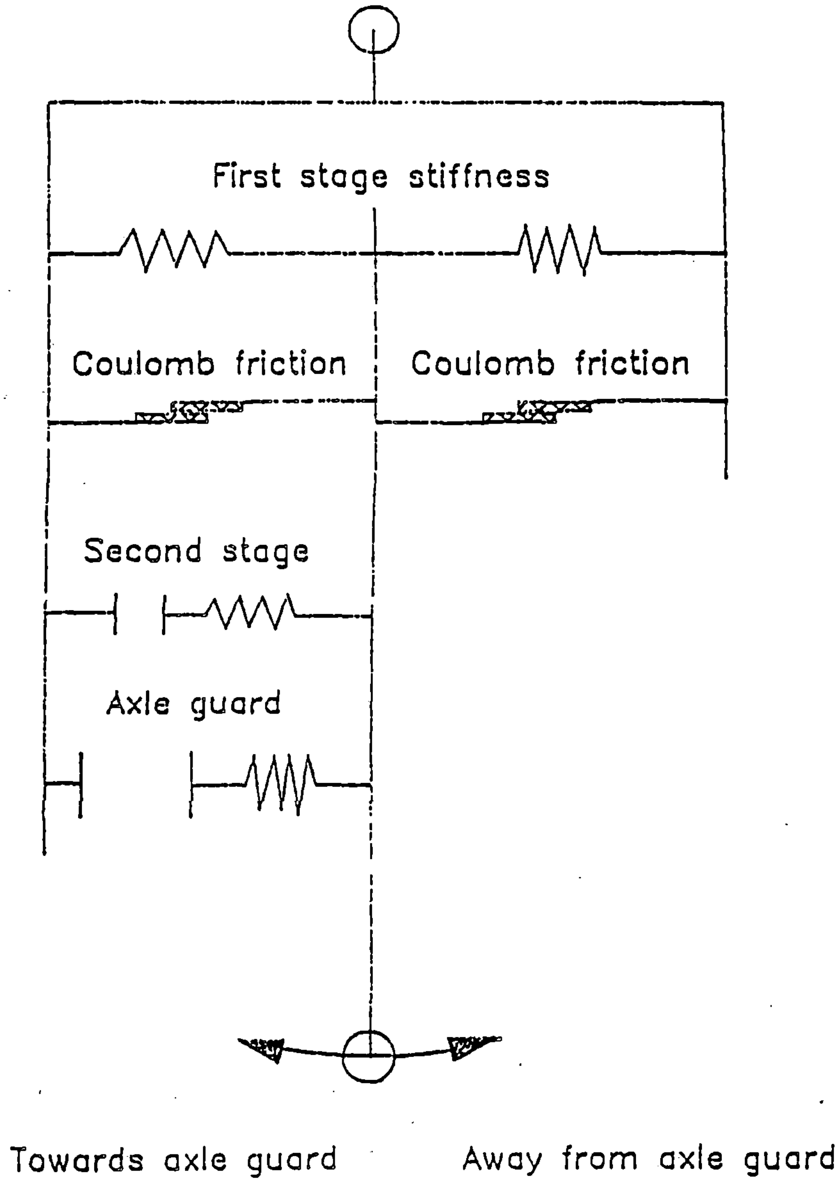

FIGURE 2-12. LATERAL SUSPENSION SCHEMATIC

2.4.3 Car/Wheel Vertical Suspension

The car/wheel vertical suspension is a two-stage leaf spring. Because it is two-staged, a loaded car generally operates in the region of the stiffer second stage. The leaf spring is modeled as a hysteretic element which consists of a two-stage piecewise linear spring in parallel with coulomb friction. The model used to represent the leaf spring has been adapted from a detailed study of the damping and stiffness properties of leaf springs [14]. In the model, the transition from positive to negative coulomb damping is represented as an exponential trajectory. Figure 2.13 shows an idealization of the car/wheel vertical suspension.

2.5 VEHICLE AND TRACK PARAMETERS

The parameters representing the vehicle body and suspension elements for the prototype vehicle are summarized in Appendix D. These parameters have been determined by AAR from measurements of vehicle components for the unloaded vehicle.

The vehicle was operated on a series of track segments constructed to establish Chapter XI track conditions. For each of these conditions, the wheel-rail profile appropriate for the track section as measured in the field was used in the simulations. These profiles are summarized in Appendix D. Addditionally, for perturbed track tests, field measured track lateral and vertical perturbations were used to represent the test track directly. These sections of field track geometries have been stored on magnetic disks in a form convenient for simulation. Thus, simulations conducted in this study have utilized measured track data for perturbed track sections.

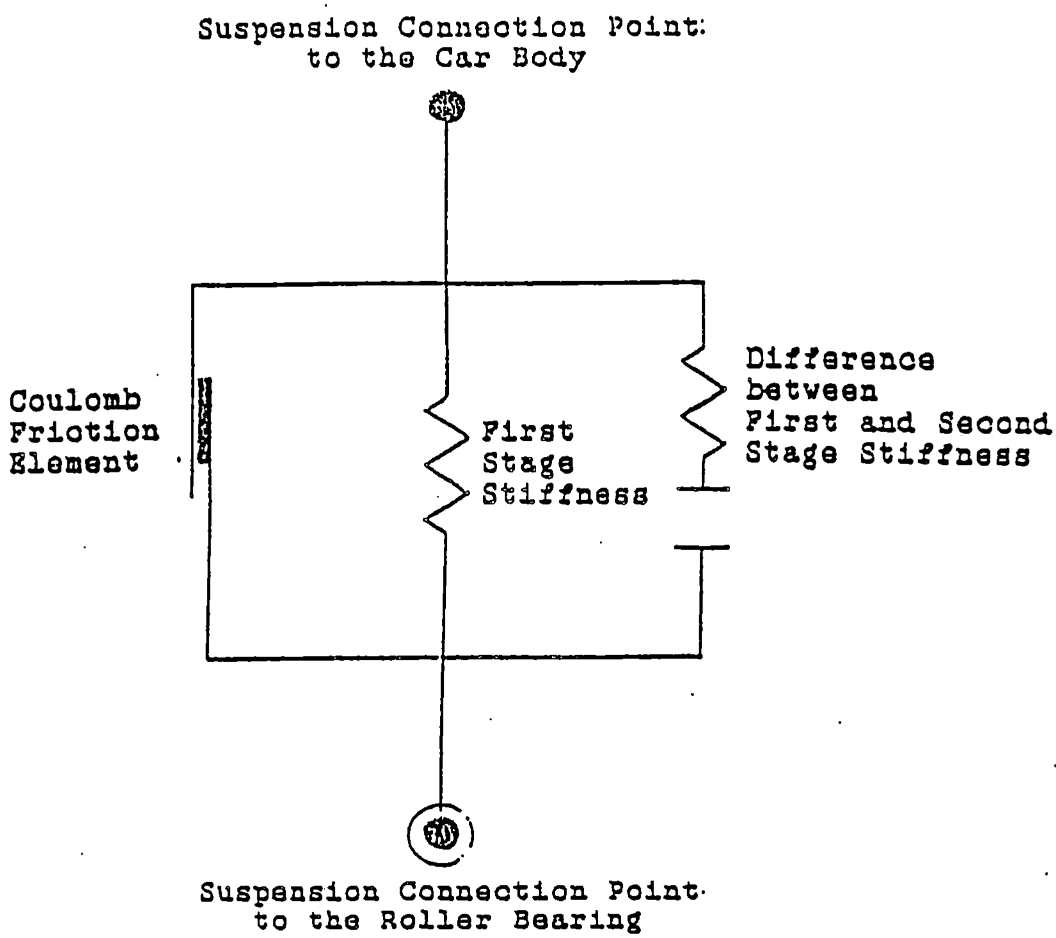

FIGURE 2-13. VERTICAL SUSPENSION SCHEMATIC

3. VEHICLE PERFORMANCE EVALUATION

3.1 SCOPE OF STUDY

An extensive set of field tests was conducted on the unloaded two-axle vehicle equipped with instrumented wheelsets. These tests were conducted on tangent, curved, and perturbed track specifically constructed at the AAR Test Center to provide track conditions described by Chapter XI. These tests have provided some of the most detailed dynamic performance data available in North America [6]. The test data provide an opportunity to assess both the performance of the prototype vehicle and capabilities of the analytical model to predict field performance. In the study described in this report, areas of agreement and disagreement between the field data and the simulations are identified, and, in particular, the fidelity of the wheel-rail model is assessed. Additionally, simulations have been conducted to complement the field tests by assessing conditions for which test data are not available. These simulations were designed to determine performance for vehicle or track conditions which have been identified as important in an overall evaluation of the vehicle-safety-related dynamic performance.

3.2 VEHICLE LATERAL HUNTING STABILITY

The unloaded baseline vehicle was simulated operating on unperturbed tangent track to assess vehicle lateral stability. Time histories of the vehicle leading wheelset lateral motions from an initially displaced lateral position of 0.35 inches at 100 mph and at 105 mph are illustrated in Figure 3-1. At 100 mph, the initial displacement dies out, and the vehicle is stable. At 105 mph, however, sustained hunting oscillations occur with flange-to-flange wheel lateral displacement.

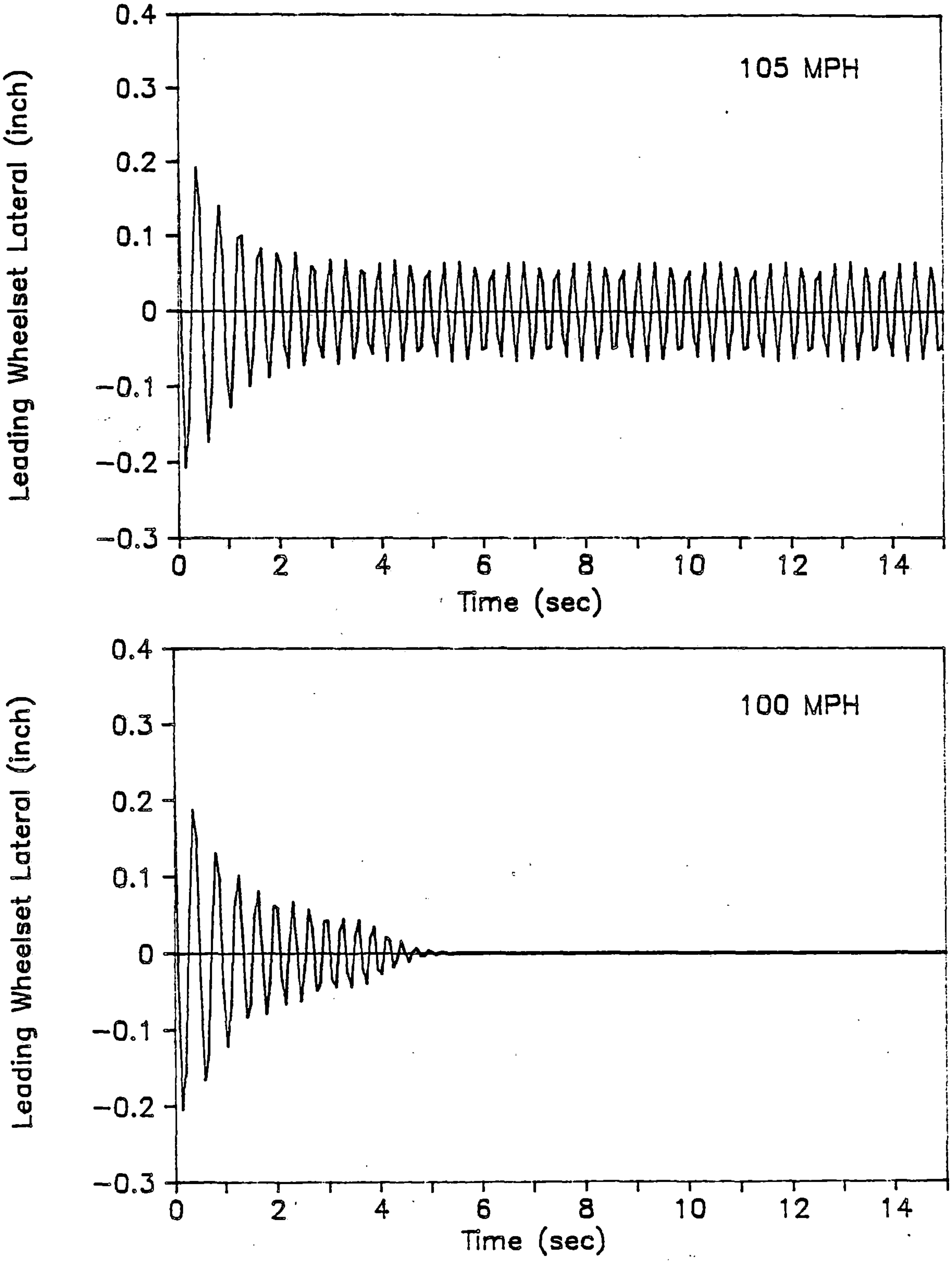

FIGURE 3-1. LEAD WHEELSET LATERAL RESPONSE ON SMOOTH TANGENT TRACK

Field tests conducted on the unloaded vehicle operating on tangent track indicated no evidence of sustained hunting between 40 mph and 90 mph. Thus, the field tests and simulation generally agree.

In shakedown tests of the vehicle prior to field testing, the vehicle longitudinal suspension which includes an elastically mounted hydraulic shock absorber, was tuned to provide good lateral stability. The simulation parameter values reflect the field test values of the parameters as determined by AAR tests. Additional simulations, summarized in Figure 3-2, were conducted to evaluate the influence of the shock absorber on the hunting speed. As the hydraulic damper is reduced to 50-percent effectiveness, the vehicle hunting speed decreases to 60 mph, and as the hydraulic damper is reduced to 25-percent effectiveness, the hunting speed decreases to 33 mph. These simulations indicate that an effective hydraulic damper is required to achieve an acceptable hunting speed for the vehicle.

The baseline simulations were conducted for the vehicle operating on a dry track with a wheel-rail friction coefficient of 0.5. Simulations conducted with the lower friction coefficient of 0.4, reflecting the presence of some moisture or lubrication, have indicated that the hunting speed increases to above 110 mph. Thus, these simulations illustrate, as has often been observed in field testing, that a reduction in the wheel-rail friction coefficient increases the hunting speed.

3.3 STEADY-STATE CURVING

An extensive set of field data was measured using instrumented wheelsets for the vehicle operating on 5-degree, 7.5-degree and 10-degree curves at the Pueblo Test Track. The instrumented wheelsets provide measurements of vertical, lateral, and longitudinal force for each wheel on the vehicle.

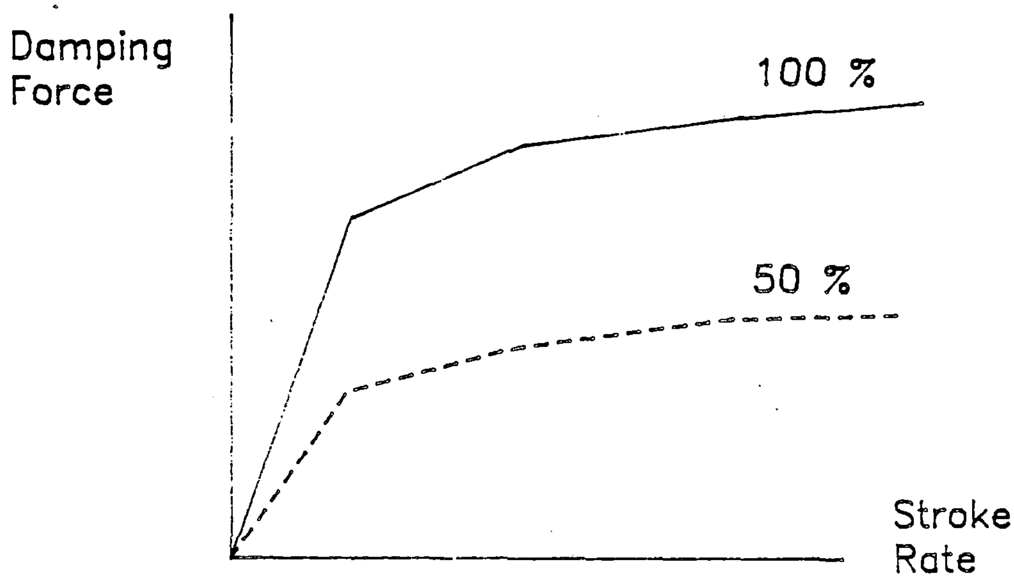

Damping (% of nominal)	Hunting Speed (MPH)
100 %	105
75 %	90
50 %	60
25 %	33

FIGURE 3-2. CRITICAL HUNTING SPEED VARIATIONS AS A FUNCTION OF DAMPING CHARACTERISTIC

Data summarizing the steady-state forces, torques, and axle angles occurring as the vehicle traversed the curves at constant speed, for two runs each in clockwise and counterclockwise directions, are summarized in Figures 3-3 through 3-9. Also summarized in each plot are simulation results based upon measured wheel-rail profiles for the curves. To indicate the sensitivity of the simulations to changes in wheel-rail friction coefficient, results are shown for wheel-rail coefficients of 0.5 and 0.4.

The measured wheel vertical forces for four experimental runs at each speed on each curve for all of the test runs are plotted in Figures 3-3 and 3-4. Also plotted are corresponding computer simulations conducted with wheel-rail coefficients of friction of 0.4 and 0.5. These data show the transfer of vertical force from the inner wheels to the outer wheels as vehicle speed is increased from below balance speed to above balance speed. The trends in the test data as a function of speed are similar to those of the computed data. Very little difference occurs between the two sets of computed data for friction coefficients of 0.4 and 0.5. The test data plotted for clockwise and counterclockwise tests have, in general, about as much variation in their values for a given test as the variation between the test data and the computed data. The primary difference between the test data and computed data is for the lead inner wheel, where the experimental data for every test indicates a lower vertical load than does the computed data. Part of this difference may be due to the instrumented wheelset calibration, since the total sum of the measured vertical forces on the four wheels was 600 pounds less than the stated vehicle weight and the front-axle measurements identified were lower than those expected from the vehicle weight distribution.

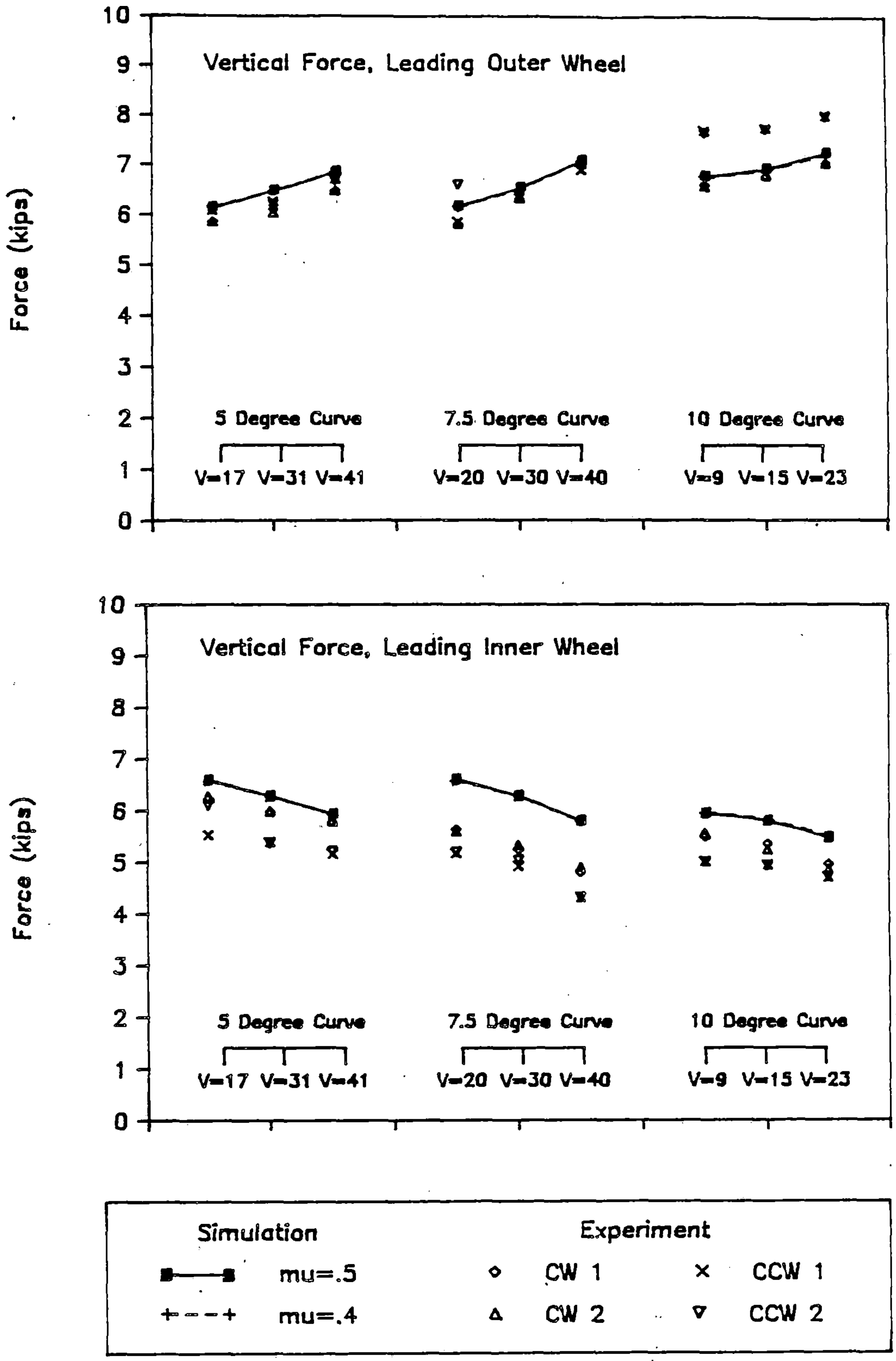

FIGURE 3-3. STEADY CURVING WHEELSET VERTICAL FORCES - LEADING AXLE

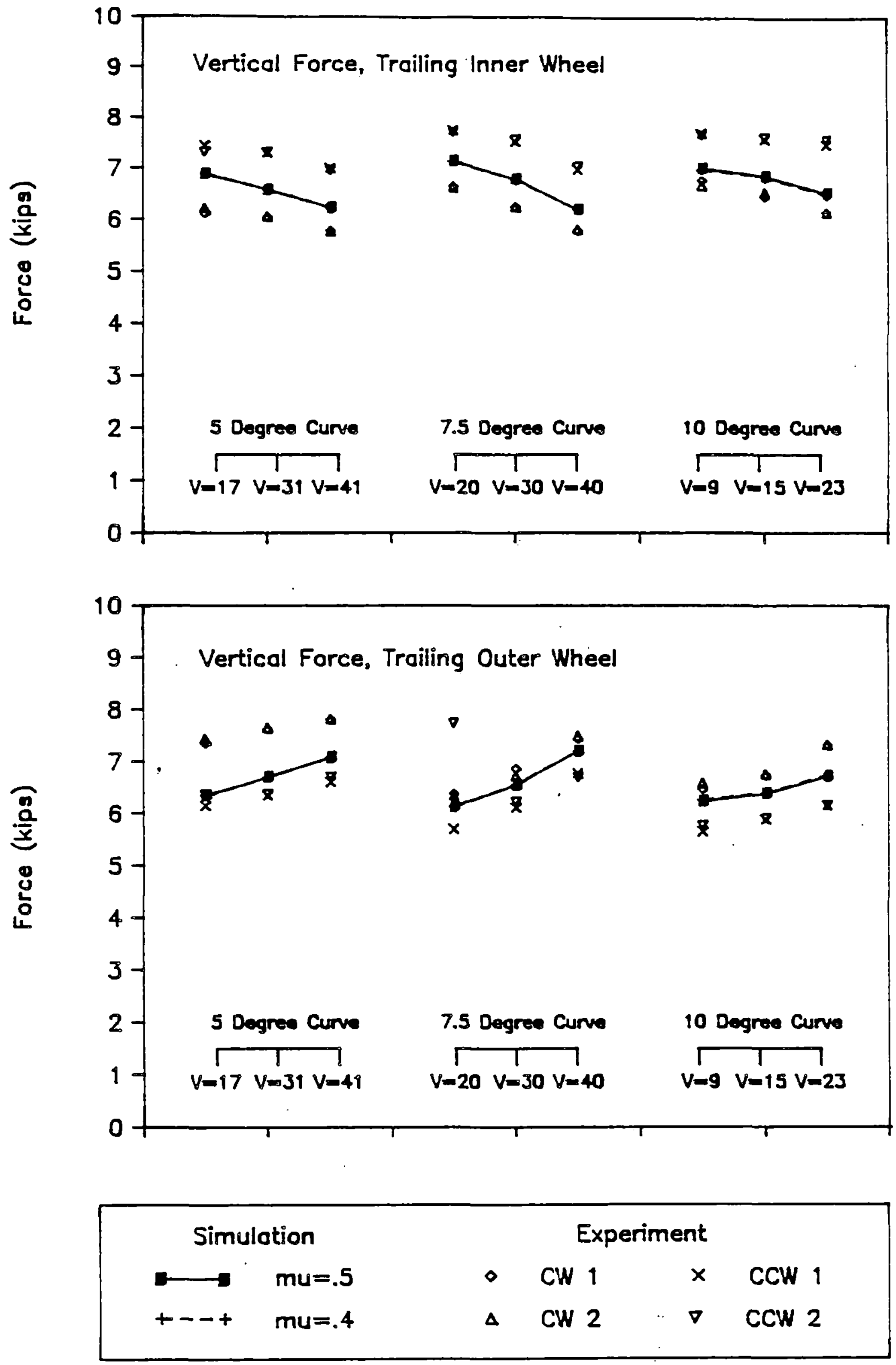

FIGURE 3-4. STEADY CURVING WHEELSET VERTICAL FORCES - TRAILING AXLE

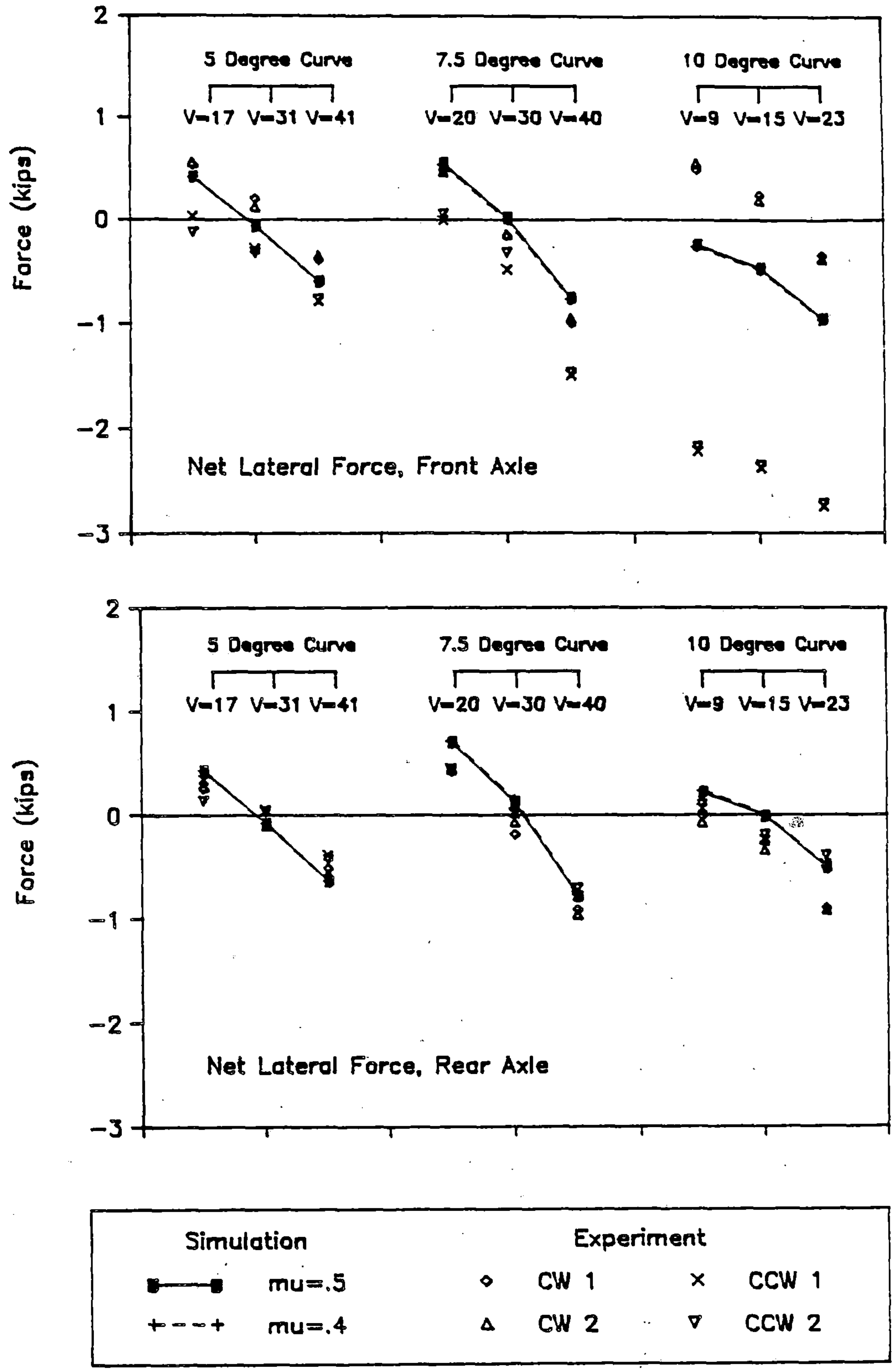

FIGURE 3-5. STEADY CURVING NET WHEELSET LATERAL FORCES

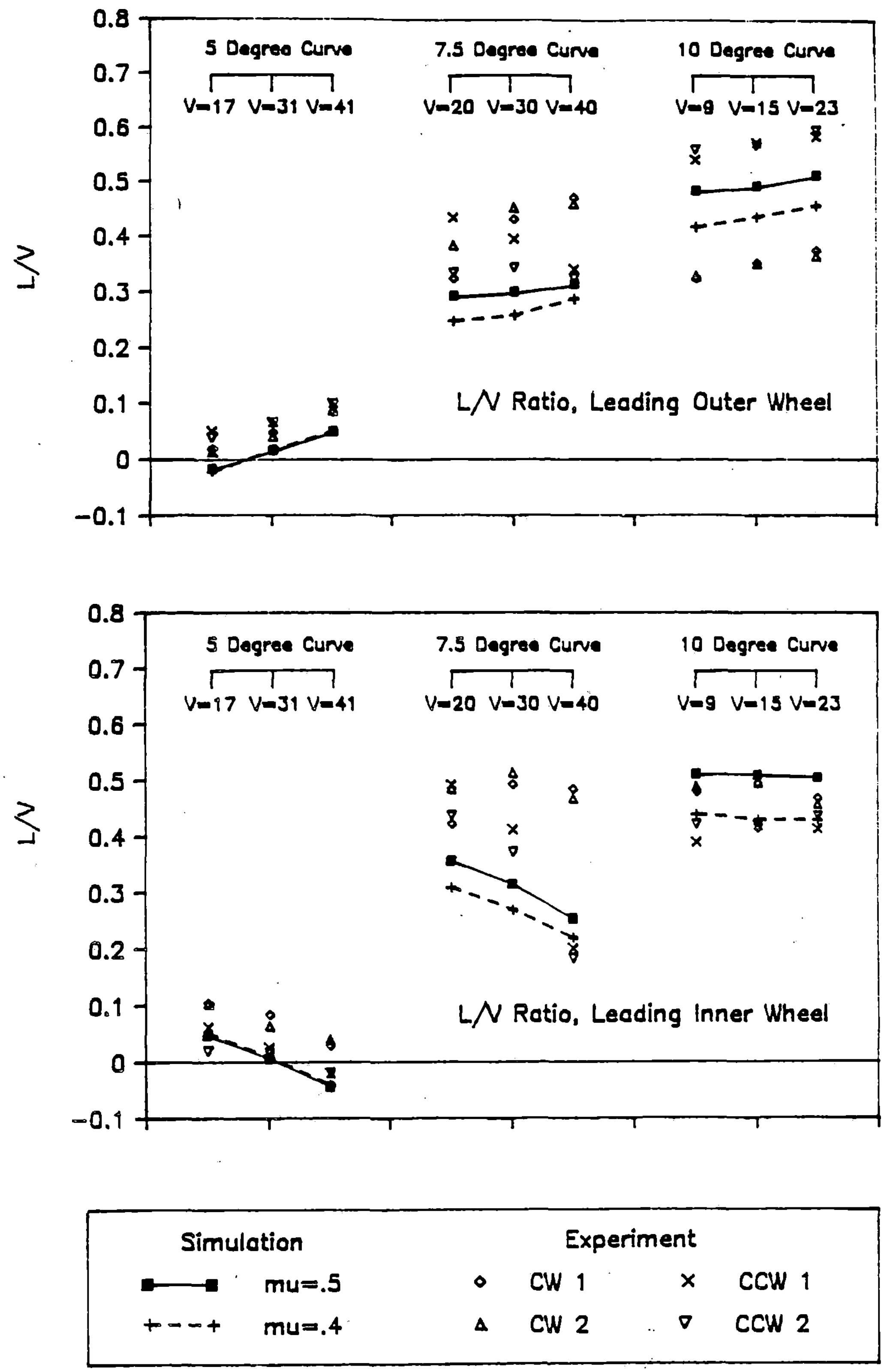

FIGURE 3-6. STEADY CURVING WHEELSET L/V RATIOS - LEADING AXLE

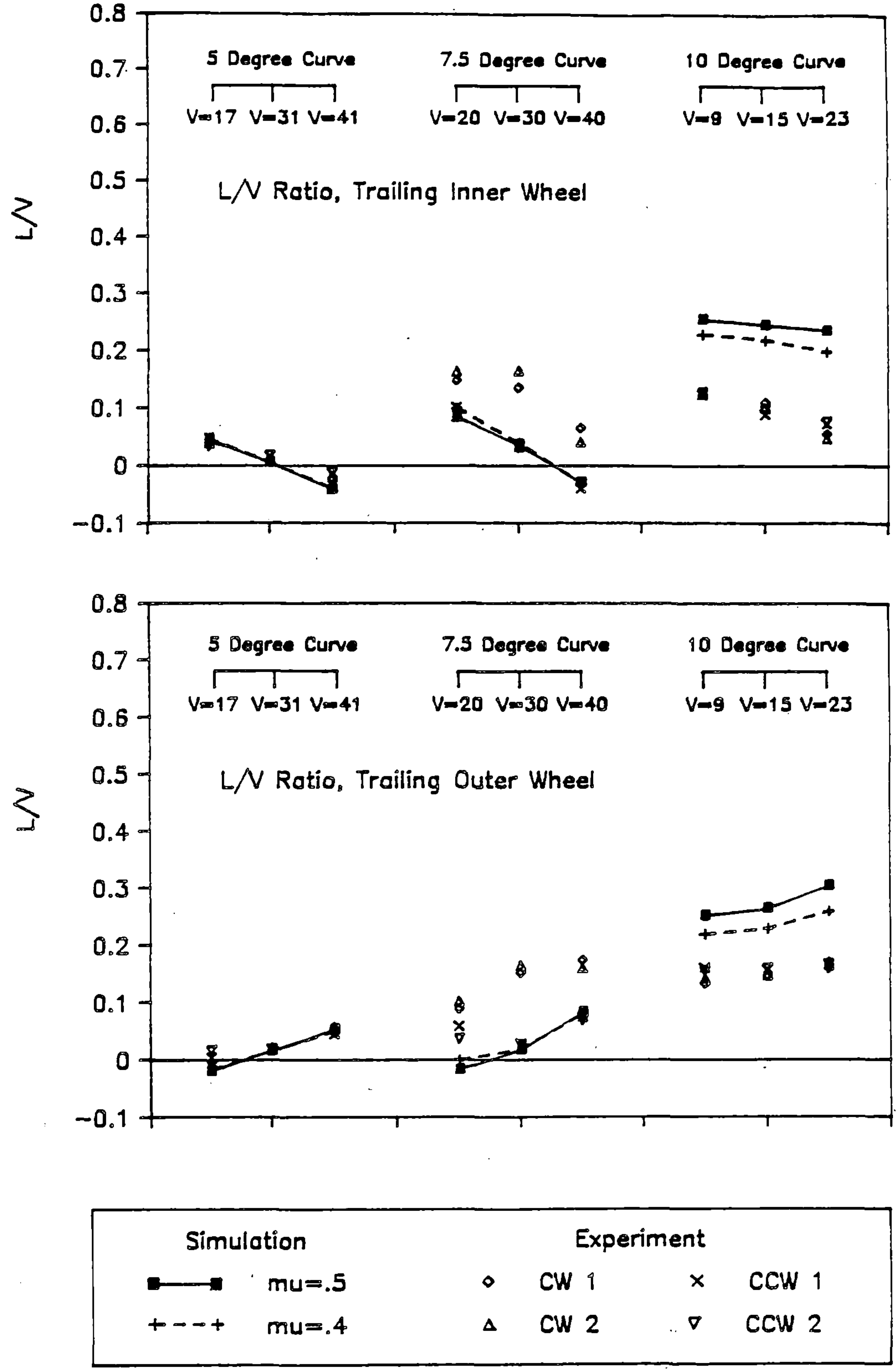

FIGURE 3-7. STEADY CURVING WHEELSET L/V RATIOS - TRAILING EDGE

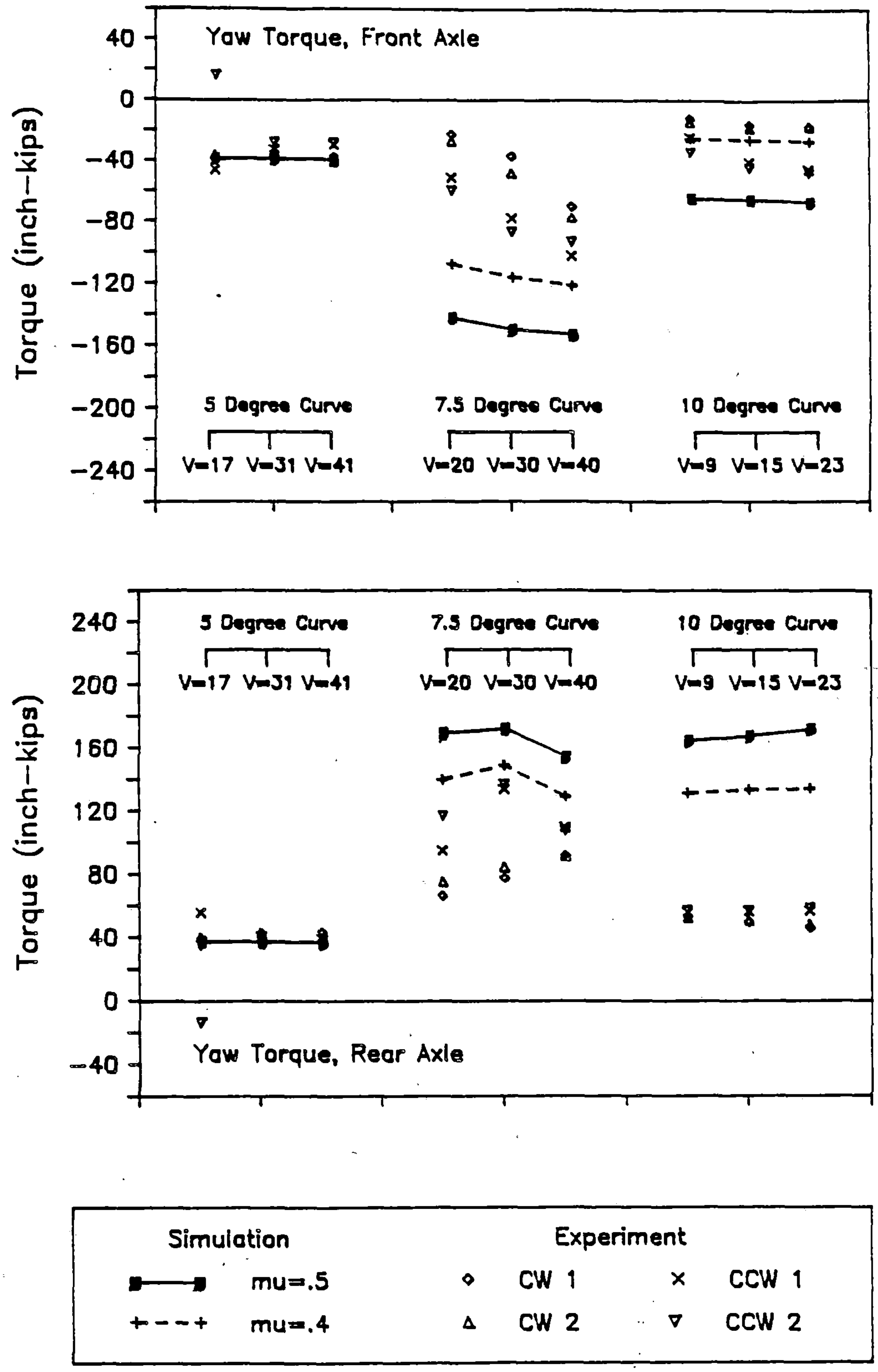

FIGURE 3-8. STEADY CURVING WHEELSET YAW TORQUE

The net lateral forces on the front and rear axles for each test are plotted in Figure 3-5. The computed data plotted show very little sensitivity to a variation in wheel-rail friction coefficient from 0.5 to 0.4. Both the computed data and the test data show identical trends for the lateral force variation as the vehicle speed increases from an underbalanced to an overbalanced condition. Test data for the trailing axle have relatively little variation with a maximum of 500 pounds among the four test runs for each test condition and are in relatively close agreement (±500 pounds) with the computed lateral forces. The lead axle test data have relatively significant variations between tests run clockwise and counterclockwise. The major difference, of greater than 2,500 pounds, occurred on the 10-degree curve. It is thought that this difference in test data was caused by suspension friction and axle misalignment; however, causes have not yet been conclusively determined. The computed data lie between the clockwise and counterclockwise data for the lead axle on the 10-degree curve and exhibit similar trends to the test data.

Plots of L/V ratios for each wheel for all of the tests are summarized in Figures 3-6 and 3-7. The computed data show that the wheel L/V ratios for the 5-degree curve are relatively insensitive to changes in friction levels. They show more sensitivity for the 7.5-degree and 10-degree curves where increased flanging occurs. For the 10-degree curve, a reduction of between 0.05 and 0.01 occurs in wheel L/V when the friction coefficient is reduced from 0.5 to 0.4. The L/V ratios for the lead outer wheel are the largest recorded during the test. For this wheel, L/V ratios increased from approximately 0.05 for the 5-degree curve to 0.4 for the 7.5-degree curve to 0.5 for the 10-degree curve. The trends in both the test data and the computed data as speed increases and the degree of curvature increases are

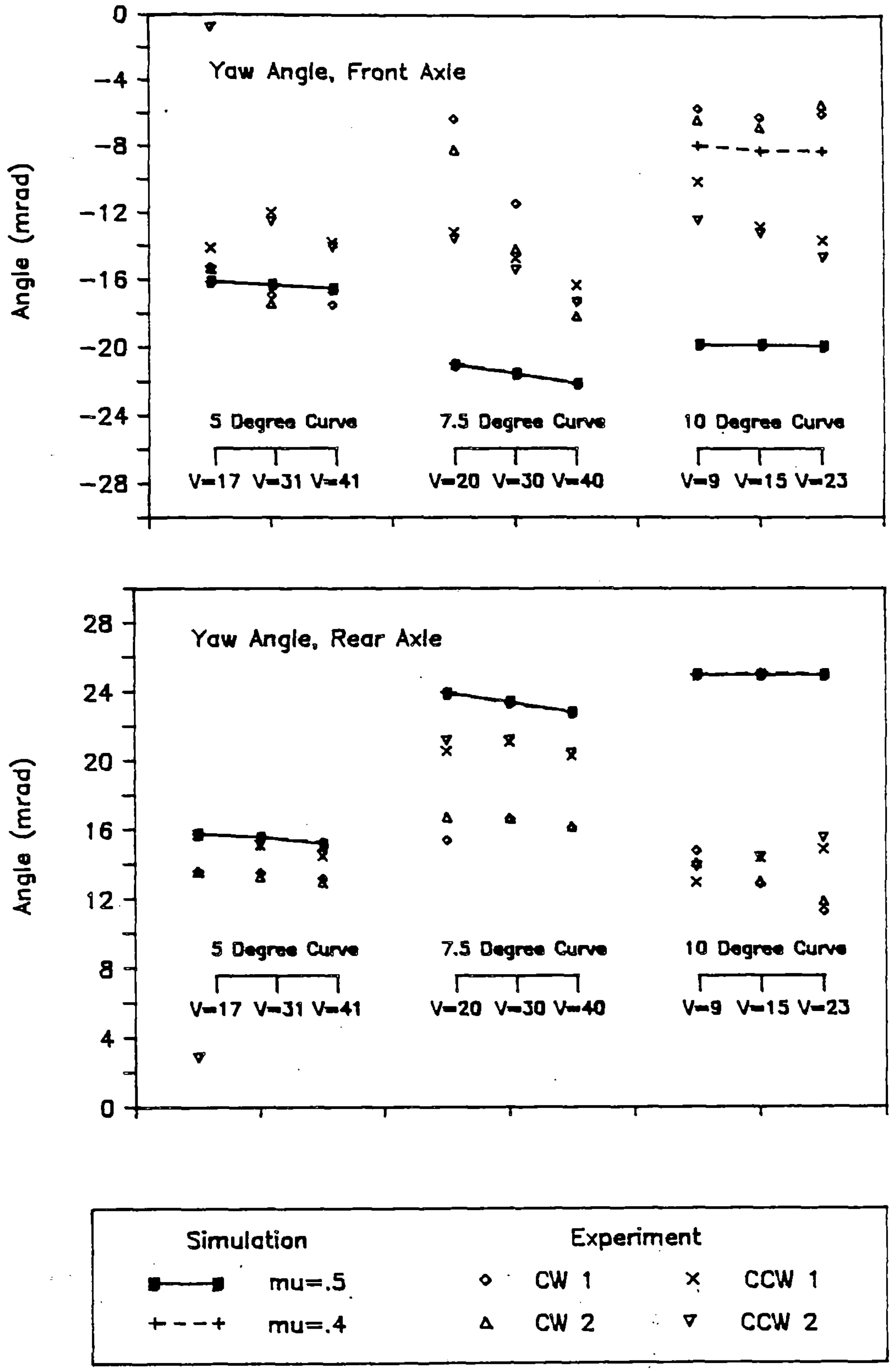

FIGURE 3-9. STEADY CURVING WHEELSET YAW ANGLES

similar. All of the computed and test data indicate L/V ratios of less than 0.8 in all tests. For the 10-degree curve, data variations in L/V of 0.25 occurred between clockwise and counterclockwise data. The computed data lie between these two sets of test data for the lead outer wheel. Data for the trailing axle indicate L/V ratios of less than 0.3 for all curves.

The axle net yaw torque and yaw angles for each test are plotted in Figures 3-8 and 3-9, respectively. Although these quantities are relatively insensitive to changes in the wheel-rail friction coefficient for the 5-degree curve, the computed yaw angle and torque of the lead axle on the 10-degree curve vary significantly with changes in friction coefficient from 0.4 to 0.5, with the lead-axle yaw angle increasing from 8 mrad to 21 mrad as the coefficient of friction is increased from 0.4 to 0.5. Similarly, the yaw torque increases from approximately 20 inch-kips to 60 inch-kips. Thus, the yaw torques resulting from longitudinal creep forces in high-degree curves where significant flanging occurs are relatively sensitive to changes in friction levels.

For the 5-degree curve, there is relatively close agreement between the tested and computed values of yaw torque and yaw angle. In contrast, for the 10-degree curve where significant flanging and creep force saturation occur, the analysis predicts significantly higher yaw torque when based on a friction coefficient of 0.5. That is, a computed torque of 60 inch-kips for the lead axle compares with test data in the range of 20-40 inch-kips, a computed torque of 160 inch-kips for the trailing axle compares with test data in the 40 inch-kip range. The sensitivity of yaw torques to changes in friction in strongly flanging conditions make the precise comparison of test data and computed data difficult. In these strongly flanging conditions, small changes in wheel-rail contact geometry, as well as in friction and creep force saturation mechanisms, can significantly influence the production of longitudinal forces. Both experimental measurements and the computation of wheel-rail forces are difficult under strongly flanging conditions because of the strong sensitivity of wheel-rail forces to small values of displacement.

To provide a view of the overall vehicle curving performance, wheel L/V ratios have been computed for a wheel-rail friction coefficient of 0.5 and the baseline wheel-rail geometry (Heumann wheel profile on new 136-pound rail) for curves of 5-degrees to 15-degrees. These data, plotted in Figures 3-10 and 3-11, illustrate that under these nominal conditions wheel L/V ratios less than 0.6 occur under all operating conditions. For this range of curves, the simulation indicates that the unloaded vehicle curving performance does not approach severe wheel climb.

3.4 VEHICLE RESPONSE TO ALIGNMENT PERTURBATIONS

Tests were performed on the vehicle operating at speeds of 10 mph to 80 mph over 0.5 inch wide gage track with sinusoidal 39-foot periodic alignment variations of 1.25-inch amplitude. Data measured during the test series included the longitudinal stroke, minimum vertical load, and axle L/V ratios for the front axle, and the lateral strokes and peak lateral wheel loads for the front and rear axles. In Table 3-1, these data are summarized and are compared with computed data for the baseline vehicle. Both the computed data and test data for suspension longitudinal stroke for the front axle indicate that as speed increases from 20 mph to 70 mph the longitudinal strokes decrease, but then increase from 70 mph to 80 mph. The stroke amplitudes indicated by the model longitudinal stroke data for all speeds are approximately 50-percent larger than those of the measured data. The

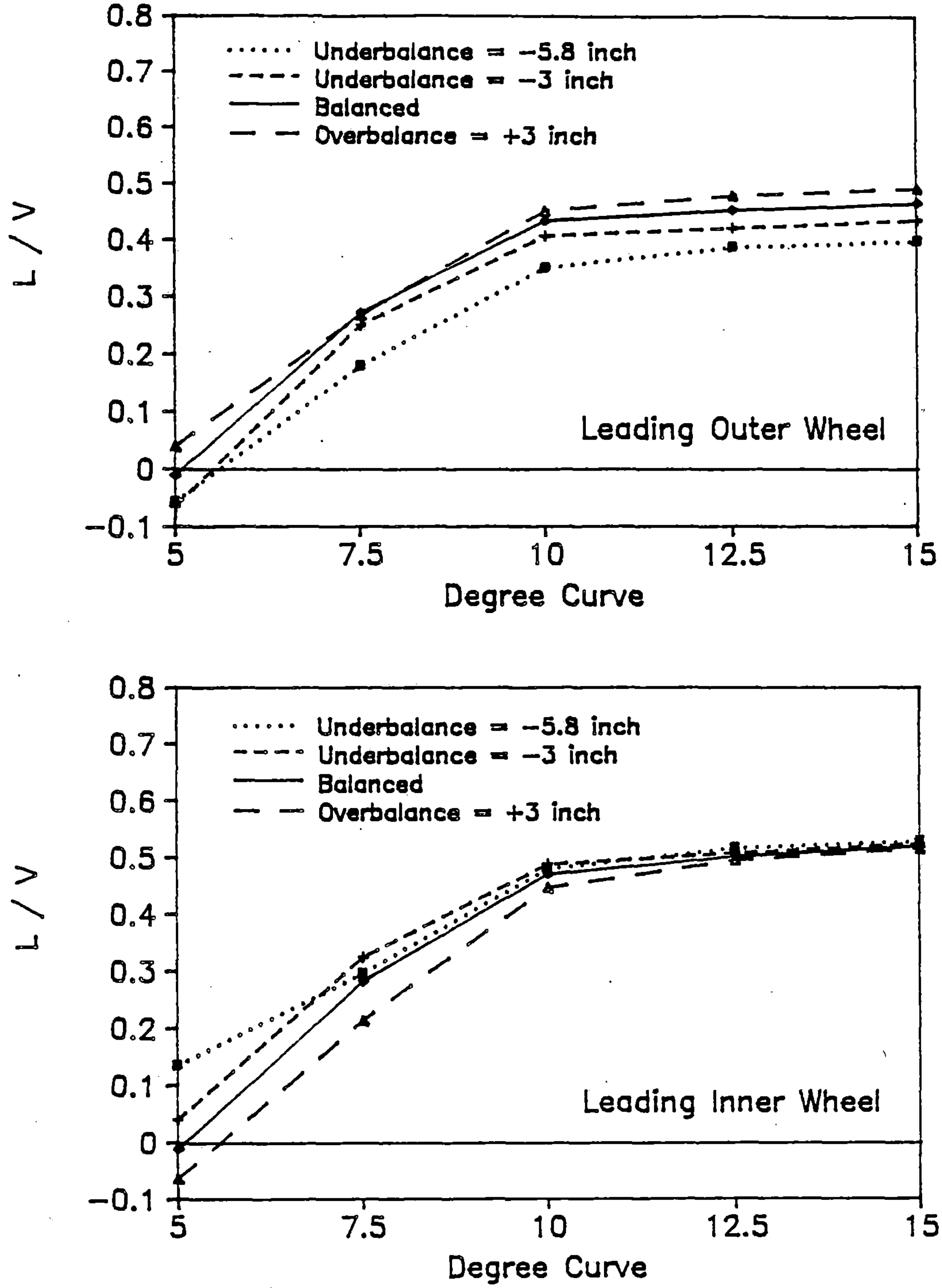

FIGURE 3-10. STEADY CURVING WHEELSET L/V RATIOS WITH SUPERELEVATION OF 6 INCHES - LEADING AXLE

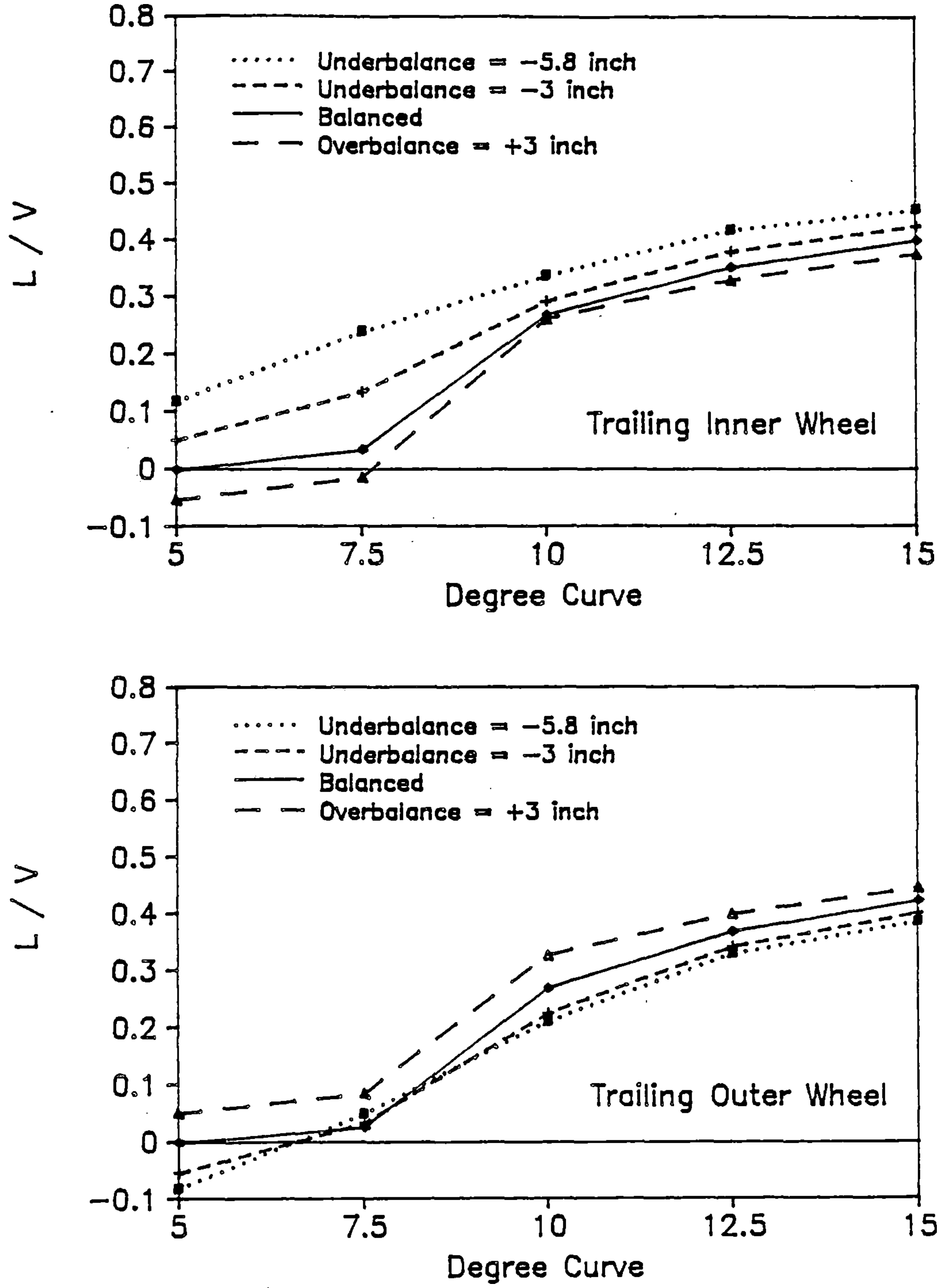

FIGURE 3-11. STEADY CURVING WHEELSET L/V RATIOS WITH SUPERELEVATION OF 6 INCHES - TRAILING AXLE

TABLE 3-1. VEHICLE RESPONSE TO 39-FOOT SINUSOIDAL ALIGNMENT PERTURBATIONS

	Velocity (mph)	Experimental Results	Model Results $\mu = 0.5$	Model Results $\mu = 0.4$
Longitudinal Suspension Stroke, Front Axle (in)	10	.60	.940	.822
	15	.47	.716	.607
	20	.35	.575	.480
	25	.35	.484	.436
	30	.35	.426	.413
	40	.30	.436	.365
	50	.22	.391	.342
	60	.20	.352	.321
	70	.28	.336	.347
	80	.32	.419	.362
Longitudinal Suspension Stroke, Rear Axle (in)	10	-	.989	.869
	15	-	.774	.662
	20	-	.623	.537
	25	-	.526	.449
	30	-	.439	.387
	40	-	.371	.300
	50	-	.298	.248
	60	-	.274	.243
	70	-	.275	.258
	80	-	.290	.281
Lateral Suspension Stroke, Front Axle (in)	10	.12	.151	.059
	15	.15	.129	.044
	20	.18	.131	.037
	25	.15	.124	.081
	30	.20	.169	.126
	40	.15	.325	.147
	50	.18	.259	.150
	60	.30	.225	.279
	70	.70	.361	.407
	80	.70	.645	.764
Lateral Suspension Stroke, Rear Axle (in)	10	.20	.288	.133
	15	.20	.661	.141
	20	.22	2.130	.143
	25	.22	2.341	.356
	30	.28	2.490	.500
	40	.45	2.002	.701
	50	.80	1.160	.691
	60	1.20	1.083	.803
	70	1.45	.991	1.450
	80	1.40	2.336	2.080

TABLE 3-1. VEHICLE RESPONSE TO 39-FOOT SINUSOIDAL ALIGNMENT PERTURBATIONS (CONTINUED)

	Velocity (mph)	Experimental Results	Model Results $\mu = 0.5$	Model Results $\mu = 0.4$
Maximum Lateral Load, Front Axle (lbf)	10	1540	3833	3110
	15	1250	3481	2927
	20	750	3653	3005
	25	1020	3770	3052
	30	1020	3691	3370
	40	1250	4921	4331
	50	1800	5884	3780
	60	2550	4406	5309
	70	6100	6180	7021
	80	5500	7320	8034
Maximum Lateral Load, Rear Axle (lbf)	10	1540	3856	3158
	15	1540	3434	2397
	20	750	3493	2251
	25	1250	3599	1583
	30	1250	4707	1282
	40	1540	1370	1241
	50	2050	1167	1291
	60	2300	1238	1344
	70	2050	1304	1421
	80	2050	2835	2110
Front Axle L/V Sum	10	.40	.977	.761
	15	.35	.845	.700
	20	.25	.833	.712
	25	.35	.809	.679
	30	.32	.760	.707
	40	.40	.822	.698
	50	.45	.899	.569
	60	.55	.629	.700
	70	.85	.852	.877
	80	.95	.965	.971
Rear Axle L/V Sum	10	-	.982	.763
	15	-	.839	.657
	20	-	.843	.513
	25	-	.823	.343
	30	-	.755	.278
	40	-	.338	.215
	50	-	.203	.226
	60	-	.215	.248
	70	-	.230	.256
	80	-	.505	.393

TABLE 3-1. VEHICLE RESPONSE TO 39-FOOT SINUSOIDAL ALIGNMENT PERTURBATIONS (CONTINUED)

	Velocity (mph)	Experimental Results	Model Results $\mu = 0.5$	Model Results $\mu = 0.4$
L/V Ratio, Wheel 1	10	.20	.494	.389
	15	.15	.422	.355
	20	.15	.388	.342
	25	.17	.385	.348
	30	.20	.376	.352
	40	.25	.423	.397
	50	.30	.509	.287
	60	.42	.354	.274
	70	.75	.318	.316
	80	.75	.358	.500
L/V Ratio, Wheel 2	10	.20	.511	.420
	15	.20	.461	.399
	20	.10	.445	.410
	25	.17	.435	.314
	30	.17	.422	.299
	40	.15	.340	.279
	50	.15	.353	.402
	60	.20	.434	.514
	70	.22	.571	.644
	80	.25	.651	.723
L/V Ratio, Wheel 3	10	-	.501	.415
	15	-	.458	.375
	20	-	.472	.316
	25	-	.452	.224
	30	-	.535	.181
	40	-	.194	.161
	50	-	.151	.171
	60	-	.163	.174
	70	-	.171	.182
	80	-	.331	.249
L/V Ratio, Wheel 4	10	-	.482	.365
	15	-	.415	.332
	20	-	.399	.224
	25	-	.377	.172
	30	-	.416	.169
	40	-	.167	.172
	50	-	.169	.181
	60	-	.183	.199
	70	-	.190	.206
	80	-	.278	.226

model data are relatively insensitive to changes in friction coefficient from 0.5 to 0.4.

The data for the measured suspension lateral stroke for the front axle has local peaks at approximately 20 mph and 30 mph and then monotonically increasing strokes above 40 mph. The model data illustrate local peaks at approxmately 20 mph and 40 mph and then monotonically increasing strokes above 60 mph. The front-axle test data vary from a stroke of 0.12 inches at 10 mph to 0.7 inches at 80 mph, while the model data vary from 0.15 inches at 10 mph to 0.65 inches at 80 mph.

The measured rear suspension stroke increases monotonically from 0.2 inches at 10 mph to 1.4 inches at 80 mph. The model rear stroke is sensitive to changes in wheel-rail friction. At a friction coefficient of 0.5, the model stroke indicates a resonance in the lateral suspension at 30 mph with the stroke approaching 2.5 inches. At a friction coefficient of 0.4, however, the stroke exhibits no resonance and monotonically increases with speed reaching a maximum stroke of 2 inches at 80 mph.

The measured and computed peak lateral loads for the front and rear axles, for a friction coefficient of 0.5, are plotted in Figure 3-12. The model predicts significantly higher lateral loads at speeds below 40 mph than those indicated by the measured data. Predicted front-axle lateral loads are twice those measured.

Test data for axle L/V ratios is only available for the front axle. Front axle L/V ratios predicted by the model approach 1.0 at both low and high speeds, while measured data indicate axle L/V ratios of approximtely 0.4 at speeds below 50 mph and L/V ratios of 0.85 and 0.95 at 70 mph and 80 mph respectively. Both the test data (for the front axle) and the model data (for both axles) indicate that axle L/V ratios at all speeds are below a value of 1.3 which is associated with a potential wheel climb condition.

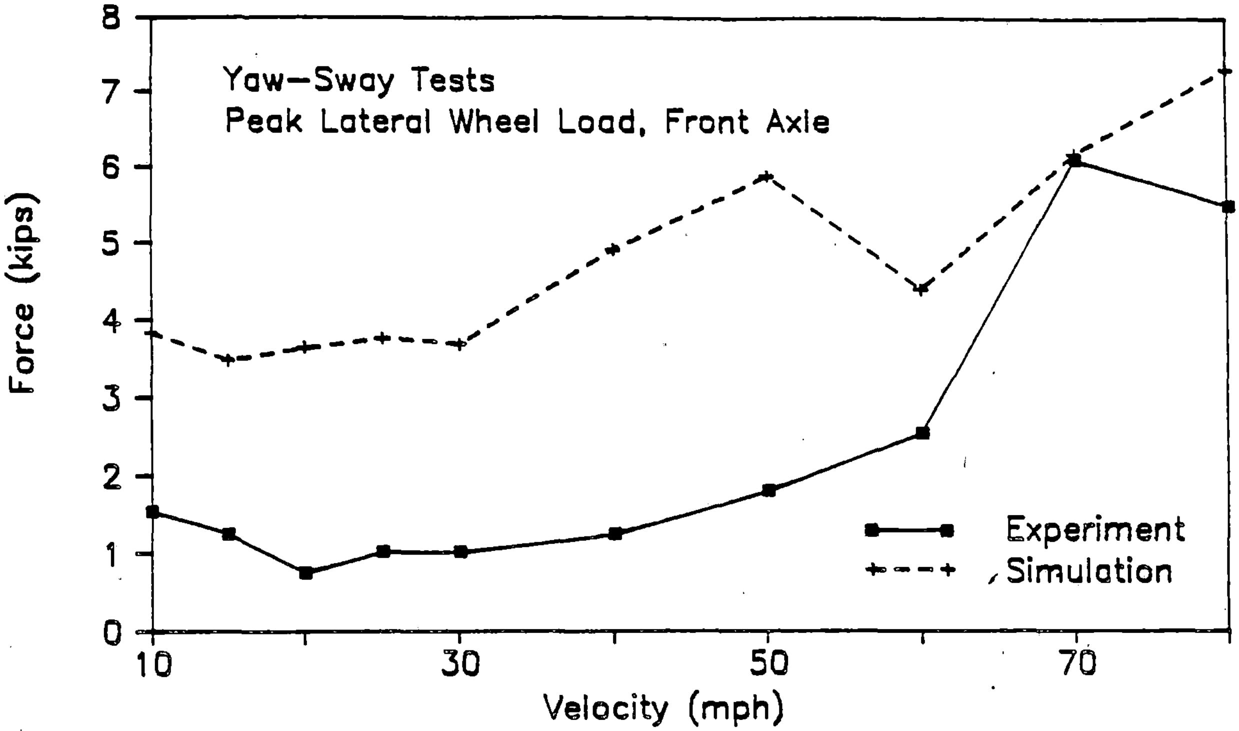

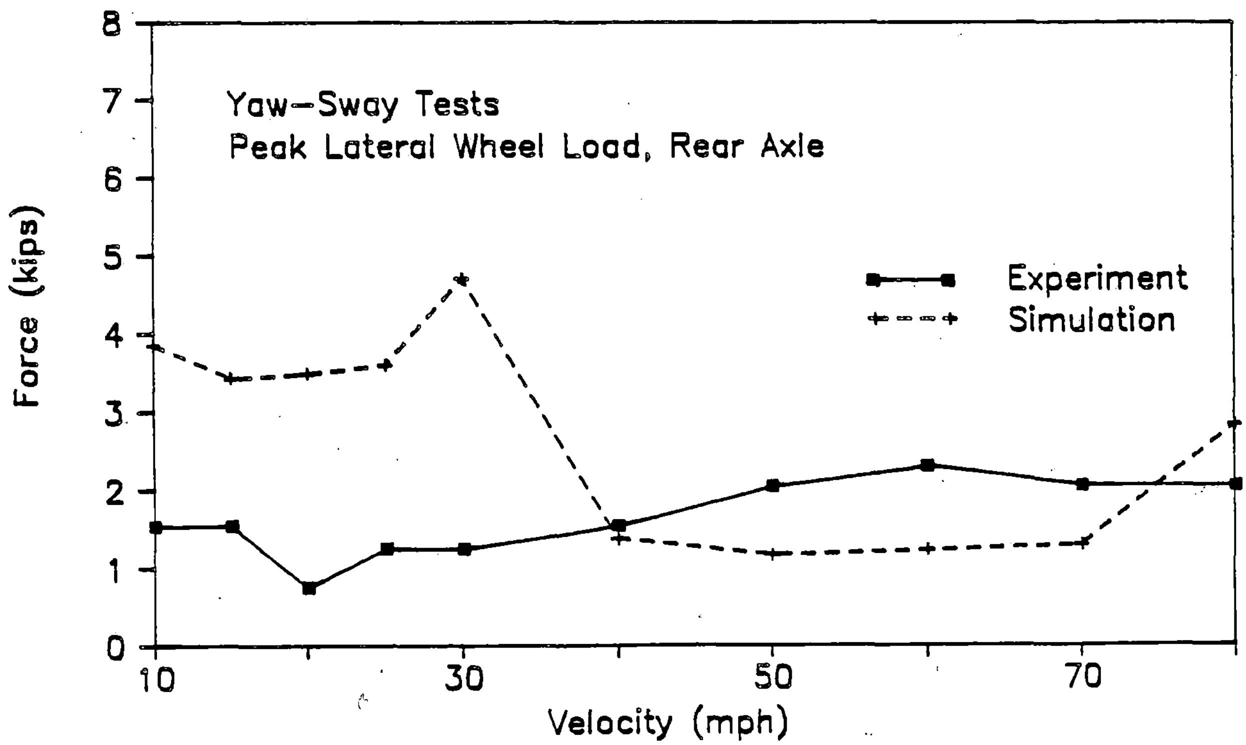

FIGURE 3-12. YAW-SWAY TEST PEAK LATERAL WHEEL LOADS

In summary, the model indicates that a possible rear-axle lateral resonance condition exists for levels of wheel-rail friction of 0.5, a condition that is not observed in the test data. The resonance is a strong function of wheel-rail friction and is not present when values of friction are reduced to 0.4. Both the model and the test data indicate that axle L/V ratios for all speeds are less than 1.0, a value below the value (1.3) nominally associated with severe wheel climb.

Simulations were also conducted with the vehicle to determine its response to 78-foot wavelength periodic perturbations of 1.25-inch amplitude, which should excite vehicle yaw motion. The results of these simulations for baseline conditions are summarized in terms of axle L/V ratios in Table 3-2. These data indicate axle L/V ratios of less than 1.0 at speeds of 20 mph to 70 mph and axle L/V ratios of less than 1.3 at 80 mph.

3.5 VEHICLE RESPONSE TO CURVED TRACK PERTURBATIONS

The vehicle was tested on a section of 12-degree curved track which had a combination of 1.0-inch amplitude in-phase alignment and gage variation coupled with 0.5-inch amplitude crosslevel variations, as prescribed by Chapter XI. This track geometry is designed to excite vehicle lateral and roll motion while negotiating a curve. The vehicle wheel force measurements for speeds of 14 mph to 23 mph are summarized in Table 3-3. Tests were not conducted above 23 mph because unsafe conditions with significant wheel climb were approached. The test data in terms of peak lateral wheel loads on the front axle and axle L/V ratios are plotted in Figures 3-13 and 3-14, respectively. In both figures, the test data are compared with model results computed for speeds of 14 mph to 28 mph, the speed at which the model indicated excessive wheel climb. In both the experiment and the

TABLE 3-2. VEHICLE RESPONSE TO 78-FOOT SINUSOIDAL ALIGNMENT PERTURBATIONS

	Velocity (mph)	Experimental Results	Model Results $\mu = 0.5$
Front Axle L/V Sum	20	-	.519
	30	-	.518
	40	-	.545
	50	-	.593
	60	-	.679
	70	-	.862
	80	-	1.023
Rear Axle L/V Sum	20	-	.433
	30	-	.408
	40	-	.393
	50	-	.396
	60	-	.238
	70	-	.886
	80	-	1.242

TABLE 3-3. VEHICLE RESPONSE TO ALIGNMENT AND CROSSLEVEL PERTURBATIONS ON 12-DEGREE CURVED TRACK

	Velocity (mph)	Experimental Results	Model Results $\mu = 0.5$	Model Results $\mu = 0.4$
Maximum Lateral Load, Wheel 1 (lbf)	14	5800	5366	5288
	16.5	7600	6383	6557
	18.5	7400	7549	7133
	21	7400	7952	7857
	23	8000	8444	8322
	25.5		8989	8970
	28		9357	9237
Maximum Lateral Load, Wheel 2 (lbf)	14	2700	3303	2794
	16.5	3700	3296	2782
	18.5	4000	3272	2764
	21	3700	3261	2732
	23	3300	3234	2708
	25.5		3262	3151
	28		3172	2781
Front Axle L/V Sum	14	1.15	1.046	.888
	16.5	1.35	1.056	.926
	18.5	1.35	1.083	.963
	21	1.65	1.157	1.033
	23	1.60	1.207	1.066
	25.5		1.303	1.142
	28		1.265	1.165
Rear Axle L/V Sum	14	.75	1.053	.870
	16.5	.78	1.035	.784
	18.5	.80	1.004	.738
	21	.87	.970	.712
	23	.90	.938	.704
	25.5		.900	.729
	28		.954	.806
Minimum Percent Vertical Load (%)	14	53	68	66
	16.5	46	66	65
	18.5	46	62	63
	21	46	57	59
	23	34	57	59
	25.5		51	57
	28		41	52

TABLE 3-3. VEHICLE RESPONSE TO ALIGNMENT AND CROSSLEVEL PERTURBATIONS ON 12-DEGREE CURVED TRACK (CONTINUED)

	Velocity (mph)	Experimental Results	Model Results $\mu = 0.5$	Model Results $\mu = 0.4$
L/V Ratio, Wheel 1	14	.81	.564	.535
	16.5	.80	.610	.630
	18.5	.85	.711	.671
	21	.80	.779	.730
	23	.83	.848	.757
	25.5		.881	.805
	28		.846	.842
L/V Ratio, Wheel 2	14	.60	.522	.428
	16.5	.67	.519	.427
	18.5	.70	.516	.427
	21	.95	.513	.426
	23	.92	.509	.425
	25.5		.507	.424
	28		.507	.423
L/V Ratio, Wheel 3	14	.50	.466	.411
	16.5	.52	.462	.420
	18.5	.50	.461	.409
	21	.47	.467	.409
	23	.50	.465	.408
	25.5		.440	.434
	28		.487	.497
L/V Ratio, Wheel 4	14	.35	.587	.505
	16.5	.37	.573	.463
	18.5	.40	.549	.443
	21	.47	.533	.433
	23	.52	.510	.419
	25.5		.551	.399
	28		.665	.379

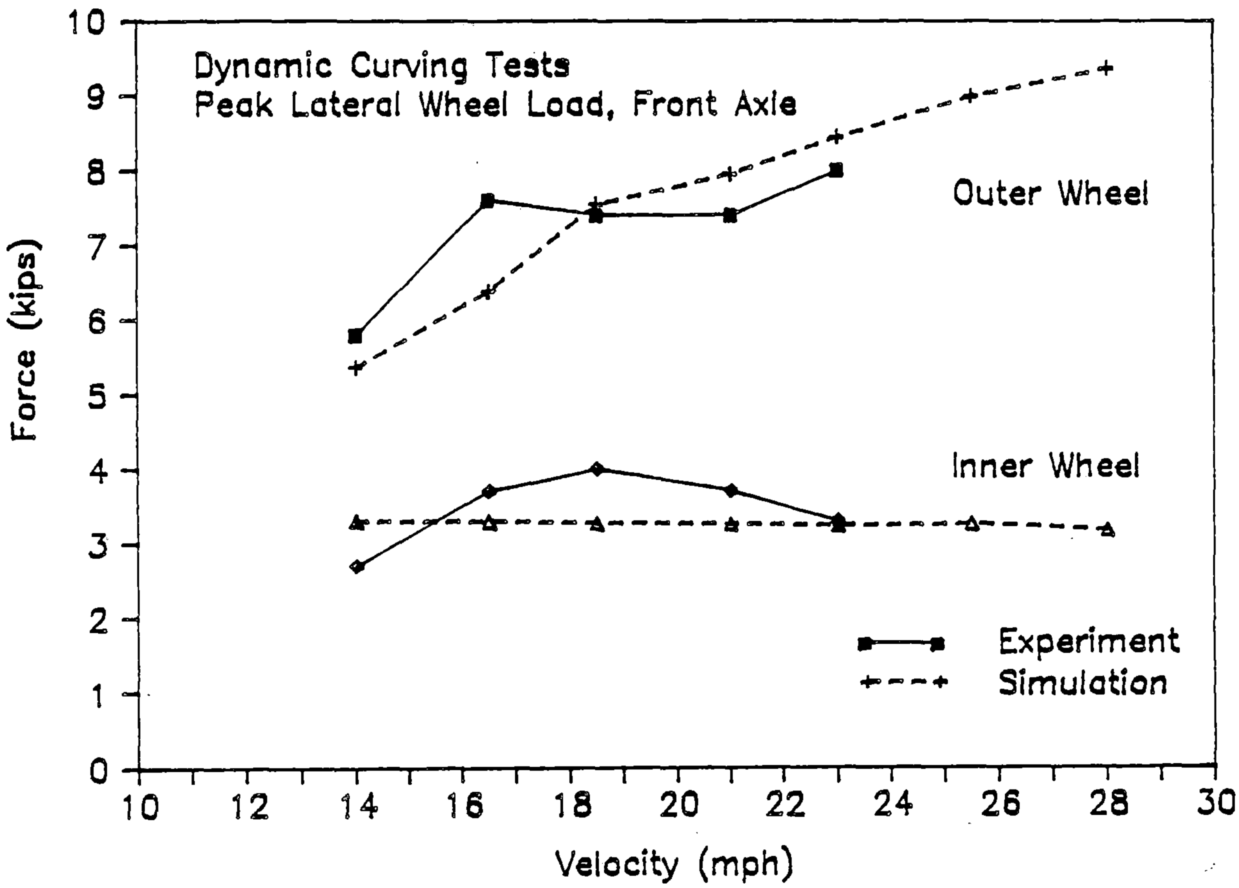

FIGURE 3-13. DYNAMIC CURVING TEST PEAK LATERAL WHEEL LOADS ON FRONT AXLE

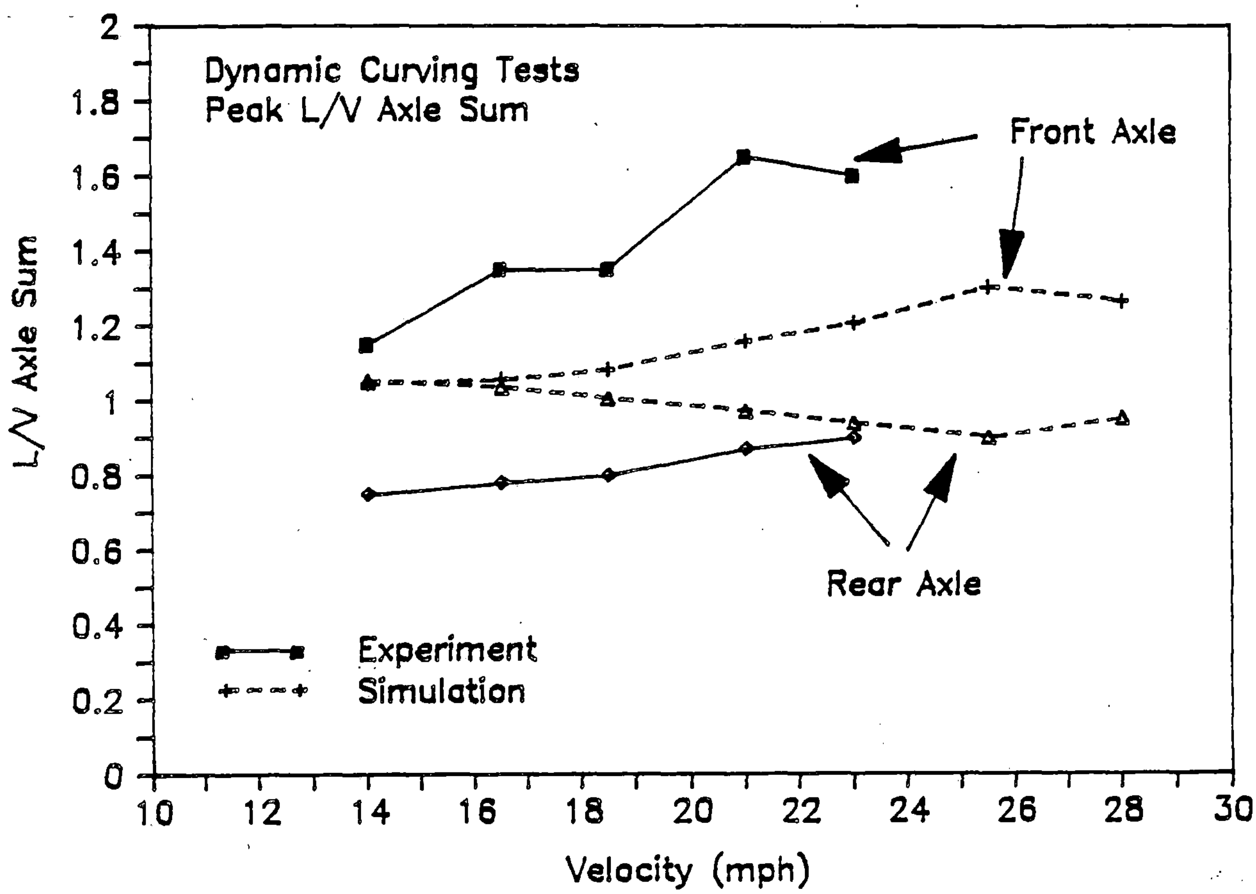

FIGURE 3-14. DYNAMIC CURVING TEST PEAK L/V AXLE SUM

model, the peak lateral force on the inner wheel of the front axle remained relatively constant at approximately 3,500 pounds as the speed increased. As speed increased from 14 mph to 25 mph, the speed at which the tests were stopped, the peak force on the outer wheel increased from 5,500 pounds to 8,000 pounds. The test data and model data are in good agreement on the peak lateral forces as a function of speed.

As shown in Figure 3-14 the test data indicate higher L/V ratios than do the model predictions. The measured front-axle L/V ratios increase from 1.15 at 14 mph to above 1.6 at 23 mph, while the L/V ratios predicted by the model increase from 1.05 at 14 mph to above 1.3 at 28 mph. Since the lateral loads predicted by the model and measured in the tests are in good agreement, higher L/V ratios in the measured data are primarily attributable to the lower vertical loads, i.e. more wheel unloading, in the measured data, as shown in Table 3-3. Both the test data and the model predictions indicate that significant wheel climb occurs on the outer wheel as the speed is increased beyond 20 mph and that unsafe wheel climb conditions are approached at 23 mph in the test and at 28 mph in the model.

3.6 VEHICLE RESPONSE TO CROSSLEVEL PERTURBATIONS

The vehicle was tested on track with 0.75-inch amplitude crosslevel perturbations repeated every 39 feet. The perturbations are out of phase on the right and left rails to excite roll and twist in the car. In Table 3-4, test data are summarized for speeds varying from 36 mph to 60 mph and compared with model data. In Figure 3-15, the vehicle roll angle is plotted as a function of speed where the roll angles in both the test data and model are noted to increase from approximately 1.6 degrees to 2.1 degrees over the speed range. The roll angles for the unloaded vehicle are relatively small,

TABLE 3-4. VEHICLE RESPONSE TO CROSSLEVEL PERTURBATIONS

	Velocity (mph)	Experimental Results	Model Results
Minimum Percent Vertical Load, Wheel 1 (%)	15	-	75
	36	53	69
	44	42	55
	52	40	61
	60	42	60
	75	-	55
Minimum Percent Vertical Load, Wheel 2 (%)	15	-	76
	36	62	62
	44	45	52
	52	48	59
	60	50	60
	75	-	48
Minimum Percent Vertical Load, Wheel 3 (%)	15	-	80
	36	55	58
	44	43	61
	52	36	57
	60	32	58
	75	-	57
Minimum Percent Vertical Load, Wheel 4 (%)	15	-	80
	36	65	47
	44	55	62
	52	62	61
	60	58	62
	75	-	56
Carbody Peak-to-Peak Roll Angle (degrees)	15	-	1.53
	36	1.7	1.69
	44	1.8	1.73
	52	1.8	1.80
	60	2.1	1.93
	75	-	2.17

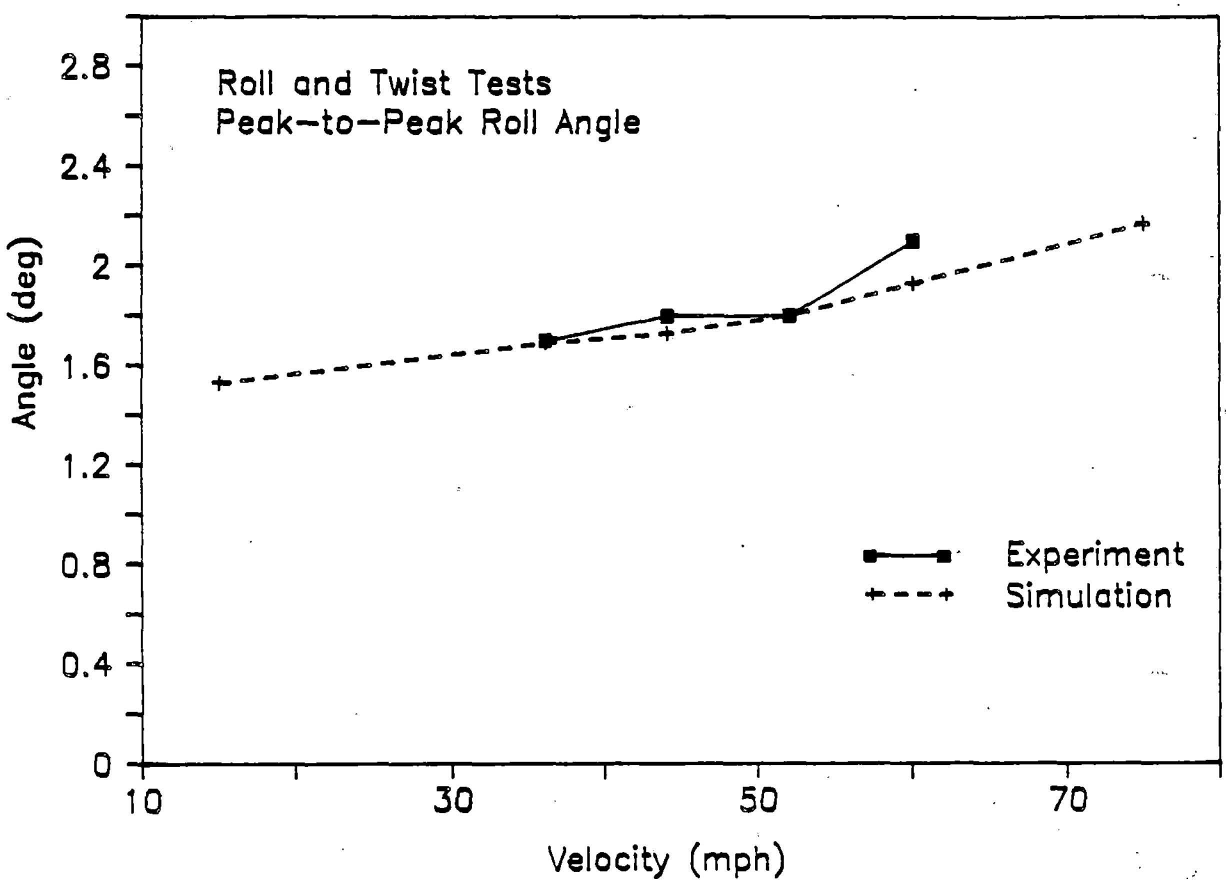

FIGURE 3-15. ROLL-TWIST TEST PEAK-TO-PEAK ROLL ANGLE

and the unloaded vehicle is not excited significantly by the crosslevel perturbations.

3.7 VEHICLE RESPONSE TO VERTICAL PERTURBATIONS

Tests were also conducted on the vehicle over track with periodic 39-foot in-phase 0.75-inch amplitude vertical perturbations designed to excite vehicle bounce and pitch. In Figure 3-16, the percent of wheel unloading measured as a function of speed in the tests is plotted and compared with model predictions. Both the test and model data indicate that as speed increases the percent of wheel unloading increases with full unloading occurring at 70 mph.

In Table 3-5, test data for the unloaded vehicle traversing a single vertical bump with a 2-inch amplitude and 36-foot length are summarized. The test data, as well as model predictions, indicate that as the speed is increased to 40 mph complete wheel unloading occurs. The test and model data closely agree.

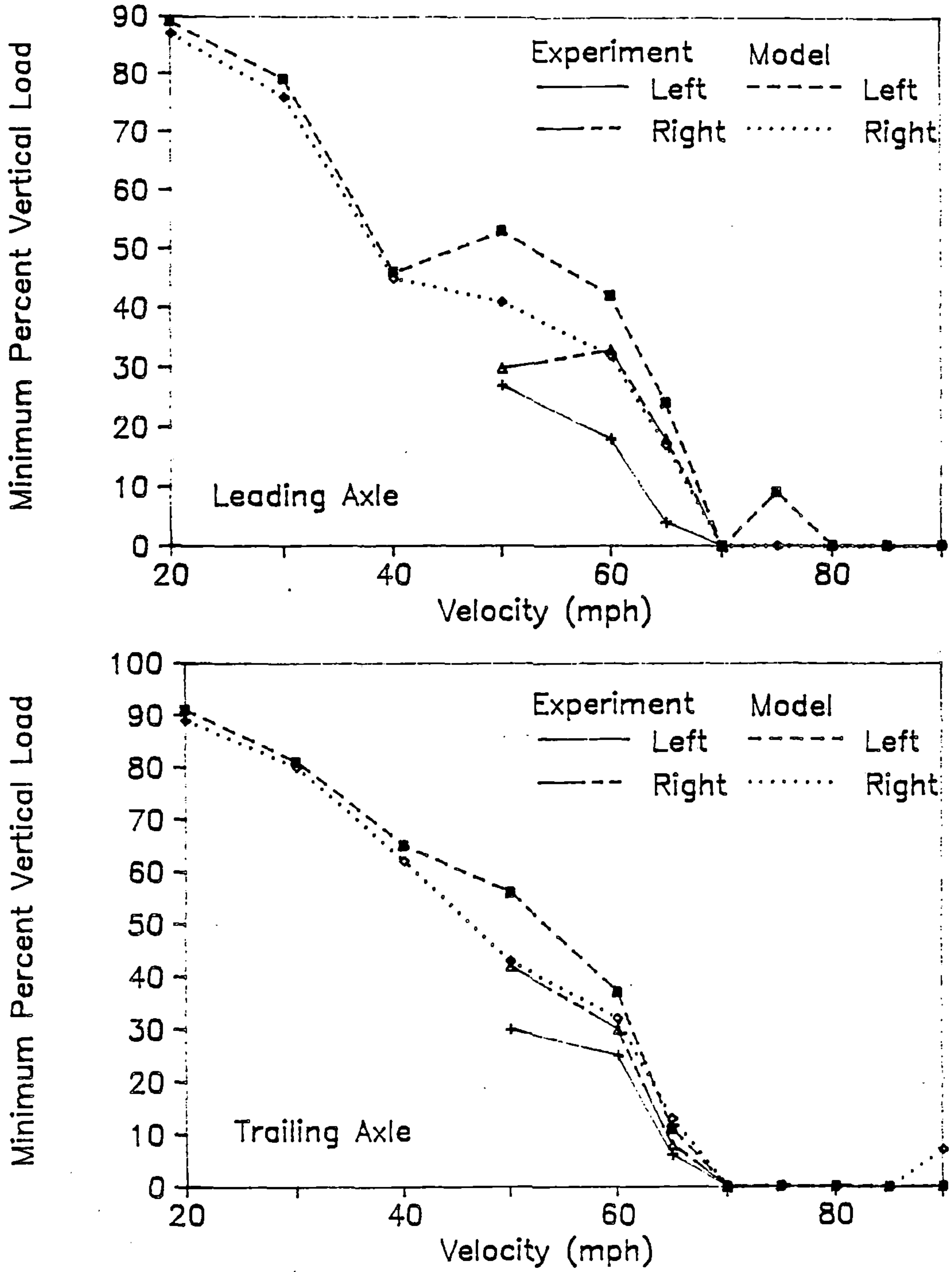

FIGURE 3-16. BOUNCE-PITCH TEST MINIMUM PERCENT VERTICAL WHEEL LOAD

TABLE 3-5. VEHICLE RESPONSE TO VERTICAL PUMP

	Velocity (mph)	Experimental Results	Model Results
Minimum Percent Vertical Load, Front Axle (%)	20	-	26
	30	20	5
	40	0	0
	50	14	0
	60	5	0
	70	-	0
	80	-	0
Minimum Percent Vertical Load, Rear Axle (%)	20	-	18
	30	24	5
	40	0	5
	50	5	5
	60	3	0
	70	-	0
	80	-	0
Maximum Percent Vertical Load, Front Axle (%)	20	-	175
	30	-	197
	40	-	350
	50	-	280
	60	-	210
	70	-	250
	80	-	330
Maximum Percent Vertical Load, Rear Axle (%)	20	-	160
	30	-	190
	40	-	290
	50	-	230
	60	-	220
	70	-	280
	80	-	310

4. SUMMARY AND CONCLUSIONS

4.1 UNLOADED VEHICLE DYNAMIC PERFORMANCE

Extensive test data have been obtained and processed for the unloaded two-axle prototype vehicle operating over Chapter XI prescribed track conditions. Computer simulations have also been conducted to determine vehicle performance. The results of these studies have indicated the following:

(1) Hunting Speed on Unperturbed, Tangent Track

(a) Field tests indicated a hunting speed above 90 mph.

(b) Simulations indicated a hunting speed above 100 mph.

(2) Constant Speed Negotiation of Unperturbed, Constant Radius Curved Track

(a) Field tests indicated maximum wheel L/V ratios of 0.1, 0.51, and 0.6 on 5-degree, 7.5-degree and 10-degree curves, respectively.

(b) Simulations indicated maximum wheel L/V ratios of 0.05, 0.36, and 0.51 on 5-degree, 7.5-degree and 10-degree curves respectively. Additional simulations indicated maximum wheel L/V ratios of less than 0.6 for curves from 5-degree to 15-degree.

(3) Yaw-Sway Tests on Track with Sinusoidal Alignment Perturbations

(a) Field tests conducted from 10 mph to 80 mph indicated a maximum axle L/V ratio of 0.95.

(b) Simulations indicated a maximum axle L/V ratio of 0.98 between 10 mph to 80 mph.

(4) Dynamic Curving on Curved Track with Alignment and Crosslevel Perturbations

(a) Field tests indicated axle L/V ratios above 1.35 above 20 mph and were terminated at 23 mph.

(b) Simulations indicated axle L/V ratios above 1.2 at 23 mph and severe wheel climb at 28 mph.

(5) Rock and Roll on Crosslevel Track Perturbations

(a) Field tests indicated a maximum carbody roll angle of 2.1 degrees between 36 mph and 60 mph.

(b) Simulations indicated a maximum carbody roll angle of 2.2 degrees between 15 mph to 75 mph.

(6) Bounce and Pitch on Vertical Sinusoidal Track Perturbations

(a) Field tests have shown full wheel periodic unloading above 70 mph.

(b) Simulations have indicated full wheel unloading above 70 mph for short time periods corresponding to a distance of approximately three feet.

(7) Bounce and Pitch in Negotiation of a Single Vertical Bump

(a) Field tests have shown full wheel unloading above 40 mph.

(b) Simulations have indicated full wheel unloading above 40 mph for short time periods corresponding to a travel distance of less than four feet.

In both field tests and simulations, the unloaded two-axle vehicle approached an unsafe condition associated with severe wheel climb only in the dynamic curving tests, where tests were stopped at 23 mph. These track conditions represent severe conditions in which cars equipped with standard three-piece freight trucks would also be expected to experience severe wheel climb conditions at low speeds, as shown by the tests described in reference [4].

Additional simulations have indicated that the vehicle hunting speed decreases significantly, to 33 mph, if the hydraulic damper effectiveness is reduced to 25 percent of its design value. Thus, an effective hydraulic damper is necessary to maintain a hunting speed in excess of 90 mph. Simulations have also shown that the specific performance of the vehicle in terms of L/V ratios on curved and/or perturbed track can be strongly influenced by both wheel-rail profiles and by wheel-rail friction coefficients. However, the variations in both wheel-rail profiles and friction coefficients from the baseline values considered in the study did not result in a change from safe to unsafe operating conditions.

4.2 MODEL VALIDATION

The two-axle unloaded baseline vehicle model has agreed closely with field test data for all tests conducted on vertical and crosslevel track perturbations with an indication within ± 5 mph of when wheel unloading conditions are reached. These series of tests which excite vehicle bounce, pitch and roll motions primarily exercise the vehicle suspensions and are not strongly influenced by wheel-rail creep forces. The close agreement between the model and test results provides strong confidence in the modeling and parameter values of the vehicle vertical suspension and carbody mass and inertia parameters.

The vehicle model has also predicted trends and identified maximum L/V ratios which closely agree with field tests that excite the vehicle laterally through wheel-rail creep and the vehicle's lateral and longitudinal suspension. However, the lateral plane model has not agreed closely with field test data in a number of specific measurements, including the lateral suspension stroke in sinusoidal alignment tests and the wheelset alignment in 10-

degree steady-state curving tests. For both of these conditions, the model results were shown to be sensitive to changes in wheel-rail friction coefficients, as well as wheel-rail profile. While these differences occurred, it is also noted that in dynamic curving severe wheel climb conditions were identified by both the field tests and simulations at comparable speeds. While the model validation with respect to detailed wheel-rail creep force prediction under flanging conditions requires some additional attention, in the prediction of general trends and in the identification of safety limiting conditions, the model and field test data are in good agreement.

4.3 CONCLUSIONS AND RECOMMENDATIONS

The study has shown the importance of a complementary evaluation through field tests and computer analyses of the safety performance of rail vehicles. Although field tests are indispensable in vehicle evaluation, they are necessarily limited by time and cost to a specified number of tests representing the behavior of the vehicle for a given set of operating and track conditions on the day of the test. Analyses are valuable to explore vehicle operating conditions which may result from changes in vehicle parameters such as friction or damping in suspension elements, wear, changes in wheel profile, and variations in vehicle loading, as well as to variations of track conditions such as changes in track profile due to wear, lubrication, and track perturbations such as alignment wavelengths not included in tests. The effectiveness of an analytical model depends strongly on its degree of validation by experimental data. The model developed in the study has been shown to generally agree with field data in terms of predicting trends and identifying cases where safety limits are aproached; however, the model did not have universally close agreement with the field data in terms of predicting detailed longitudinal and lateral creep forces for conditions involving substantial flanging. Further effort to assess the basic wheel-rail model under flanging conditions is recommended in terms of acquiring additional field test data, as well as reviewing the wheel-rail model formulation for these cases. Additionally, all of the comparisons between the model and test data have corresponded to the lightly loaded wheel conditions (7,000 lbs) for the unloaded car. Further effort is required to assess in detail the validity of the wheel-rail model under wheel loads appropriate for a fully loaded vehicle, particularly for strongly flanging conditions.

5. REFERENCES

1. "Chapter XI, Service Worthiness Tests and Analysis for New Freight Cars," Draft Document RA 87-03-0175, AAR Manual of Standards and Recommended Practice, Association of American Railroads, March 1987.

2. Ehrenbeck, R. and Polcari, S., "Vehicle/Track Interaction Assessment Techniques," Report No. DOT/FRA/ORD-84/01.1, Federal Railroad Administration, March 1984.

3. Coltman, M., Brantman, R., Tong, P., "A Description of the Tests Conducted and Data Obtained During the Perturbed Track Test," Report No. FRA/ORD-80/15, Federal Railroad Administration, June 1980.

4. Coltman, M. and Weinstock, H., "Vehicle/Track Interaction Test at Bennington, N.H.," Final Report, DOT/FRA/TSC, Federal Railroad Administration, January 1986.

5. Blader, F. B. and Mealy, G. L., "Analytic Studies of the Effects of Track Geometry Variation," Report No. DOT/FRA/ORD-85-01, Federal Railroad Administration, July 1985.

6. "Track Tests Results Based upon Chapter XI," Summary Report Under FRA Task Order 20, Association of American Railroads, August 1987.

7. Weinstock, H., "Wheel Climb Derailment Criteria for Evaluation of Rail Vehicle Safety," ASME Paper No. 84-WA/RT-1, December 1984.

8. Sweet, L. M. and Karmel, A., "Wheelclimb Derailment Processes and Derailment Criteria," Final Report No. MEA-1618 (Contract No. DOT-TSC-1603) Princeton University, August 1983.

9. Matsudaria, T., "Dynamics of High Speed Rolling Stock," Japanese National Railway Technical Research Institute Quarterly Report, Special Issue, 1963.

10. Koci, H. H. and Swenson, C. A., "Locomotive Wheel-Rail Loading - A Systems Approach," Electromotive Division, General Motors, LaGrange, IL, Proceedings of the Heavy Haul Railways Conference, Perth, Australia, February 1978.

11. "The Car and Locomotive Cyclopedia of American Practices," 5th Edition, Simmons-Boardman, 1984.

12. Wolf, E. J. and Stec, F. F., "Single Axle Suspensions for Intermodel Freight Cars," Conference Proceedings, The Economics and Performance of Freight Car Trucks, Montreal, October 1983.

13. Longo, T. A., "A General Simulation Procedure for Rail Vehicle Dynamics," S.M. Thesis, Massachusetts Institute of Technology, 1986.

14. Fancher, P. S., et al., "Measurement and Representation of Truck Leaf Springs," SAE Paper No. SAE/SP.80/475, 1980.

15. Kalker, J. J., "Survey of Wheel-Rail Rolling Contact Theory," Journal of Vehicle System Dynamics, Vol. 5, 1979.

16. Wormley, D. N., Hedrick, J. K., Nagurka, M. L., "Analysis of Rail Transit Vehicle Curving Performance," DOT Report No. UMTA/MA/06/0025/84/1, 1984.

17. Elkins, J. A. and Eickhoff, B. M., "Advances in Nonlinear Wheel/Rail Force Predictions and Their Validation," Journal of Dynamic Systems Measurement and Control, Vol. 104, No. 2, June 1982.

18. O'Connell, S. P., "The Influence of Heavy Vehicle Dynamics on Pavement Response," S.M. Thesis, Massachusetts Institute of Technology, 1986.

Appendix A

Kinematic Analysis

Several frames of reference are used to describe the motion of the carbody and wheelsets in the two-axle vehicle dynamic curving model. The position of the carbody center of mass is expressed with respect to the ideal "deterministic" track frame, which is a frame which undergoes curving and superelevation rotations like the actual track, but which is not subjected to crosslevel perturbations. Since the wheel/rail mechanics are most naturally described in the plane of the track, the positions of the wheelsets are expressed relative to the local track plane which rolls relative to the deterministic track frame.

To achieve the rotational equations of each element in the simplest form, it is necessary to express the motion of each object in a frame of reference which is a principal axis system of the body. Such a principal axis system may or may not be fixed with respect to the body. If the body possesses rotational symmetry as a wheelset does, then the body has many principal axis systems.

In the following, it is assumed that the velocity of the rail vehicle is constant. The small angle approximation is frequently used, and terms of second order or higher in angles are neglected in the final results. Also, the product of a small angle and the time derivative of a small angle are considered to be negligible. Terms consisting of the product of two small angular velocities are neglected in acceleration relations.

A.1 The Physics of Coordinate Rotations

In Newton's second law, the relation

$$\vec{F} = \frac{d\vec{P}}{dt} = m\vec{a}$$

is valid only when the acceleration is referred to an inertial coordinate frame, where $\vec{F}$ is the force acting on the body, $\vec{P}$ is the momentum of the body, m is the mass, and $\vec{a}$ is the inertial acceleration of the body. This is the governing equation for translational motion.

The corresponding equation for rotational motion is given by:

$$\vec{\tau} = \frac{d\vec{H}}{dt} = \frac{d}{dt}\left(\bar{I}\vec{\omega}\right)$$

where $\vec{\tau}$ is the torque acting on the body, $\vec{H}$ is the angular momentum, $\bar{I}$ is the moment of inertia tensor, and $\vec{\omega}$ is the instantaneous angular velocity of the body with respect to an inertial frame. If the angular momentum vector is expressed in a coordinate system which is a principal axis system of the body, then the off-diagonal elements of the inertia tensor are zero and the expression may be simplified. Furthermore, the inertias are then time invariant. However, this will generally be the case only when a transformation to a noninertial frame of reference has been made.

Consider a coordinate system, F, which is rotating with respect to inertial space. This angular velocity may be expressed in the coordinates of the F system, as follows:

$$^{I}\vec{\omega}^{F} = \begin{pmatrix} \omega_{FX} \\ \omega_{FY} \\ \omega_{FZ} \end{pmatrix}_{\{F\}}$$

The notation adopted here should be explained, as it will be used extensively. The I and F superscripts are used to indicate that a velocity or acceleration refers to the motion of the F frame relative to the I frame. In the case of a position vector such as

$$^{I}\vec{R}^{F}$$

it is understood that the notation indicates the vector from the origin of the I frame to that of the F frame. Column vectors will often be subscripted with a letter or number indicating in which frame of reference the vector is expressed. Thus, the $\{F\}$ below indicates that the component values are expressed in terms of the F frame coordinates.

$$\vec{u} = \begin{pmatrix} u_X \\ u_Y \\ u_Z \end{pmatrix}_{\{F\}} = u_X \hat{\imath}_F + u_Y \hat{\jmath}_F + u_Z \hat{k}_F$$

The fundamental law giving the inertial velocity of a point Q, expressed with respect to the rotating frame of reference F, is as follows:

$$\boxed{\frac{d}{dt}\left({}^{I}\vec{R}^{Q}\right) = \frac{d}{dt}\left({}^{I}\vec{R}^{F}\right) + \frac{\partial}{\partial t}\left({}^{F}\vec{R}^{Q}\right) + {}^{I}\vec{\omega}^{F} \times {}^{F}\vec{R}^{Q} \qquad \text{(A.1.1)}}$$

where, on the right hand side, the ordinary derivative gives the time rate of change in the inertial system, the partial derivative is the simple time derivative with respect to the rotating system, and the angular velocity is that of the rotating system relative to the inertial frame. In component form,

$$^{I}v_X^Q = {}^{I}v_X^F + {}^{F}v_X^Q + z\omega_{FY} - y\omega_{FZ}$$

$$^{I}v_Y^Q = {}^{I}v_Y^F + {}^{F}v_Y^Q + x\omega_{FZ} - z\omega_{FX}$$

$$^{I}v_Z^Q = {}^{I}v_Z^F + {}^{F}v_Z^Q + y\omega_{FX} - x\omega_{FY}$$

For rotational motion, the angular velocity of the body relative to inertial space is projected onto a principal axis coordinate system of the body. The angular momentum is thus easily found. For all bodies except the wheelsets, the frame of reference in which the motion will be expressed is the body-fixed coordinate system. In the case of the wheelsets, the appropriate frame of reference is a principal axis system which does not spin with the wheelset.

If frame F is a principal axis system of the body, and G is a body-fixed principal axis system, then the angular momentum is given by:

$$
{}^{I}\vec{H}^{G} = \begin{pmatrix} I_X \omega_{GX} \\ I_Y \omega_{GY} \\ I_Z \omega_{GZ} \end{pmatrix}_{\{F\}}
$$

For the wheelset dynamic equations, the objective is to calculate the torque $\vec{\tau}$ in the frame F, since it is more convenient than the spinning body-fixed system G. Using (A.1.1),

$$
\boxed{\vec{\tau} = \begin{pmatrix} I_X \dot{\omega}_{GX} \\ I_Y \dot{\omega}_{GY} \\ I_Z \dot{\omega}_{GZ} \end{pmatrix}_{\{F\}} + \begin{pmatrix} I_Z \omega_{FY} \omega_{GZ} - I_Y \omega_{FZ} \omega_{GY} \\ I_X \omega_{FZ} \omega_{GX} - I_Z \omega_{FX} \omega_{GZ} \\ I_Y \omega_{FX} \omega_{GY} - I_X \omega_{FY} \omega_{GX} \end{pmatrix}_{\{F\}} \qquad \text{(A.1.2)}}
$$

If the F frame is identical to the G frame, as is the case for the carbody:

$$
\boxed{\vec{\tau} = \begin{pmatrix} I_X \dot{\omega}_{GX} \\ I_Y \dot{\omega}_{GY} \\ I_Z \dot{\omega}_{GZ} \end{pmatrix}_{\{G\}} + \begin{pmatrix} (I_Z - I_Y) \omega_{GY} \omega_{GZ} \\ (I_X - I_Z) \omega_{GX} \omega_{GZ} \\ (I_Y - I_X) \omega_{GX} \omega_{GY} \end{pmatrix}_{\{G\}} \qquad \text{(A.1.3)}}
$$

The translational acceleration of an object expressed in the coordinates of a rotating reference frame must also be considered. The time differentiation operation implied in (A.1.1) may be applied twice to the position of a point Q, measured with respect to a frame with origin F located at position ${}^I\vec{R}^F$ and rotating at an angular velocity ${}^I\vec{\omega}^F$ relative to inertial space. With $\vec{v}_{rel}$ and $\vec{a}_{rel}$ corresponding to the relative motion of Q with respect to the frame F, the following acceleration formula is found:

$$\boxed{\begin{aligned}\frac{d^2}{dt^2}\left({}^I\vec{R}^Q\right) = \frac{d^2}{dt^2}\left({}^I\vec{R}^F\right) &+ \vec{a}_{rel} + 2\,{}^I\vec{\omega}^F \times \vec{v}_{rel} \\ &+ {}^I\dot{\vec{\omega}}^F \times {}^F\vec{R}^Q + {}^I\vec{\omega}^F \times \left({}^I\vec{\omega}^F \times {}^F\vec{R}^Q\right)\end{aligned} \qquad \text{(A.1.4)}}$$

In component form,

$$\begin{aligned}{}^Ia_X^Q = {}^Ia_X^F + {}^Fa_X^Q &+ 2(v_Z\omega_{FY} - v_Y\omega_{FZ}) + z\dot{\omega}_{FY} - y\dot{\omega}_{FZ} \\ &+ y\omega_{FX}\omega_{FY} + z\omega_{FX}\omega_{FZ} - x({\omega_{FY}}^2 + {\omega_{FZ}}^2)\end{aligned}$$

$$\begin{aligned}{}^Ia_Y^Q = {}^Ia_Y^F + {}^Fa_Y^Q &+ 2(v_X\omega_{FZ} - v_Z\omega_{FX}) + x\dot{\omega}_{FZ} - z\dot{\omega}_{FX} \\ &+ z\omega_{FY}\omega_{FZ} + x\omega_{FX}\omega_{FY} - y({\omega_{FX}}^2 + {\omega_{FZ}}^2)\end{aligned}$$

$$\begin{aligned}{}^Ia_Z^Q = {}^Ia_Z^F + {}^Fa_Z^Q &+ 2(v_Y\omega_{FX} - v_X\omega_{FY}) + y\dot{\omega}_{FX} - x\dot{\omega}_{FY} \\ &+ x\omega_{FX}\omega_{FZ} + y\omega_{FY}\omega_{FZ} - z({\omega_{FX}}^2 + {\omega_{FY}}^2)\end{aligned}$$

In practice, this equation is applied repeatedly through successive transformations to achieve the acceleration of a complicated motion with respect to an inertial frame of reference.

A.2 System Transformations

Two distinct motions must be examined in the transformation from inertial coordinates to the deterministic track frame. The first is a rotation about the vertical axis due to the curvature of the track in vehicle curving situations. The second is a rotation about the longitudinal axis at the inside rail due to the track superelevation. A further rotation about the track centerline due to the crosslevel perturbation is necessary to describe the perturbed track plane. Finally, the track surface perturbation is a vertical displacement of the actual track centerline relative to the deterministic track plane. The three body rotations then follow.

Figure A.1 illustrates the six coordinate rotations used to describe the most complicated system, the wheelsets. The crosslevel rotation is not used for the carbody system.

Before proceeding further, a discussion of our right-handed coordinate system is required. The $\hat{\imath}$ axes are oriented longitudinally parallel to the track, positive in the direction of motion of the vehicle; the $\hat{\jmath}$ axes are aligned across the track in the lateral direction, positive to the left when looking forward; and the $\hat{k}$ axes are oriented vertically, with the positive direction upward. The x direction is along the $\hat{\imath}$ axis, the y direction is along the $\hat{\jmath}$ axis, and the z direction is along the $\hat{k}$ axis. The particular coordinate systems under consideration have unit vectors which have been rotated in one or more ways with respect to the "pure" definitions above.

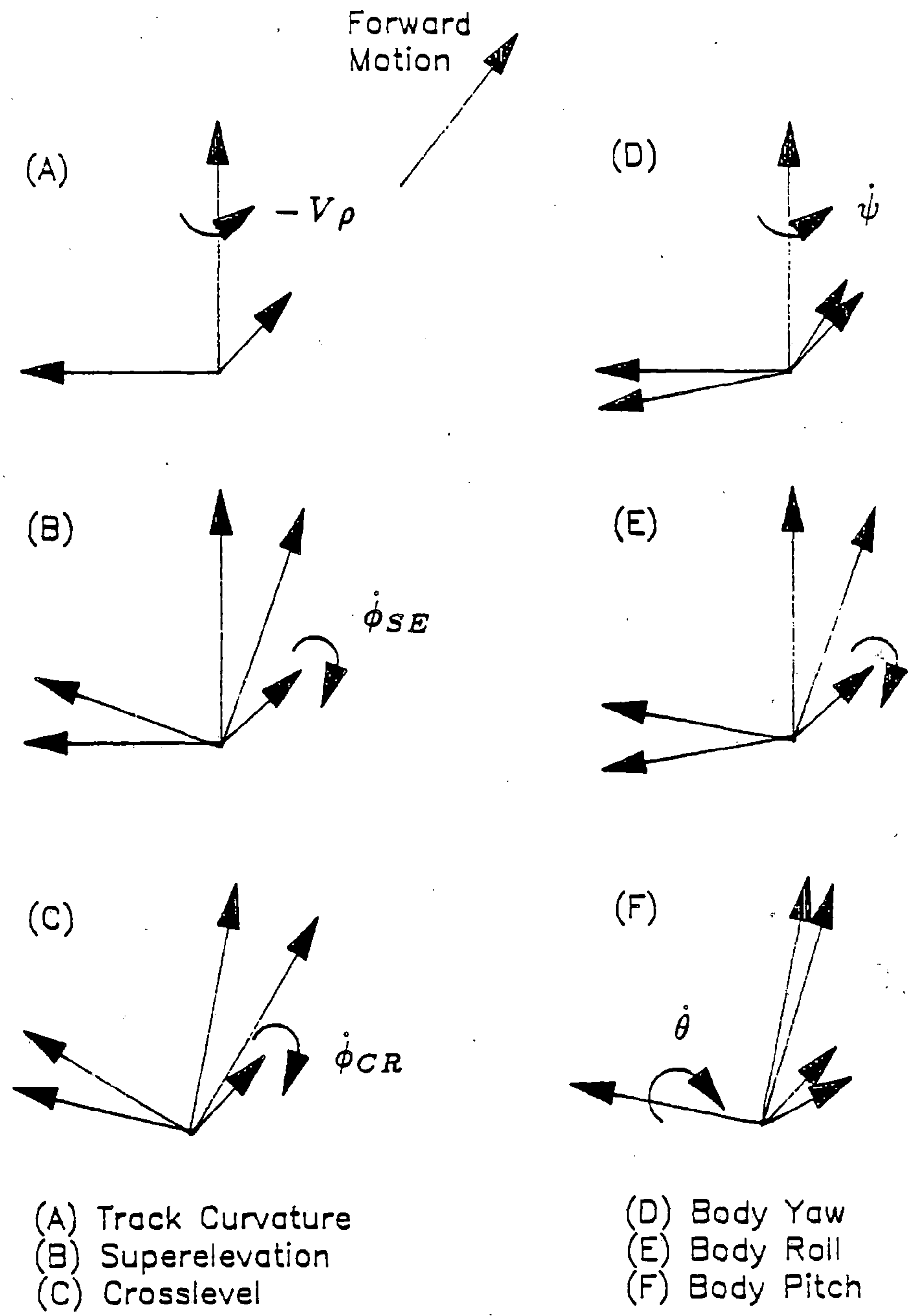

Figure A.1 Diagram showing the six coordinate rotations for the wheelset system. The other bodies do not include the perturbed track plane rotation.

A.2.1 Rotation of the D and P Track Frames

The rotational motions of the deterministic and track plane systems is developed in this section. Let the inertial system be denoted by the subscript I and the horizontal system, which curves with the track, be marked with the subscript H. The horizontal frame is rotating with respect to the inertial frame with an angular velocity which depends upon the vehicle velocity V and the curvature of the track ρ.

$$ {}^{I}\vec{\omega}^{H} = -V\rho\,\hat{k}_H = \begin{pmatrix} 0 \\ 0 \\ -V\rho \end{pmatrix}_{\{H\}} $$

The superelevated track frame S rolls with respect to the horizontal frame H at a rate given by the time rate of change of the superelevation angle. The origins of the two frames coincide at the top of the right rail of the ideal, deterministic track.

$$ {}^{H}\vec{\omega}^{S} = \dot{\phi}_{SE}\,\hat{\imath}_H $$

The coordinate rotation necessary to express a vector $\vec{u}$, expressed in H frame coordinates, in terms of S frame coordinates may be written in matrix form as follows, where the approximate matrix is obtained by considering the small angle approximation:

$$ \vec{u}_{\{S\}} = \begin{pmatrix} 1 & 0 & 0 \\ 0 & \cos(\phi_{SE}) & \sin(\phi_{SE}) \\ 0 & -\sin(\phi_{SE}) & \cos(\phi_{SE}) \end{pmatrix} \vec{u}_{\{H\}} $$

$$ \approx \begin{pmatrix} 1 & 0 & 0 \\ 0 & (1-\frac{1}{2}{\phi_{SE}}^2) & \phi_{SE} \\ 0 & -\phi_{SE} & (1-\frac{1}{2}{\phi_{SE}}^2) \end{pmatrix} \vec{u}_{\{H\}} $$

Since the matrix is an orthogonal transformation, the inverse operation of transforming from the S frame to the H frame may be found by simply taking the transpose of the matrix. Figure A.2 illustrates the basic track and wheelset coordinate systems in the absence of crosslevel perturbations.

The origin of the deterministic track frame D is located midway between the rails (assuming no track irregularities), and as it is fixed in the S system it has the same angular velocity with respect to inertial space as the S frame. Additionally, the S and D frame coordinate systems are perfectly aligned.

$$ {}^{I}\vec{\omega}^{D} = \begin{pmatrix} \dot{\phi}_{SE} \\ -\phi_{SE} V \rho \\ -(1 - \frac{1}{2}{\phi_{SE}}^{2}) V \rho \end{pmatrix}_{\{D\}} $$

Applying the small angle approximation,

$$ \boxed{ {}^{I}\vec{\omega}^{D} = \begin{pmatrix} \dot{\phi}_{SE} \\ 0 \\ -V\rho \end{pmatrix}_{\{D\}} \qquad {}^{I}\dot{\vec{\omega}}^{D} = \begin{pmatrix} \check{\phi}_{SE} \\ -\phi_{SE} V \dot{\rho} \\ -V\dot{\rho} \end{pmatrix}_{\{D\}} \qquad \text{(A.2.1)} } $$

As noted previously, the wheelsets are most naturally considered in reference frames which roll with the crosslevel of the track, a rotation about the track centerline. The sum of the superelevation and crosslevel rotations occurs frequently, and it is useful to define the total roll ϕ_{TR} of the track plane relative to the horizontal frame, as well as its derivatives, as follows:

$$ \begin{aligned} \phi_{TR} &= \phi_{SE} + \phi_{CR} \\ \dot{\phi}_{TR} &= \dot{\phi}_{SE} + \dot{\phi}_{CR} \\ \check{\phi}_{TR} &= \check{\phi}_{SE} + \check{\phi}_{CR} \end{aligned} $$

The inertial angular velocity of the track plane may be obtained as the sum of two vectors,

$$ {}^{I}\vec{\omega}^{P} = {}^{I}\vec{\omega}^{D} + {}^{D}\vec{\omega}^{P} $$

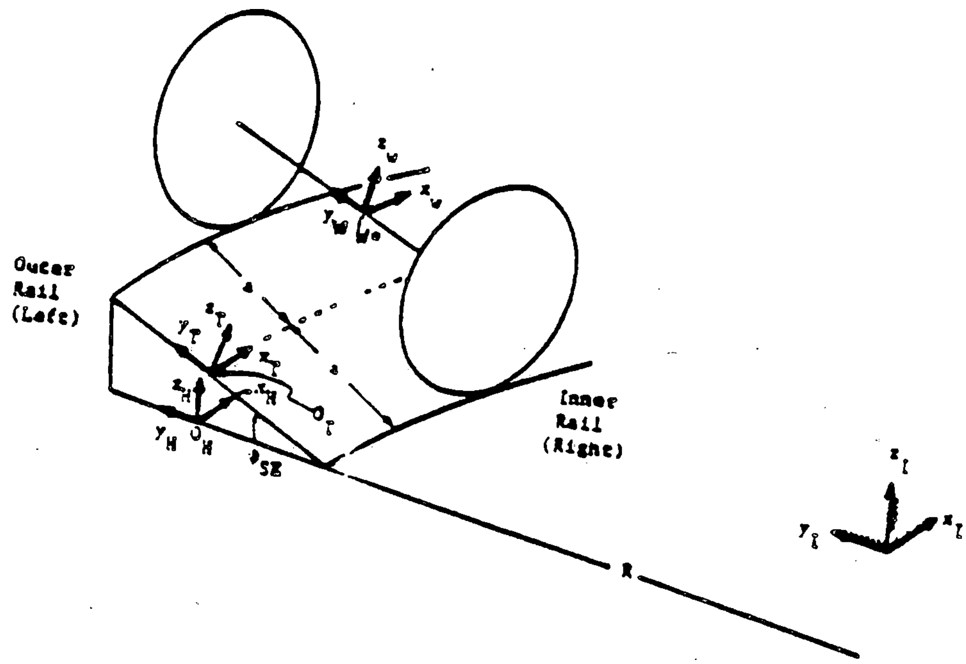

Figure A.2   Coordinate systems of wheelset and track.

Since the longitudinal axes of the D and P systems are aligned, one may write directly,

$$
{}^{D}\vec{\omega}^{P} = \begin{pmatrix} \dot{\phi}_{CR} \\ 0 \\ 0 \end{pmatrix}_{\{D\}}
$$

The angular velocity and acceleration of the P frame are then given as follows:

$$
{}^{I}\vec{\omega}^{P} = \begin{pmatrix} \mathring{\phi}_{TR} \\ 0 \\ -V\rho \end{pmatrix}_{\{D\}} = \begin{pmatrix} \mathring{\phi}_{TR} \\ 0 \\ -V\rho \end{pmatrix}_{\{P\}} \tag{A.2.2}
$$

$$
{}^{I}\dot{\vec{\omega}}^{P} = \begin{pmatrix} \check{\phi}_{TR} \\ -\phi_{SE}V\dot{\rho} \\ -V\dot{\rho} \end{pmatrix}_{\{D\}} = \begin{pmatrix} \check{\phi}_{TR} \\ -\phi_{TR}V\dot{\rho} \\ -V\dot{\rho} \end{pmatrix}_{\{P\}}
$$

A.2.2 Translation of the Origin of the Track Frames

The translational velocity and acceleration of the origin of the two track frames are basic quantities used in many other expressions. Relations (A.1.1) and (A.1.4) are applied as appropriate for successive frames of reference, with the following results.

$$\frac{d}{dt}\left({}^{I}\vec{R}^{D}\right) = \begin{pmatrix} V \\ 0 \\ a\dot{\phi}_{SE} \end{pmatrix}_{\{D\}} \qquad \frac{d^2}{dt^2}\left({}^{I}\vec{R}^{D}\right) = \begin{pmatrix} aV\dot{\rho} \\ -V^2\rho \\ \phi_{SE}V^2\rho + a\ddot{\phi}_{SE} \end{pmatrix}_{\{D\}} \tag{A.2.3}$$

$$\frac{d}{dt}\left({}^{I}\vec{R}^{P}\right) = \begin{pmatrix} V \\ 0 \\ a\dot{\phi}_{SE} \end{pmatrix}_{\{P\}} \qquad \frac{d^2}{dt^2}\left({}^{I}\vec{R}^{P}\right) = \begin{pmatrix} aV\dot{\rho} \\ -V^2\rho \\ \phi_{TR}V^2\rho + a\ddot{\phi}_{SE} \end{pmatrix}_{\{P\}}$$

A.2.3 Translation Relative to the Deterministic Track Frame

The translational motion of the carbody, expressed in the coordinates of the deterministic track frame, may be considered with relations (A.1.1) and (A.1.4) and the following values for a body with center of mass at point Q,

$$ {}^{I}\vec{R}^{D} \qquad {}^{I}\vec{\omega}^{D} = \begin{pmatrix} \dot{\phi}_{SE} \\ -\phi_{SE}V\rho \\ -(1-\frac{1}{2}{\phi_{SE}}^2)V\rho \end{pmatrix}_{\{D\}}$$

$$ {}^{D}\vec{R}^{Q} = \begin{pmatrix} x \\ y \\ z \end{pmatrix}_{\{D\}} \qquad \vec{v}_{rel} = \begin{pmatrix} \dot{x} \\ \dot{y} \\ \dot{z} \end{pmatrix}_{\{D\}} \qquad \vec{a}_{rel} = \begin{pmatrix} \ddot{x} \\ \ddot{y} \\ \ddot{z} \end{pmatrix}_{\{D\}}$$

The velocity and acceleration of a point Q in the D frame is determined with (A.1.1) and (A.1.4), as follows:

$$\boxed{\begin{array}{l} \dfrac{d}{dt}\left({}^{I}\vec{R}^{Q}\right) = \begin{pmatrix} \dot{x} + V + yV\rho \\ \dot{y} - xV\rho - z\dot{\phi}_{SE} \\ \dot{z} + (a+y)\dot{\phi}_{SE} + x\phi_{SE}V\rho \end{pmatrix}_{\{D\}} \qquad \text{(A.2.4)} \\ \dfrac{d^2}{dt^2}\left({}^{I}\vec{R}^{Q}\right) = \begin{pmatrix} \ddot{x} + (a+y)V\dot{\rho} - x\rho V^2\rho \\ \ddot{y} - V^2\rho - z\ddot{\phi}_{SE} - xV\dot{\rho} \\ \ddot{z} + \phi_{SE}V^2\rho + (a+y)\ddot{\phi}_{SE} + x\phi_{SE}V\dot{\rho} \end{pmatrix}_{\{D\}} \end{array}}$$

A.2.4 Translation Relative to the Track Plane

The frame of reference of the track plane is used to describe the motion of the wheelsets. The derivation of translational motion relative to the P frame is similar to that with respect to the D frame, except that the track roll due to crosslevel must be included.

The motion of a point Q at the center of mass of a body which is described in P system coordinates may be written using relations (A.1.1) and (A.1.4) with the following values:

$${}^{I}\vec{R}^{P} \qquad {}^{I}\vec{\omega}^{P} = \begin{pmatrix} \dot{\phi}_{TR} \\ -\phi_{TR}V\rho \\ -(1 - \frac{1}{2}{\phi_{TR}}^2)V\rho \end{pmatrix}_{\{P\}}$$

$${}^{P}\vec{R}^{Q} = \begin{pmatrix} x \\ y \\ z \end{pmatrix}_{\{P\}} \qquad \vec{v}_{rel} = \begin{pmatrix} \dot{x} \\ \dot{y} \\ \dot{z} \end{pmatrix}_{\{P\}} \qquad \vec{a}_{rel} = \begin{pmatrix} \ddot{x} \\ \ddot{y} \\ \ddot{z} \end{pmatrix}_{\{P\}}$$

Note that the transformation between D and P frames may be used to transform to D coordinates a point expressed in the P system:

$${}^{I}\vec{R}^{P} = \begin{pmatrix} x \\ y \\ z \end{pmatrix}_{\{P\}} = \begin{pmatrix} x \\ y(1 - \frac{1}{2}{\phi_{CR}}^2) - z\phi_{CR} \\ y\phi_{CR} + z(1 - \frac{1}{2}{\phi_{CR}}^2) \end{pmatrix}_{\{D\}}$$

The velocity and acceleration are then:

$$
\frac{d}{dt}\left({}^{I}\vec{R}^{Q}\right) = \begin{pmatrix} \dot{x} + V + yV\rho \\ \dot{y} - xV\rho - z\dot{\phi}_{TR} \\ \dot{z} + a\dot{\phi}_{SE} + y\dot{\phi}_{TR} \end{pmatrix}_{\{P\}} \tag{A.2.5}
$$

$$
\frac{d^2}{dt^2}\left({}^{I}\vec{R}^{Q}\right) = \begin{pmatrix} \check{x} + (a+y)V\dot{\rho} \\ \check{y} - V^2\rho - z\check{\phi}_{TR} - xV\dot{\rho} \\ \check{z} + \phi_{TR}V^2\rho + a\check{\phi}_{SE} + y\check{\phi}_{TR} \end{pmatrix}_{\{P\}}
$$

A.2.5 Rigid Body Rotations

Each rigid body in the model has some rotational freedom relative to its corresponding track system. The most general case of yaw, roll, and pitch freedom will be considered here.

Three rotations are required to describe the angular position of a body with respect to a track system T. First, an intermediate frame 1 is defined by a yaw motion ψ relative to the T frame. The body frame 2 is defined by a roll displacement with respect to the intermediate frame 1 by the angle ϕ. Finally, the body frame F is given by a pitch displacement θ.

Combining these rotations defines the transformation from the track frame T to the body frame F. To second order, it is given as follows:

$$
\vec{u}_{\{F\}} = \begin{pmatrix} 1 - \frac{1}{2}(\theta^2 + \psi^2) & \psi & -\theta \\ -\psi & 1 - \frac{1}{2}(\phi^2 + \psi^2) & \phi \\ \theta + \phi\psi & -\phi + \theta\psi & 1 - \frac{1}{2}(\phi^2 + \theta^2) \end{pmatrix} \vec{u}_{\{T\}}
$$

To first order, the forward and inverse transformations are given by:

$$\vec{u}_{\{F\}} = \begin{pmatrix} 1 & \psi & -\theta \\ -\psi & 1 & \phi \\ \theta & -\phi & 1 \end{pmatrix} \vec{u}_{\{T\}} \qquad \vec{u}_{\{T\}} = \begin{pmatrix} 1 & -\psi & \theta \\ \psi & 1 & -\phi \\ -\theta & \phi & 1 \end{pmatrix} \vec{u}_{\{F\}} \quad \text{(A.2.6)}$$

The angular velocity of the F frame with respect to the T frame may be written as

$$^{T}\vec{\omega}^{F} = \dot{\psi}\hat{k}_1 + \dot{\phi}\hat{\imath}_2 + \dot{\theta}\hat{\jmath}_F$$

The angular velocity of the T frame relative to inertial space may be simply expressed in the T frame coordinates, using either (A.2.1) or (A.2.2) as appropriate.

$$^{I}\vec{\omega}^{T} = \begin{pmatrix} \omega_{TX} \\ \omega_{TY} \\ \omega_{TZ} \end{pmatrix}_{\{T\}}$$

Transforming this vector to the F frame, and adding the angular velocity of the F frame relative to the T frame, one arrives at the angular velocity of the F system relative to inertial space. Preserving angular terms of second order in the resulting expressions,

$$\begin{aligned}
\omega_{FX} &= (1 - \frac{1}{2}(\psi^2 + \theta^2))\omega_{TX} + \dot{\phi}(1 - \frac{1}{2}\theta^2) + \psi\omega_{TY} - \theta(\omega_{TZ} + \dot{\psi}) \\
\omega_{FY} &= -\psi\omega_{TX} + (1 - \frac{1}{2}(\psi^2 + \phi^2))\omega_{TY} + \phi(\omega_{TZ} + \dot{\psi}) + \dot{\theta} \\
\omega_{FZ} &= \theta(\omega_{TX} + \dot{\phi}) - \phi\omega_{TY} + (1 - \frac{1}{2}(\theta^2 + \phi^2))(\omega_{TZ} + \dot{\psi})
\end{aligned}$$

Applying the small angle approximation,

$$
{}^{I}\vec{\omega}^{F} = \begin{pmatrix} \omega_{FX} \\ \omega_{FY} \\ \omega_{FZ} \end{pmatrix}_{\{F\}} = \begin{pmatrix} \dot{\phi} + \omega_{TX} \\ \dot{\theta} + \omega_{TY} \\ \dot{\psi} + \omega_{TZ} \end{pmatrix}_{\{F\}} . \tag{A.2.7}
$$

The second order relations may be differentiated, neglecting terms consisting of the product of a small angle and a small angular velocity, as well as two small angular velocities. The terms $\dot{\theta}\omega_{FZ}$ and $\dot{\theta}\omega_{FX}$ are eliminated from the roll and yaw relations, respectively, since they will be the product of small angular rates for the carbody. In the case of the wheelsets, these relations will be applied to the 2 frame, not W, for which θ is identically zero.

$$
{}^{I}\dot{\vec{\omega}}^{F} = \begin{pmatrix} \dot{\omega}_{FX} \\ \dot{\omega}_{FY} \\ \dot{\omega}_{FZ} \end{pmatrix}_{\{F\}} \tag{A.2.8}
$$

where:

$$
\begin{aligned}
\dot{\omega}_{FX} &= \check{\phi} + \dot{\omega}_{TX} - \theta(\check{\psi} + \dot{\omega}_{TZ}) \\
\dot{\omega}_{FY} &= \check{\theta} + \dot{\omega}_{TY} - \psi\dot{\omega}_{TX} + \phi(\check{\psi} + \dot{\omega}_{TZ}) \\
\dot{\omega}_{FZ} &= \check{\psi} + \dot{\omega}_{TZ} + \theta(\check{\phi} + \dot{\omega}_{TX})
\end{aligned}
$$

Equations (A.1.2) and (A.1.3), applied to the time rate of change of rotational momentum in a reference frame F, may both be expressed in a general form, with the cross terms χ suitably defined:

$$
\vec{\tau} = \begin{pmatrix} I_X\dot{\omega}_{FX} \\ I_Y\dot{\omega}_{FY} \\ I_Z\dot{\omega}_{FZ} \end{pmatrix}_{\{F\}} + \begin{pmatrix} \chi_X \\ \chi_Y \\ \chi_Z \end{pmatrix}_{\{F\}}
$$

One now seeks expressions for the accelerations $\breve{\psi}$, $\breve{\phi}$, and $\breve{\theta}$. Defining some terms Γ, without writing their detailed components, one may rewrite the above relations as follows:

$$\tau_X = I_X(\breve{\phi} - \theta\breve{\psi} + \Gamma_X) + \chi_X$$
$$\tau_Y = I_Y(\breve{\theta} + \phi\breve{\psi} + \Gamma_Y) + \chi_Y$$
$$\tau_Z = I_Z(\breve{\psi} + \theta\breve{\phi} + \Gamma_Z) + \chi_Z$$

These expressions may be reduced in order to uncouple the angular accelerations from each other. Solving for each of the individual angular accelerations and neglecting small terms, with the cross terms χ from (A.1.2) or (A.1.3) as appropriate,

$$\breve{\phi} = \frac{1}{I_X}(\tau_X - \chi_X) + \theta\frac{1}{I_Z}\tau_Z - \dot{\omega}_{TX} \tag{A.2.9}$$

$$\breve{\theta} = \frac{1}{I_Y}(\tau_Y - \chi_Y) - \phi\frac{1}{I_Z}\tau_Z - \dot{\omega}_{TY} + \psi\dot{\omega}_{TX}$$

$$\breve{\psi} = \frac{1}{I_Z}(\tau_Z - \chi_Z) - \theta\frac{1}{I_X}\tau_X - \dot{\omega}_{TZ}$$

A.3 Transformations Between Coordinate Systems

The motions of the rigid bodies may be neatly described by coordinate systems located at the longitudinal positions of the body centers of mass. Interactions between these bodies occur at suspension elements which act between two bodies, each "end" of which may be considered to be at fixed positions relative to the two centers of mass of the bodies to which it is attached. Since these body centers are generally described in different D coordinate systems, a derivation of the suspension strokes requires methods to transform between D systems located at different positions along the track. Both translational and rotational differences between frames must be reconciled.

A.3.1 Translational Differences Between Frames

Consider two points Q and Q' which have positions and velocities given in coordinate systems D and D', respectively. The position and velocity of Q' may be expressed in D system coordinates by transforming from D' to S', then to H', onwards to H, then to S, and finally to D. (Recall that these frames have been previously defined.) These steps will be written out below.

First, write the positions of Q and Q' in the D and D' frames.

$$ {}^{D}\vec{R}^{Q} = \begin{pmatrix} x \\ y \\ z \end{pmatrix}_{\{D\}} \qquad {}^{D'}\vec{R}^{Q'} = \begin{pmatrix} x' \\ y' \\ z' \end{pmatrix}_{\{D'\}} $$

The frame S' has the same orientation as D' and is merely shifted laterally by the track half-gauge. Then a rotation through the local superelevation angle yields the position of Q' in coordinates of the horizontal frame H'. Thus,

$$ {}^{H'}\vec{R}^{Q'} = \begin{pmatrix} x' \\ a + y' - z'\phi_{SE}' \\ z' + (a+y')\phi_{SE}' \end{pmatrix}_{\{H'\}} $$

Considering the transformation from the H system to the H' system, both a rotation and a translation are required. The H and H' frames have a different orientation since the x axis of each frame is directed along the track centerline. The magnitude of the angle of rotation about the $\hat{k}_{\{H\}}$ axis is approximately given by the longitudinal distance times the average curvature. The sign of the rotation is negative for the case of H' forward of H and positive if H' is aft of H. (This is consistent with the convention that positive curve radii indicate curving to the right.) If the longitudinal distance between the two D frames is given by l, and the curvature averaged at the two locations is $\rho_{AVG} = (\rho)_{AVG}$, then

$$\vec{u}_{\{H'\}} = \begin{pmatrix} 1 & \gamma & 0 \\ -\gamma & 1 & 0 \\ 0 & 0 & 1 \end{pmatrix} \vec{u}_{\{H\}} \qquad \vec{u}_{\{H\}} = \begin{pmatrix} 1 & -\gamma & 0 \\ \gamma & 1 & 0 \\ 0 & 0 & 1 \end{pmatrix} \vec{u}_{\{H'\}}$$

where:

$$\gamma = -l\,\rho_{AVG}$$

$$l = \begin{cases} \text{positive if } H' \text{ forward of } H \\ \text{negative if } H' \text{ aft of } H \end{cases}$$

Observe that H' is always displaced laterally in a negative sense from H since the track is curving to the right. The magnitude of this lateral shift is given approximately by $l^2\,\rho_{AVG}/2$.

Finally, note that the vertical position of the right rail does not vary due to track superelevation. Then the position of Q' relative to H, expressed in H coordinates, may be written by adding two vectors when both are expressed in the coordinates of the H system:

$${}^{H}\vec{R}^{Q'} = {}^{H}\vec{R}^{H'} + {}^{H'}\vec{R}^{Q'}$$

$$= \begin{pmatrix} l + x' - y'\gamma \\ -\frac{l^2}{2}\rho_{AVG} + a + y' - z'\phi_{SE}' + x'\gamma \\ (a + y')\phi_{SE}' + z' \end{pmatrix}_{\{H\}}$$

This expression must be transformed to the coordinates of the superelevated track system S, followed by a lateral translation equal to the track half-gauge. The resulting vector from D to Q' is then expressed in D system coordinates. Subtracting these components from the position of Q relative to the D frame yields the difference of position, written in D coordinates:

$$
{}^{D}\vec{R}^{Q} - {}^{D}\vec{R}^{Q'} = \begin{pmatrix} x - l - x' + y'\gamma \\ y + \frac{l^2}{2}\rho_{AVG} - y' - z'(\phi_{SE} - \phi_{SE}') - x'\gamma \\ z + (a + y')(\phi_{SE} - \phi_{SE}') - z' - \phi_{SE}\frac{l^2}{2}\rho_{AVG} \end{pmatrix}_{\{D\}} \quad \text{(A.3.1)}
$$

Consider now the difference between the inertial velocities and accelerations of points Q' and Q. Previous formulae provide the value of the inertial velocity and acceleration of a point expressed in the coordinates of its local D frame. The difference between the values for two points is obtained simply by transforming the value for Q' to D coordinates and subtracting the result from the value for the point Q.

The inertial velocities and accelerations of the two points may be written as follows:

$$
\frac{d}{dt}\left({}^{I}\vec{R}^{Q}\right) = \begin{pmatrix} v_X \\ v_Y \\ v_Z \end{pmatrix}_{\{D\}} \qquad \frac{d}{dt}\left({}^{I}\vec{R}^{Q'}\right) = \begin{pmatrix} v'_X \\ v'_Y \\ v'_Z \end{pmatrix}_{\{D'\}}
$$

$$
\frac{d^2}{dt^2}\left({}^{I}\vec{R}^{Q}\right) = \begin{pmatrix} a_X \\ a_Y \\ a_Z \end{pmatrix}_{\{D\}} \qquad \frac{d^2}{dt^2}\left({}^{I}\vec{R}^{Q'}\right) = \begin{pmatrix} a'_X \\ a'_Y \\ a'_Z \end{pmatrix}_{\{D'\}}
$$

The orientations of the D and D' frames are identical to those of the S and S' frames, respectively. The rotation between the D and D' coordinate systems, to first order, is given as follows:

$$
\vec{u}_{\{D\}} = \begin{pmatrix} 1 & -\gamma & 0 \\ \gamma & 1 & (\phi_{SE} - \phi_{SE}') \\ 0 & -(\phi_{SE} - \phi_{SE}') & 1 \end{pmatrix} \vec{u}_{\{D'\}}
$$

Transforming the velocity and acceleration of Q' to the D system and subtracting the result from that of Q yields the following:

$$\frac{d}{dt}\left({}^{I}\vec{R}^{Q}\right) - \frac{d}{dt}\left({}^{I}\vec{R}^{Q'}\right) = \begin{pmatrix} v_X - v'_X + \gamma v'_Y \\ v_Y - v'_Y - \gamma v'_X - (\phi_{SE} - \phi_{SE}{}')v'_Z \\ v_Z - v'_Z + (\phi_{SE} - \phi_{SE}{}')v'_Y \end{pmatrix}_{\{D\}} \quad \text{(A.3.2)}$$

$$\frac{d^2}{dt^2}\left({}^{I}\vec{R}^{Q}\right) - \frac{d^2}{dt^2}\left({}^{I}\vec{R}^{Q'}\right) = \begin{pmatrix} a_X - a'_X + \gamma a'_Y \\ a_Y - a'_Y - \gamma a'_X - (\phi_{SE} - \phi_{SE}{}')a'_Z \\ a_Z - a'_Z + (\phi_{SE} - \phi_{SE}{}')a'_Y \end{pmatrix}_{\{D\}}$$

A.3.2 Rotational Differences Between Frames

The orientation of the principal axes of each rigid body may be represented by roll, pitch, and yaw rotations relative to the appropriate D system for each body, as indicated in (A.2.6). Consider two bodies, F and F', which are oriented with respect to the frames D and D' with the following transformation matrices:

$$\vec{u}_{\{F\}} = \begin{pmatrix} 1 & \psi & -\theta \\ -\psi & 1 & \phi \\ \theta & -\phi & 1 \end{pmatrix} \vec{u}_{\{D\}} \qquad \vec{u}_{\{F'\}} = \begin{pmatrix} 1 & \psi' & -\theta' \\ -\psi' & 1 & \phi' \\ \theta' & -\phi' & 1 \end{pmatrix} \vec{u}_{\{D'\}}$$

These matrices and that which describes the orientation of D' with respect to D may be manipulated to arrive at the transformation from the F' to the F orientation:

$$\vec{u}_{\{F\}} = \begin{pmatrix} 1 & (\psi - \psi' - \gamma) & -(\theta - \theta') \\ -(\psi - \psi' - \gamma) & 1 & (\phi_F - \phi'_F) \\ (\theta - \theta') & -(\phi_F - \phi'_F) & 1 \end{pmatrix} \vec{u}_{\{F'\}} \quad \text{(A.3.3)}$$

where:

$$\phi_F = \phi_{SE} + \phi$$
$$\phi'_F = \phi_{SE}{}' + \phi'$$

The above result indicates that the frame F is obtained from the F' frame by rolling through an angle equal to $(\phi_F - \phi'_F)$, by pitching through an angle $(\theta - \theta')$, and by rotating in the yaw sense through an angle $(\psi - \psi' - \gamma)$.

Finally, the difference between angular rates of rotation of the principal axes of two rigid body systems is found in a manner analogous to the difference in the translational velocities. The differences in the time rate of change of angular velocity may be obtained in the same fashion. The angular velocities and accelerations may be written as follows:

$$
{}^I\vec{\omega}^F = \begin{pmatrix} \omega_X \\ \omega_Y \\ \omega_Z \end{pmatrix}_{\{D\}} \qquad {}^I\vec{\omega}^{F'} = \begin{pmatrix} \omega'_X \\ \omega'_Y \\ \omega'_Z \end{pmatrix}_{\{D'\}}
$$

$$
{}^I\dot{\vec{\omega}}^F = \begin{pmatrix} \dot{\omega}_X \\ \dot{\omega}_Y \\ \dot{\omega}_Z \end{pmatrix}_{\{D\}} \qquad {}^I\dot{\vec{\omega}}^{F'} = \begin{pmatrix} \dot{\omega}'_X \\ \dot{\omega}'_Y \\ \dot{\omega}'_Z \end{pmatrix}_{\{D'\}}
$$

Applying the transformation from the D' frame to the D system in order to find the differences in the angular velocity and acceleration between the two frames,

$$
\boxed{
\begin{aligned}
{}^I\vec{\omega}^F - {}^I\vec{\omega}^{F'} &= \begin{pmatrix} \omega_X - \omega'_X + \gamma\omega'_Y \\ \omega_Y - \omega'_Y - \gamma\omega'_X - (\phi_{SE} - \phi_{SE}')\omega'_Z \\ \omega_Z - \omega'_Z + (\phi_{SE} - \phi_{SE}')\omega'_Y \end{pmatrix}_{\{D\}} \qquad \text{(A.3.4)} \\
{}^I\dot{\vec{\omega}}^F - {}^I\dot{\vec{\omega}}^{F'} &= \begin{pmatrix} \dot{\omega}_X - \dot{\omega}'_X + \gamma\dot{\omega}'_Y \\ \dot{\omega}_Y - \dot{\omega}'_Y - \gamma\dot{\omega}'_X - (\phi_{SE} - \phi_{SE}')\dot{\omega}'_Z \\ \dot{\omega}_Z - \dot{\omega}'_Z + (\phi_{SE} - \phi_{SE}')\dot{\omega}'_Y \end{pmatrix}_{\{D\}}
\end{aligned}
}
$$

Appendix B

Wheel / Rail Mechanics

In this appendix, the dynamic interactions between wheel and rail are considered. Based on the kinematics presented in Appendix A, wheelset translational and rotational equations are found. These relations are then extended to include translation of points defined relative to the wheelset frame of reference.

The frictional contact patch forces are calculated using Kalker's method, and the wheel/rail forces are resolved in both the wheelset and track frames of reference. With the applied forces given from wheel/rail considerations, and kinematic and geometric relations found in this appendix, the equations of motion of a wheelset are found for the general case of two points of contact between a single wheel and the rail.

B.1 The Wheelset System

The wheelset model includes the wheelset motion which is permitted, which involve lateral, yaw, and spin movement. The wheelset roll and vertical position of the center of gravity are determined by the constraint of wheel/rail contact. The wheelset rolls and is displaced vertically relative to the track plane as a result of the differences in left and right rolling radii and the heights of the contact patches. The wheelset vertical and roll equations of motion are used to solve for the wheelset normal loads; these relations are important even though the wheelset motion is constrained in these modes.

Originating at the track centerline in the P frame, one displacement and three rotations are required to describe the motion of the wheelset. The position of the center of mass is determined with respect to the perturbed track frame P, and it is given by the following,

$$^{P}\vec{R}^{W} = \begin{pmatrix} 0 \\ y_W \\ z_W \end{pmatrix}_{\{P\}} = \begin{pmatrix} 0 \\ y_W - z_W\phi_{CR} \\ z_W \end{pmatrix}_{\{D\}} .$$

where:

$$y_W = \text{wheelset lateral position}$$
$$z_W = r_o + z_{WR} + z_{SURF} = \text{wheelset vertical position}$$
$$r_o = \text{nominal wheelset rolling radius}$$
$$z_{WR} = \text{vertical height of wheel w.r.t. rail}$$
$$z_{SURF} = \text{track vertical surface perturbation}$$

The z_{WR} term is obtained from wheel/rail geometry tables, for it is the vertical position of the wheelset centroid as a function of lateral excursion. The surface perturbation, z_{SURF}, is the vertical track roughness perturbation.

B.1.1 Rotation of the Wheelset

A principal axis coordinate system for the wheelset is obtained by rotating through the yaw angle ψ_W and rolling through an angle ϕ_W. This is defined to be the 2 coordinate system for the wheelset, following the discussion of section A.2.5. (Note that the wheelset pitch is considered to be a "half-state" since only its first derivative, the wheelset spin, is involved in the model.) To first order, the transformation matrix from the track plane P to the 2 system is written using (A.2.6) with no pitch angle:

$$\vec{u}_{\{2\}} = \begin{pmatrix} 1 & \psi_W & 0 \\ -\psi_W & 1 & \phi_W \\ 0 & -\phi_W & 1 \end{pmatrix} \vec{u}_{\{P\}}$$

Using the roll transformation from the D to the P frame,

$$\vec{u}_{\{2\}} = \begin{pmatrix} 1 & \psi_W & 0 \\ -\psi_W & 1 & (\phi_{CR} + \phi_W) \\ 0 & -(\phi_{CR} + \phi_W) & 1 \end{pmatrix} \vec{u}_{\{D\}}$$

The angular velocity of the 2 frame is developed using (A.2.7), with no spin term $\dot{\theta}$, as well as the relations for the P frame angular velocity from (A.2.2), expressed in the P coordinate frame. The wheelset system W is axially aligned with the 2 frame but is spinning with the wheel.

$$\boxed{{}^{I}\vec{\omega}^{2} = \begin{pmatrix} \dot{\phi}_W + \dot{\phi}_{TR} \\ 0 \\ \dot{\psi}_W - V\rho \end{pmatrix}_{\{2\}} \qquad {}^{I}\vec{\omega}^{W} = \begin{pmatrix} \dot{\phi}_W + \dot{\phi}_{TR} \\ \dot{\theta}_W \\ \dot{\psi}_W - V\rho \end{pmatrix}_{\{2\}} \qquad \text{(B.1.1)}}$$

The angular acceleration may be written for the W frame, in the 2 coordinate system with $\theta = 0$, using (A.2.8):

$${}^{I}\dot{\vec{\omega}}^{W} = \begin{pmatrix} \dot{\omega}_{WX} \\ \dot{\omega}_{WY} \\ \dot{\omega}_{WZ} \end{pmatrix}_{\{2\}} \qquad \text{(B.1.2)}$$

where:

$$\dot{\omega}_{WX} = \breve{\phi}_W + \breve{\phi}_{TR}$$
$$\dot{\omega}_{WY} = \breve{\theta}_W - \phi_{TR} V \dot{\rho} - \psi_W \breve{\phi}_{TR} + \phi_W(\breve{\psi}_W - V\dot{\rho})$$
$$\dot{\omega}_{WZ} = \breve{\psi}_W - V\dot{\rho}$$

The 2 system must be always axially aligned with the W frame, but it is not subjected to the spin accelerations $\breve{\theta}_W$. One may then write:

$$
{}^{I}\dot{\vec{\omega}}^{2} = \begin{pmatrix} \dot{\omega}_{WX} \\ \dot{\omega}_{WY} - \breve{\theta}_W \\ \dot{\omega}_{WZ} \end{pmatrix}_{\{2\}} \tag{B.1.3}
$$

The rotational equations for the wheelset are now found using the general solution (A.1.2) with (A.2.9), noting that due to symmetry $I_{WX} = I_{WZ}$,

$$
\begin{aligned}
\breve{\phi}_W &= \frac{1}{I_{WX}}(\tau_{WX} + I_{WY}\dot{\theta}_W\omega_{WZ}) - \breve{\phi}_{TR} \\
\breve{\theta}_W &= \frac{1}{I_{WY}}\tau_{WY} - \phi_W\frac{1}{I_{WZ}}\tau_{WZ} + \phi_{TR}V\dot{\rho} + \psi_W\breve{\phi}_{TR} \\
\breve{\psi}_W &= \frac{1}{I_{WZ}}(\tau_{WZ} - I_{WY}\dot{\theta}_W\omega_{WX}) + V\dot{\rho}
\end{aligned} \tag{B.1.4}
$$

B.1.2 Translation of the Wheelset

Separate P frame systems are constructed beneath each wheelset. With the approximations previously noted, the position vector and relative motion are found below.

$$
{}^{P}\vec{R}^{W} = \begin{pmatrix} 0 \\ y_W \\ z_W \end{pmatrix}_{\{P\}} \qquad \vec{v}_{rel} = \begin{pmatrix} 0 \\ \dot{y}_W \\ \dot{z}_W \end{pmatrix}_{\{P\}} \qquad \vec{a}_{rel} = \begin{pmatrix} 0 \\ \breve{y}_W \\ \breve{z}_W \end{pmatrix}_{\{P\}}
$$

Note that the first and second derivatives $\dot{z}_W$ and $\breve{z}_W$ are obtained from kinematic considerations involving wheel/rail contact.

Defining the velocity and acceleration of the wheelset, measured in the P system, the following is found using (A.2.5) (neglecting small terms):

$$\frac{d}{dt}\left({}^{I}\vec{R}^{W}\right) = \begin{pmatrix} V \\ \dot{y}_W - z_W\dot{\phi}_{TR} \\ \dot{z}_W + a\dot{\phi}_{SE} \end{pmatrix}_{\{P\}} \tag{B.1.5}$$

$$\frac{d^2}{dt^2}\left({}^{I}\vec{R}^{W}\right) = \begin{pmatrix} aV\dot{\rho} \\ \breve{y}_W - V^2\rho - z_W\breve{\phi}_{TR} \\ \breve{z}_W + \phi_{TR}V^2\rho + a\breve{\phi}_{SE} + y_W\breve{\phi}_{TR} \end{pmatrix}_{\{P\}} = \frac{1}{m_W}\begin{pmatrix} F_{WX} \\ F_{WY} \\ F_{WZ} \end{pmatrix}_{\{P\}}$$

B.1.3 Displacement Relative to the Wheelset System

The positions of points fixed with respect to the 2 system are used in the consideration of both wheel/rail and suspension forces. The motion of points fixed relative to both the wheelset system and the 2 system (which does not spin with the wheelset) may be found and expressed in coordinates of both the D and P frames of reference. (Three of these four cases will be encountered in the discussions of wheel/rail interaction and primary suspension forces.) Note that the origins of the W and 2 frames coincide. Consider a point with position expressed in coordinates of the 2 system, and with no motion relative to the F system, where the F system may be either the W or 2 system:

$$^{W}\vec{R}^{Q} = \begin{pmatrix} x \\ y \\ z \end{pmatrix}_{\{2\}} \quad \vec{v}_{rel} = \begin{pmatrix} 0 \\ 0 \\ 0 \end{pmatrix}_{\{F\}} \quad \vec{a}_{rel} = \begin{pmatrix} 0 \\ 0 \\ 0 \end{pmatrix}_{\{F\}}$$

Since the position of a point fixed relative to the 2 system is needed, upon transforming to the P and D systems the following results are obtained:

$$^{D}\vec{R}^{Q} = {}^{D}\vec{R}^{2} + {}^{2}\vec{R}^{Q}$$

$$
{}^{D}\vec{R}^{Q} = \begin{pmatrix} x - y\psi_W \\ y_W + x\psi_W + y - z\phi_W \\ z_W + y\phi_W + z \end{pmatrix}_{\{P\}}
= \begin{pmatrix} x - y\psi_W \\ y_W - z_W\phi_{CR} + x\psi_W + y - z(\phi_{CR} + \phi_W) \\ z_W + y(\phi_{CR} + \phi_W) + z \end{pmatrix}_{\{D\}} \qquad \text{(B.1.6)}
$$

The motion of points relative to the W and 2 systems may be considered in a general sense using equations (A.1.1) and (B.1.5), where the spin angular velocity may be either that for the wheelset W system or the 2 system. The F system is used to represent either of these cases. Note that ω_{FX} and ω_{FZ} are small angular rates, whereas ω_{FY} is not a small angular rate when the frame F is the wheelset frame W. Applying the small angle approximation,

$$
\frac{d}{dt}\left({}^{I}\vec{R}^{Q}\right) = \frac{d}{dt}\left({}^{I}\vec{R}^{W}\right) + {}^{I}\vec{\omega}^{F} \times {}^{F}\vec{R}^{Q} \qquad \text{(B.1.7)}
$$

$$
= \begin{pmatrix} V + v_X \\ \dot{y}_W - z_W\dot{\phi}_{TR} + v_Y + z\psi_W\omega_{FY} + x\phi_W\omega_{FY} \\ \dot{z}_W + a\dot{\phi}_{SE} + v_Z \end{pmatrix}_{\{P\}}
$$

$$
= \begin{pmatrix} V + v_X \\ \dot{y}_W - z_W\dot{\phi}_{TR} - \phi_{CR}\dot{z}_W + v_Y + z\psi_W\omega_{FY} + x(\phi_{CR} + \phi_W)\omega_{FY} \\ \dot{z}_W + a\dot{\phi}_{SE} + \phi_{CR}\dot{y}_W + v_Z \end{pmatrix}_{\{D\}}
$$

where:

$$v_X = z\omega_{FY} - y\omega_{FZ}$$

$$v_Y = x\omega_{FZ} - z\omega_{FX}$$

$$v_Z = y\omega_{FX} - x\omega_{FY}$$

B.2 Wheel / Rail Contact

The forces developed at the wheel/rail contact patches have a significant effect on the dynamic performance of a rail vehicle. The total force at a contact patch is the sum of the normal force, which acts perpendicular to the plane of contact, and the frictional creep force, which acts in the plane of contact.

Consideration of the relative motion between wheel and rail at the points of contact yields the wheel/rail creepage, which is a measure of the amount of relative slip between the two bodies. The frictional creep forces at the interface are determined by the creepages and the wheel/rail contact geometry.

B.2.1 Location of the Contact Patches

The point of contact between wheel and rail may be described with respect to the wheelset center of gravity using 2 system coordinates. The lateral and vertical positions arise from consideration of the half-gauge of the track and the wheel rolling radius, respectively. The longitudinal component results from a shift in the contact patch location as the wheelset yaws. For a positive yaw angle, this shift is in the forward direction at the left wheel, relative to the 2 system, and in the negative direction at the right wheel [16]. The contact patch locations may be written as follows:

$$ {}^{W}\vec{R}^{CPL} = \begin{pmatrix} \Delta_L \\ a \\ -r_L \end{pmatrix}_{\{2\}} \qquad {}^{W}\vec{R}^{CPR} = \begin{pmatrix} -\Delta_R \\ -a \\ -r_R \end{pmatrix}_{\{2\}} \tag{B.2.1} $$

where:

$$ \Delta_L = r_L \psi_W \tan(\gamma_L) $$
$$ \Delta_R = r_R \psi_W \tan(\gamma_R) $$

It is convenient at this point to write down the relations for accessing the wheel/rail contact geometry tables. The contact parameters are provided as a function of wheelset lateral excursion relative to the rail. It is approximately correct to assume that the contact geometry for each wheel is independent of the other wheel, and thus one may take the net lateral excursion of each wheel separately and perform two table lookups. This approach permits implied gauge changes due to rail flexibility, and it can also be used to handle models with large gauge variations. In the following, y_{LR} and y_{RR} are the lateral displacement of the left and right rails, respectively, due to rail and track flexibility.

$$\begin{aligned} y_{net,L} &= y_W - y_{PER,L} - y_{LR} \\ y_{net,R} &= y_W - y_{PER,R} - y_{RR} \end{aligned} \tag{B.2.2}$$

B.2.2 Transformation of Wheel / Rail Relative Velocity

In order to consider the wheel/rail contact constraint and the wheel/rail creepages, it is necessary to first transform the differences between the velocities of wheel and rail to contact patch coordinates.

The contact patch plane at each wheel is defined by a roll transformation about the rail surface. The angle involved in the transformation is the angle between the contact patch plane and the wheelset axle, the contact angle δ, corrected for the roll of the wheelset axle relative to the track plane, ϕ_W. Figure B.1 illustrates the necessary rotations at each rail. Since the combination of the contact angle and the wheelset roll angle appears frequently, it is convenient to define the angle γ between the contact patch and the P frame. The transformations for the left and right rails are thus:

$$\vec{u}_{\{CPL\}} = \begin{pmatrix} 1 & 0 & 0 \\ 0 & \cos(\gamma_L) & \sin(\gamma_L) \\ 0 & -\sin(\gamma_L) & \cos(\gamma_L) \end{pmatrix} \vec{u}_{\{P\}}$$

$$\vec{u}_{\{CPR\}} = \begin{pmatrix} 1 & 0 & 0 \\ 0 & \cos(\gamma_R) & -\sin(\gamma_R) \\ 0 & \sin(\gamma_R) & \cos(\gamma_R) \end{pmatrix} \vec{u}_{\{P\}}$$

where:

$$\gamma_L = \delta_L + \phi_W$$

$$\gamma_R = \delta_R - \phi_W$$

Relation (B.1.7) gives the inertial velocity of an arbitrary point fixed with respect to the W system, expressed in P and 2 system coordinates. These terms may be transformed to the left and right contact patch planes. Using the small angle and small angular rates approximations, with $\cos\delta = \cos\gamma \pm \phi_W \sin\gamma$ and $\sin\delta = \sin\gamma \pm \phi_W \cos\gamma$, and noting that $r\omega_{WX} - z_W\dot{\phi}_{TR} \approx r\dot{\phi}_W$, one finds the following:

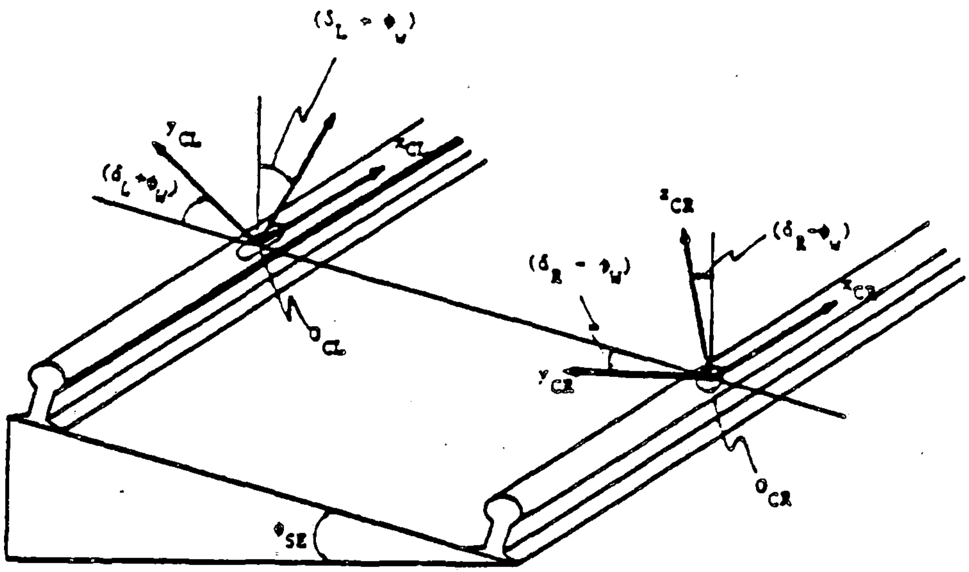

$$\begin{Bmatrix} \hat{i}_{CL} \\ \hat{j}_{CL} \\ \hat{k}_{CL} \end{Bmatrix} \begin{bmatrix} 1 & 0 & 0 \\ 0 & c(\delta_L + \phi_W) & s(\delta_L + \phi_W) \\ 0 & -s(\delta_L + \phi_W) & c(\delta_L + \phi_W) \end{bmatrix} \begin{Bmatrix} \hat{i}_J \\ \hat{j}_T \\ \hat{k}_T \end{Bmatrix} ; \begin{Bmatrix} \hat{i}_{CR} \\ \hat{j}_{CR} \\ \hat{k}_{CR} \end{Bmatrix} = \begin{bmatrix} 1 & 0 & 0 \\ 0 & c(\delta_R - \phi_W) & s(\delta_R - \phi_W) \\ 0 & s(\delta_R - \phi_W) & c(\delta_R - \phi_W) \end{bmatrix} \begin{Bmatrix} \hat{i}_T \\ \hat{j}_T \\ \hat{k}_T \end{Bmatrix}$$

Figure B.1 Diagram showing the contact patch coordinate systems.

$$\begin{pmatrix} w_{LX} \\ w_{LY} \\ w_{LZ} \end{pmatrix}_{\{CPL\}} = \frac{d}{dt}\left({}^{I}\vec{R}_{W}^{CPL}\right) - \frac{d}{dt}\left({}^{I}\vec{R}_{R}^{CPL}\right) \tag{B.2.3}$$

where:

$$w_{LX} = V - r_L\dot{\theta}_W - a\omega_{WZ}$$

$$\begin{aligned} w_{LY} = {} & \cos(\gamma_L)(\dot{y}_W - \dot{y}_{LR} + r_L\dot{\phi}_W) \\ & + \sin(\gamma_L)(\dot{z}_W + a\dot{\phi}_{SE} + a\omega_{WX} - \Delta_L\dot{\theta}_W) \end{aligned}$$

$$\begin{aligned} w_{LZ} = {} & \cos(\gamma_L)(\dot{z}_W + a\dot{\phi}_{SE} + a\omega_{WX} - \Delta_L\dot{\theta}_W) \\ & - \sin(\gamma_L)(\dot{y}_W - \dot{y}_{LR} + r_L\dot{\phi}_W) \end{aligned}$$

$$\begin{pmatrix} w_{RX} \\ w_{RY} \\ w_{RZ} \end{pmatrix}_{\{CPR\}} = \frac{d}{dt}\left({}^{I}\vec{R}_{W}^{CPR}\right) - \frac{d}{dt}\left({}^{I}\vec{R}_{R}^{CPR}\right) \tag{B.2.4}$$

where:

$$w_{RX} = V - r_R\dot{\theta}_W + a\omega_{WZ}$$

$$\begin{aligned} w_{RY} = {} & \cos(\gamma_R)(\dot{y}_W - \dot{y}_{RR} + r_R\dot{\phi}_W) \\ & - \sin(\gamma_R)(\dot{z}_W + a\dot{\phi}_{SE} - a\omega_{WX} + \Delta_R\dot{\theta}_W) \end{aligned}$$

$$\begin{aligned} w_{RZ} = {} & \cos(\gamma_R)(\dot{z}_W + a\dot{\phi}_{SE} - a\omega_{WX} + \Delta_R\dot{\theta}_W) \\ & + \sin(\gamma_R)(\dot{y}_W - \dot{y}_{RR} + r_R\dot{\phi}_W) \end{aligned}$$

B.2.3 Wheel / Rail Contact Constraint

The constraint that wheel and rail remain in contact implies that $w_{LZ} = 0$ and $w_{RZ} = 0$. That is, normal to the plane of contact, there is no relative motion between wheel and rail. These constraints will be used to simplify the creepages in the following section. Formally,

$$\boxed{\begin{aligned} w_{LZ} &= \cos(\gamma_L)(\dot{z}_W + a\dot{\phi}_{SE} + a\omega_{WX} - \Delta_L\dot{\theta}_W) \\ &\quad - \sin(\gamma_L)(\dot{y}_W - \dot{y}_{LR} + r_L\dot{\phi}_W) \\ &= 0 \\ \\ w_{RZ} &= \cos(\gamma_R)(\dot{z}_W + a\dot{\phi}_{SE} - a\omega_{WX} + \Delta_R\dot{\theta}_W) \\ &\quad + \sin(\gamma_R)(\dot{y}_W - \dot{y}_{RR} + r_R\dot{\phi}_W) \\ &= 0 \end{aligned}} \tag{B.2.5}$$

B.2.4 Wheel / Rail Creepages

The wheel/rail creepage represents the rigid slip between a small patch of steel on the wheel and a patch on the rail at the wheel/rail contact patch, normalized with respect to the velocity of the vehicle [15]. The creepages are considered in terms of their longitudinal, lateral, and spin components, defined in the contact patch coordinate systems. If the translational and rotational velocities of the wheel at the point of contact are given by $\vec{W}$ and ${}^{I}\vec{\omega}^{W}$, and the rail has only a lateral velocity given by R_Y, then the following definitions give the creepages,

$$\begin{aligned} \xi_{CX} &= \frac{1}{V}(\vec{W} - \vec{R}) \cdot \hat{\imath}_{CP} = \frac{1}{V}(W_X) \\ \xi_{CY} &= \frac{1}{V}(\vec{W} - \vec{R}) \cdot \hat{\jmath}_{CP} = \frac{1}{V}(W_Y - R_Y) \\ \xi_{CSP} &= \frac{1}{V}\left({}^{I}\vec{\omega}^{W} - {}^{I}\vec{\omega}^{R}\right) \cdot \hat{k}_{CP} = \frac{1}{V}\ {}^{I}\vec{\omega}^{W} \cdot \hat{k}_{CP} \end{aligned}$$

For the purpose of calculating the creepages, the lateral and longitudinal velocity of the wheel may be found with (B.1.7), (B.3.4), and (B.3.5) using the angular velocity of the W system and the positions of the contact patches. The creepage definitions may be used with the relations thus found to determine the longitudinal and lateral creepages at the left and right contact patches.

The translational creepages are then given below. As previously noted, the lateral rail velocities are taken to be zero in the computational model for numerical reasons. It is included in these expressions for completeness.

$$\xi_{CXL} = \frac{1}{V}\left\{V - r_L\dot{\theta}_W - a\omega_{WZ}\right\}$$

$$\xi_{CYL} = \frac{1}{V\cos(\gamma_L)}\left\{\dot{y}_W + r_L(\dot{\phi}_W - \dot{\theta}_W\psi_W) - \dot{y}_{LR})\right\}$$

$$\xi_{CXR} = \frac{1}{V}\left\{V - r_R\dot{\theta}_W + a\omega_{WZ}\right\}$$

$$\xi_{CYR} = \frac{1}{V\cos(\gamma_R)}\left\{\dot{y}_W + r_R(\dot{\phi}_W - \dot{\theta}_W\psi_W) - \dot{y}_{RR})\right\} \tag{B.2.6}$$

Applying the definition of the spin creepage, relations may be found for the left and right contact patches. After cancelling the products of small angles and small angular rates,

$$\xi_{CSPL} = \frac{1}{V}\left\{ - \sin(\delta_L)\dot{\theta}_W + \cos(\delta_L)\omega_{WZ}\right\}$$

$$\xi_{CSPR} = \frac{1}{V}\left\{\sin(\delta_R)\dot{\theta}_W + \cos(\delta_R)\omega_{WZ}\right\} \tag{B.2.7}$$

B.3 Contact Patch Forces and Moments

The forces developed at the wheel/rail contact patches have a large effect on the dynamic performance and energy dissipation of a rail vehicle. The total force at a contact patch is the sum of the normal force, which acts perpendicular to the plane of contact, and the frictional creep force, which act in the plane of contact.

Transformations to contact patch coordinates and the creepage expressions were derived in the previous section. These relations are used in the present development of the calculation of the creep forces and their resolution in the P and 2 frames of reference.

B.3.1 Wheel / Rail Creep Forces

Following the method of Kalker [15] (see also Elkins and Eickhoff [17]), the creepages are normalized using contact patch data. The normalization depends upon the coefficient of friction and the geometry of the wheel/rail contact. The method given below is consistent with recent evidence that the creep force does not depend upon the friction coefficient for low creepages.

$$\epsilon = f\frac{\rho\xi_{CX}}{\mu c} \qquad \eta = f\frac{\rho\xi_{CY}}{\mu c} \qquad \chi = f\frac{\rho\xi_{CSP}}{\mu} \tag{B.3.1}$$

where:

$f =$ constant factor, equal to 1.0 for full Kalker method

$c = \sqrt{ab}$

$a =$ major axis of contact ellipse

$b =$ minor axis of contact ellipse

$$\frac{1}{\rho} = \frac{1}{4}\left(\frac{1}{R_1^+} + \frac{1}{R_1^-} + \frac{1}{R_2^+} + \frac{1}{R_2^-}\right)$$

$R_1^{\pm} =$ principal radii of curvature of rail

$R_2^{\pm} =$ principal radii of curvature of wheel

These normalized creepages are used in a procedure in the computational model which performs a table lookup to arrive at normalized creep forces in the longitudinal and lateral contact patch directions, τ_X and τ_Y. This procedure is based on the output from Kalker's DUVOROL program, as modified by British Rail. The normalized forces must be multiplied by the maximum frictional force, μF_N, to get the actual friction forces in the contact patch plane, F_{CPX} and F_{CPY}.

$$\boxed{\begin{aligned} F_{CPX} &= \mu\, F_N\, \tau_X(\epsilon, \eta, \chi) \\ F_{CPY} &= \mu\, F_N\, \tau_Y(\epsilon, \eta, \chi) \end{aligned} \qquad \text{(B.3.2)}}$$

The normal force is the only other force acting between wheel and rail, which can be written as F_N. The vector sum of these components will be denoted $\vec{P}$ for "patch" forces; these forces will be discussed in depth below.

The power dissipated at the contact patch is taken as the dot product of the creep force and the relative velocity between wheel and rail. The former consists of longitudinal and lateral components, in the plane of contact, determined by Kalker's method. The relative velocity between the two bodies is obtained as the product of the velocity of the vehicle V and the creepages in the component directions. Writing the power separately in the longitudinal and lateral directions, and inserting negative signs to yield positive values for energy dissipation,

$$\boxed{\begin{aligned} P_{CPX} &= -F_{CPX} V\, \xi_{CX} \\ P_{CPY} &= -F_{CPY} V\, \xi_{CY} \end{aligned} \qquad \text{(B.3.3)}}$$

B.3.2 Resolution of the Contact Patch Forces

The creep forces and the normal loads must be transformed to P frame coordinates for consideration of their longitudinal, lateral, and vertical effects. When these forces are transformed to the 2 frame of the wheelset, and when the position vector of the contact patch relative to the wheelset center of gravity is expressed in 2 coordinates, the torque on the wheelset due to these forces may be found.

The contact patch forces will be written in a fashion to facilitate the developments of the next section. In particular, the creep and normal forces and moments will be kept separate, for they will be treated differently. The forces may be transformed to the P coordinate system for the purposes of translational considerations. These components will then be transformed to the 2 frame of reference, and the cross-product with the position vector of the contact patch will then give the moments acting on the wheelset.

Inverting transformation matrices presented previously, vectors may be transformed from contact patch coordinates to those of the P and 2 frames. For the left wheel:

$$\vec{u}_{\{P\}} = \begin{pmatrix} 1 & 0 & 0 \\ 0 & \cos(\gamma_L) & -\sin(\gamma_L) \\ 0 & \sin(\gamma_L) & \cos(\gamma_L) \end{pmatrix} \vec{u}_{\{CPL\}}$$

$$\vec{u}_{\{2\}} = \begin{pmatrix} 1 & \psi_W \cos(\gamma_L) & -\psi_W \sin(\gamma_L) \\ -\psi_W & \cos(\delta_L) & -\sin(\delta_L) \\ 0 & \sin(\delta_L) & \cos(\delta_L) \end{pmatrix} \vec{u}_{\{CPL\}}$$

For the right wheel, the transformations are:

$$\vec{u}_{\{P\}} = \begin{pmatrix} 1 & 0 & 0 \\ 0 & \cos(\gamma_R) & \sin(\gamma_R) \\ 0 & -\sin(\gamma_R) & \cos(\gamma_R) \end{pmatrix} \vec{u}_{\{CPR\}}$$

$$\vec{u}_{\{2\}} = \begin{pmatrix} 1 & \psi_W \cos(\gamma_R) & \psi_W \sin(\gamma_R) \\ -\psi_W & \cos(\delta_R) & \sin(\delta_R) \\ 0 & -\sin(\delta_R) & \cos(\delta_R) \end{pmatrix} \vec{u}_{\{CPR\}}$$

Conversion of the contact patch forces at the left wheel to the P frame yields the following results:

$$\vec{P}_L = \begin{pmatrix} F_{CPXL} \\ F_{CPYL} \\ F_{NL} \end{pmatrix}_{\{CPL\}} = \begin{pmatrix} F_{XL} \\ F_{YL} \\ F_{ZL} \end{pmatrix}_{\{P\}} = \begin{pmatrix} F_{CXL} \\ F_{CYL} + F_{NYL} \\ F_{CZL} + F_{NZL} \end{pmatrix}_{\{P\}} \tag{B.3.4}$$

where:

$$F_{CXL} = F_{CPXL}$$
$$F_{CYL} = \cos(\gamma_L) F_{CPYL}$$
$$F_{NYL} = -\sin(\gamma_L) F_{NL}$$
$$F_{CZL} = \sin(\gamma_L) F_{CPYL}$$
$$F_{NZL} = \cos(\gamma_L) F_{NL}$$

This relation defines the P frame components of the creep and normal forces at the left wheel. It should be mentioned that the N subscripts correspond to the normal forces; the C subscripts relate to the creep forces; the L indicates the left side; an R is used to indicate the right side. For the right wheel,

$$\vec{P}_R = \begin{pmatrix} F_{CPXR} \\ F_{CPYR} \\ F_{NR} \end{pmatrix}_{\{CPR\}} = \begin{pmatrix} F_{XR} \\ F_{YR} \\ F_{ZR} \end{pmatrix}_{\{P\}} = \begin{pmatrix} F_{CXR} \\ F_{CYR} + F_{NYR} \\ F_{CZR} + F_{NZR} \end{pmatrix}_{\{P\}} \tag{B.3.5}$$

where:

$$F_{CXR} = F_{CPXR}$$
$$F_{CYR} = \cos(\gamma_R) F_{CPYR}$$
$$F_{NYR} = \sin(\gamma_R) F_{NR}$$
$$F_{CZR} = -\sin(\gamma_R) F_{CPYR}$$
$$F_{NZR} = \cos(\gamma_R) F_{NR}$$

Thus the forces due to creep and normal forces are determined for left and right wheels in the P frame. The rotational kinematic equations for the wheelset consider the torques about each axis in the 2 coordinate system. The position vectors of the contact patches are given in (B.2.1); these relations express the positions in the 2 frame. The contact forces, expressed above in the P system, may be transformed to the 2 frame. The torques due to wheel/rail contact are then given by the vector cross-product, as follows:

$$\vec{r}_L \times \vec{P}_L = \begin{pmatrix} M_{XL} \\ M_{YL} \\ M_{ZL} \end{pmatrix}_{\{2\}} = \begin{pmatrix} M_{CXL} + M_{NXL} \\ M_{CYL} + M_{NYL} \\ M_{CZL} + M_{NZL} \end{pmatrix}_{\{2\}} \tag{B.3.6}$$

where:

$$M_{CXL} = -r_L\psi_W F_{CXL} + (r_L - a\phi_W)F_{CYL} + (r_L\phi_W + a)F_{CZL}$$
$$M_{NXL} = (r_L - a\phi_W)F_{NYL} + (r_L\phi_W + a)F_{NZL}$$
$$M_{CYL} = -r_L F_{CXL} - r_L\psi_W F_{CYL} - \Delta_L F_{CZL}$$
$$M_{NYL} = -r_L\psi_W F_{NYL} - \Delta_L F_{NZL}$$
$$M_{CZL} = -aF_{CXL} + (\Delta_L - a\psi_W)F_{CYL}$$
$$M_{NZL} = (\Delta_L - a\psi_W)F_{NYL}$$

$$\vec{r}_R \times \vec{P}_R = \begin{pmatrix} M_{XR} \\ M_{YR} \\ M_{ZR} \end{pmatrix}_{\{2\}} = \begin{pmatrix} M_{CXR} + M_{NXR} \\ M_{CYR} + M_{NYR} \\ M_{CZR} + M_{NZR} \end{pmatrix}_{\{2\}} \tag{B.3.7}$$

where:

$$M_{CXR} = -r_R\psi_W F_{CXR} + (r_R + a\phi_W)F_{CYR} + (r_R\phi_W - a)F_{CZR}$$
$$M_{NXR} = (r_R + a\phi_W)F_{NYR} + (r_R\phi_W - a)F_{NZR}$$
$$M_{CYR} = -r_R F_{CXR} - r_R\psi_W F_{CYR} + \Delta_R F_{CZR}$$
$$M_{NYR} = -r_R\psi_W F_{NYR} + \Delta_R F_{NZR}$$
$$M_{CZR} = aF_{CXR} - (\Delta_R - a\psi_W)F_{CYR}$$
$$M_{NZR} = -(\Delta_R - a\psi_W)F_{NYR}$$

B.4 Wheelset Equations of Motion

The basic kinematics of a wheelset have been presented in the first section of this appendix. The actual wheelset equations of motion may be found using those relations with the contact patch forces discussed above, as well as the forces and moments applied by the suspension connection to the "truck" (which happens to be the carbody in this instance). Figure B.2 illustrates the forces and moments applied to the wheelset system.

It may be simply stated that the truck exerts a lateral force F_{TWY} and a vertical force F_{TWZ} **on** the wheelset, as well as a roll moment M_{TWX} and yaw moment M_{TWZ}. These forces and moments, in addition to the contact forces, are those that influence the wheelset.

The degrees of freedom for the wheelset consist of lateral, yaw, and spin states. (In the computational model, the spin perturbation, or difference from nominal spin rate, is integrated. Technically, the perturbation is considered to be a "half-degree of freedom." However, this has no effect on the equations considered here.)

The equations of motion are derived for the most general case of two points of contact (tread and flange) at each wheelset. Single-point tread contact is an ordinary type of contact condition, requiring calculations for one contact patch at each wheel. Two points of contact may occur at a single wheel within a small range of lateral excursion at the inception of flange contact with the rail. At further lateral excursions, single-point contact on the flange may occur at a wheel, again requiring only one contact patch. The non-flanging wheel experiences a single point of tread contact when the flanging wheel is in two-point or single-point flange contact.

Despite these complexities, the equations can be written to assume two points of wheel/rail contact at each wheel, and the several cases described above are then degenerate cases in which the forces at one or two of the wheelset contact patches are taken to be zero. Note that a 1 is used to represent the first point of contact at the left or right wheel; in the instance of single-point contact, this

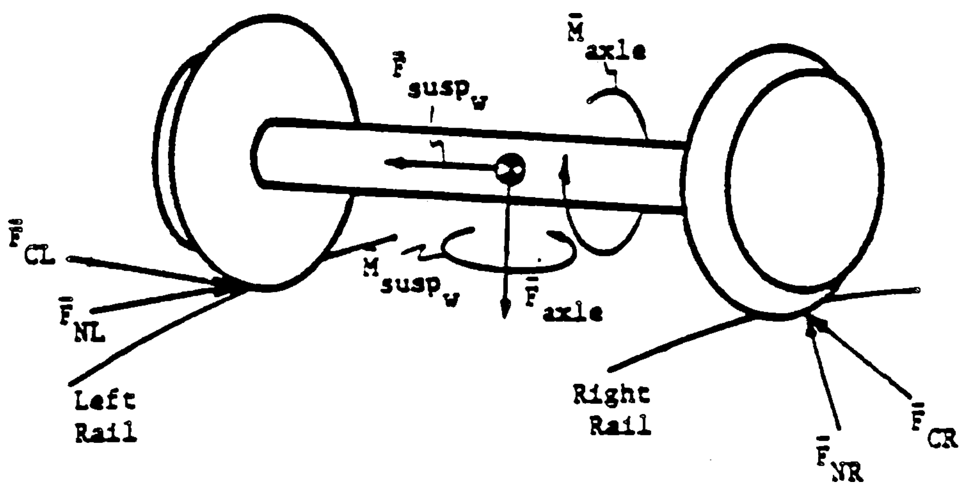

Figure B.2 Diagram showing the forces and moments applied to the wheelset.

is the only active contact condition. A 2 is used to indicate the second point of contact if one exists.

It is common in vehicle dynamic analyses to define the cant deficiency, ϕ_{def}, which represents the net lateral force per unit weight acting on a mass due to the combined effects of curving and superelevation,

$$\phi_{def} = \frac{V^2}{g}\rho - \phi_{SE}$$

Additionally, it is fruitful to define the component-wise sums of the wheel/rail forces and moments. It is also useful to simultaneously define the normal and creep contributions of each of these.

$$
\begin{aligned}
F_X &= F_{CX} + F_{NX} \\
&= F_{CXL1} + F_{CXL2} + F_{CXR1} + F_{CXR2} \\
&\quad + F_{NXL1} + F_{NXL2} + F_{NXR1} + F_{NXR2}
\end{aligned}
\tag{B.4.1}
$$

$$
\begin{aligned}
F_Y &= F_{CY} + F_{NY} \\
&= F_{CYL1} + F_{CYL2} + F_{CYR1} + F_{CYR2} \\
&\quad + F_{NYL1} + F_{NYL2} + F_{NYR1} + F_{NYR2}
\end{aligned}
$$

$$
\begin{aligned}
F_Z &= F_{CZ} + F_{NZ} \\
&= F_{CZL1} + F_{CZL2} + F_{CZR1} + F_{CZR2} \\
&\quad + F_{NZL1} + F_{NZL2} + F_{NZR1} + F_{NZR2}
\end{aligned}
$$

$$
\begin{aligned}
M_X &= M_{CX} + M_{NX} \\
&= M_{CXL1} + M_{CXL2} + M_{CXR1} + M_{CXR2} \\
&\quad + M_{NXL1} + M_{NXL2} + M_{NXR1} + M_{NXR2}
\end{aligned}
$$

$$
\begin{aligned}
M_Y &= M_{CY} + M_{NY} \\
&= M_{CYL1} + M_{CYL2} + M_{CYR1} + M_{CYR2} \\
&\quad + M_{NYL1} + M_{NYL2} + M_{NYR1} + M_{NYR2}
\end{aligned}
$$

$$
\begin{aligned}
M_Z &= M_{CZ} + M_{NZ} \\
&= M_{CZL1} + M_{CZL2} + M_{CZR1} + M_{CZR2} \\
&\quad + M_{NZL1} + M_{NZL2} + M_{NZR1} + M_{NZR2}
\end{aligned}
$$

B.4.1 Solution of Vertical and Roll Equations

The wheelset lateral, yaw, and spin equations of motion are solved for the rate of acceleration of the respective state variable. In the computational model, these derivatives are used to integrate the motion at each timestep. The wheelset vertical and roll equations are also considered, for they are necessary to determine the normal forces at the wheel/rail contact patches.

For single point contact at each wheel, the problem is well-posed in that two equations are available to solve for two unknowns. Computationally, the normal loads from the previous timestep are updated at each timestep. When there is two-point contact at a wheel, the problem is no longer well-posed in that there are now three unknown normal loads and two equations to be satisfied. The modeling approach adopted here is to develop a relationship between the two normal loads at the wheel which is in two-point contact (Blader, 1986). This relation specifies the distribution of the normal load between the tread and flange contact patches, depending upon how far the wheel has traveled across the zone of two-point contact.

From previous kinematic expressions (B.1.4) and (B.1.5), and knowledge of the forces and moments influencing the wheelset, the vertical and roll equations may be written as follows:

Wheelset Vertical Equation

$$m_W \left[\check{z}_W + \phi_{TR} V^2 \rho + a \check{\phi}_{SE} + y_W \check{\phi}_{TR} \right] = F_Z + F_{TWZ} - m_W g$$

Wheelset Roll Equation

$$\check{\phi}_W = \frac{1}{I_{WX}} \left[(M_X + M_{TWX}) + I_{WY} \dot{\theta}_W \omega_{WZ} \right] - \check{\phi}_{TR}$$

Now use (B.4.1) to expand the F_Z and M_X terms. In doing so, the relations of (B.3.2) may be used to express the dependency of the creep forces on the normal loads, and (B.3.4) through (B.3.7) provide the detailed composition of each wheel/rail interaction. In this analysis, the dominant moment terms are preserved and the lower order terms are neglected.

It is useful to recognize that the total wheel/rail vertical interaction consists of terms such as:

$$(\cos\gamma \pm \mu\tau_Y \sin\gamma)F_N$$

and the total lateral interaction includes terms such as:

$$(\mu\tau_Y \cos\gamma \pm \sin\gamma)F_N$$

Note that τ_Y depends on F_N through a one-third power term in the normalization for the Kalker table, which is a relatively weak dependence, with the result that often the previous values for F_N are sufficient to determine the value of τ_Y. However, it is reasonable to iterate once if the change in normal load from the previous value is great, as might be expected during wheelset flanging.

To simplify the expression of these relations, define the following geometric and force terms (for $i = 1$ or 2 for the first or second point of wheel/rail contact):

$$\begin{aligned}
\epsilon_{Li} &= \cos(\gamma_{Li}) + \mu\tau_{YL}\sin(\gamma_{Li}) \\
\epsilon_{Ri} &= \cos(\gamma_{Ri}) - \mu\tau_{YR}\sin(\gamma_{Ri}) \\
\nu_{Li} &= \mu\tau_{YL}\cos(\gamma_{Li}) - \sin(\gamma_{Li}) \\
\nu_{Ri} &= \mu\tau_{YR}\cos(\gamma_{Ri}) + \sin(\gamma_{Ri}) \\
\\
F_\Sigma &= m_W\left[g + \check{z}_W + \phi_{TR}V^2\rho + a\check{\phi}_{SE} + y_W\check{\phi}_{TR}\right] - F_{TWZ} \\
M_\Sigma &= I_{WX}(\check{\phi}_{TR} + \check{\phi}_W) - I_{WY}\dot{\theta}_W\omega_{WZ} - M_{TWX}
\end{aligned} \tag{B.4.2}$$

Then the wheelset vertical equation may be rewritten as follows:

$$F_\Sigma = \epsilon_{L1}F_{NL1} + \epsilon_{L2}F_{NL2} + \epsilon_{R1}F_{NR1} + \epsilon_{R2}F_{NR2}$$

Similarly, the wheelset roll equation may be expressed as the following (where the rolling radius r^* is generally equal to the nominal rolling radius r_o):

$$M_\Sigma = a\Big[\epsilon_{L1}F_{NL1} + \epsilon_{L2}F_{NL2} - \epsilon_{R1}F_{NR1} - \epsilon_{R2}F_{NR2}\Big] + r^*\Big[\nu_{L1}F_{NL1} + \nu_{L2}F_{NL2} + \nu_{R1}F_{NR1} + \nu_{R2}F_{NR2}\Big]$$

It is now necessary to derive the relation between the normal loads during two point contact. Two parameters, β_L and β_R, are defined as functions of wheelset excursion. When the wheelset is in two-point contact, the net excursion of wheel relative to rail, y_{NET}, is between two values $|y_{TREAD}|$ and $|y_{FLANGE}|$, which are determined by examination of the wheel/rail contact profile. The value of the net excursion, y_{NET}, is positive during two-point contact on the left, and it is negative during two-point contact on the right. Both $|y_{TREAD}|$ and $|y_{FLANGE}|$ are defined to be positive, and the current net wheelset excursion is compared with these values.

The modelling assumption to be made here is that the vertical component of the total normal load, summed over the two patches, is distributed between the two patches on the basis of the net wheelset excursion across the two-point band. The definitions are thus as follows:

$$F_{NL2} = \beta_L \; F_{NL1} \tag{B.4.3}$$
$$F_{NR2} = \beta_R \; F_{NR1}$$

where:

$$\beta_L = \left(\frac{y_{NET} - |y_{TREAD}|}{|y_{FLANGE}| - y_{NET}} \right) \cdot \left(\frac{\cos(\gamma_{L1})}{\cos(\gamma_{L2})} \right)$$
$$\text{if} \quad |y_{TREAD}| < y_{NET} < |y_{FLANGE}|$$
$$\beta_L = 0 \qquad \text{otherwise}$$

$$\beta_R = - \left(\frac{y_{NET} + |y_{TREAD}|}{|y_{FLANGE}| + y_{NET}} \right) \cdot \left(\frac{\cos(\gamma_{R1})}{\cos(\gamma_{R2})} \right)$$
$$\text{if} \quad - |y_{TREAD}| > y_{NET} > - |y_{FLANGE}|$$
$$\beta_R = 0 \qquad \text{otherwise}$$

This algorithm satisfies the desired boundary conditions. As the net wheelset excursion approaches the tread or flange boundary of the two-point contact zone, the normal loads approach that of single-point contact at tread and flange contact, respectively. Thus, there is continuity in the normal loads at the tread and flange boundaries of two-point contact. It is important to note that the geometric discontinuities at the contact patches of tread and flange are used, even though the wheelset excursion passes continuously through the two-point contact zone.

Thus, the above relations for the wheelset vertical and roll equations may be written in terms of two unknowns, F_{NL1} and F_{NR1}, using the following definitions:

$$\epsilon_L = \epsilon_{L1} + \beta_L \epsilon_{L2}$$
$$\epsilon_R = \epsilon_{R1} + \beta_L \epsilon_{R2}$$
$$\nu_L = \nu_{L1} + \beta_L \nu_{L2}$$
$$\nu_R = \nu_{R1} + \beta_L \nu_{R2}$$

with the following results:

$$F_\Sigma = \epsilon_L F_{NL1} + \epsilon_R F_{NR1}$$

$$M_\Sigma = a\Big[\epsilon_L F_{NL1} - \epsilon_R F_{NR1}\Big] + r^*\Big[\nu_L F_{NL1} + \nu_R F_{NR1}\Big]$$

These two equations may now be used to derive the left and right wheelset normal loads at the first point of contact. The appropriate value for the second point of contact is given by the relation $F_2 = \beta F_1$ as above:

$$F_{NL1} = \frac{(a\epsilon_R - r^*\nu_R)F_\Sigma + \epsilon_R M_\Sigma}{\Delta} \tag{B.4.4}$$

$$F_{NR1} = \frac{(a\epsilon_L + r^*\nu_L)F_\Sigma - \epsilon_L M_\Sigma}{\Delta}$$

where:

$$\Delta = \epsilon_R(a\epsilon_L + r^*\nu_L) + \epsilon_L(a\epsilon_R - r^*\nu_R)$$

During severe flanging, occasionally a negative value for a normal load is generated with $r^* = r_o$. This has been found to be a result of the inclusion of the lateral normal and creep forces in the wheelset roll equation. Rather than proceed with negative loads, a compromise approach has been taken. If a negative normal load is calculated, the value of r^* is reduced by 20 % from its previous value, and the loads are then recalculated. If a negative load still results, this process is repeated. If r^* is driven to zero and a negative load is still obtained, true wheel lift is declared. It is thought that high frequency dynamics are involved in these very short duration wheel lifts with $r^* = r_o$, which are characteristically different from wheel lift which lasts on the order of a fraction of a second. This approach has proven to work reasonably well in practice.

B.4.2 Formulation of the Wheelset State Equations

In the computational model, the normal and creep forces are determined in the contact patch frame. These forces are then resolved into their components in the P frame, and the moments are calculated in the 2 frame of reference. The lateral, spin, and yaw accelerations are then found; these state equations are given below.

Wheelset Lateral State Equation (B.4.5)

$$\breve{y}_W = g\phi_{def} - g\phi_{CR} + z_W\breve{\phi}_{TR} + \frac{1}{m_W}[F_Y + F_{TWY}]$$

Wheelset Spin State Equation (B.4.6)

$$\breve{\theta}_W = \frac{1}{I_{WY}}M_Y - \phi_W\frac{1}{I_{WZ}}[M_Z + M_{TWZ}] + \phi_{TR}V\dot{\rho} + \psi_W\breve{\phi}_{TR}$$

Wheelset Yaw State Equation (B.4.7)

$$\breve{\psi}_W = \frac{1}{I_{WZ}}\left[M_Z + M_{TWZ} - I_{WY}\mathring{\theta}_W\omega_{WX}\right] + V\dot{\rho}$$

Appendix C

Carbody and Suspension Model

The carbody has five rigid body degrees of freedom (lateral, vertical, roll, pitch, and yaw) and three flexible body modes (twist, lateral, and vertical bending). This appendix considers the development of the vehicle suspension forces and their use in determining the state equations for the above degrees of freedom.

The kinematics of Appendix A are applied to determine the suspension strokes at each of the four connections between the carbody and wheelsets. At each such connection, there are longitudinal, lateral, and vertical suspension elements. Using the suspension strokes and the element constitutive relations, the suspension forces are determined. With these suspension forces, the force and moment summations applied to the carbody and wheelsets may be determined. The carbody state equations are then developed, resorting once more to Appendix A.

C.1 Suspension Stroke Equations

In this section, equations for the suspension strokes are presented. Figure C.1 shows the basic geometry of the vehicle. There are four connections between carbody and wheelsets, numbered from 1 to 4. Suspension number 1 refers to the left leading wheel, number 2 indicates the right leading wheel, number 3 indicates the right trailing wheel, and number 4 refers to the right trailing wheel. This is a notation which proceeds clockwise from the position of the left leading wheel. The longitudinal, lateral, and vertical position of each connection is given by the values A_{XDIST}, H_{AFAX}, and V_{ERCOG}, respectively.

The strokes and stroke rates across each suspension are obtained by applying the results of section A.3 with the appropriate geometry data. Since there is a suspension element in each coordinate direction, the difference in position between carbody and wheelset along each axis will be required.

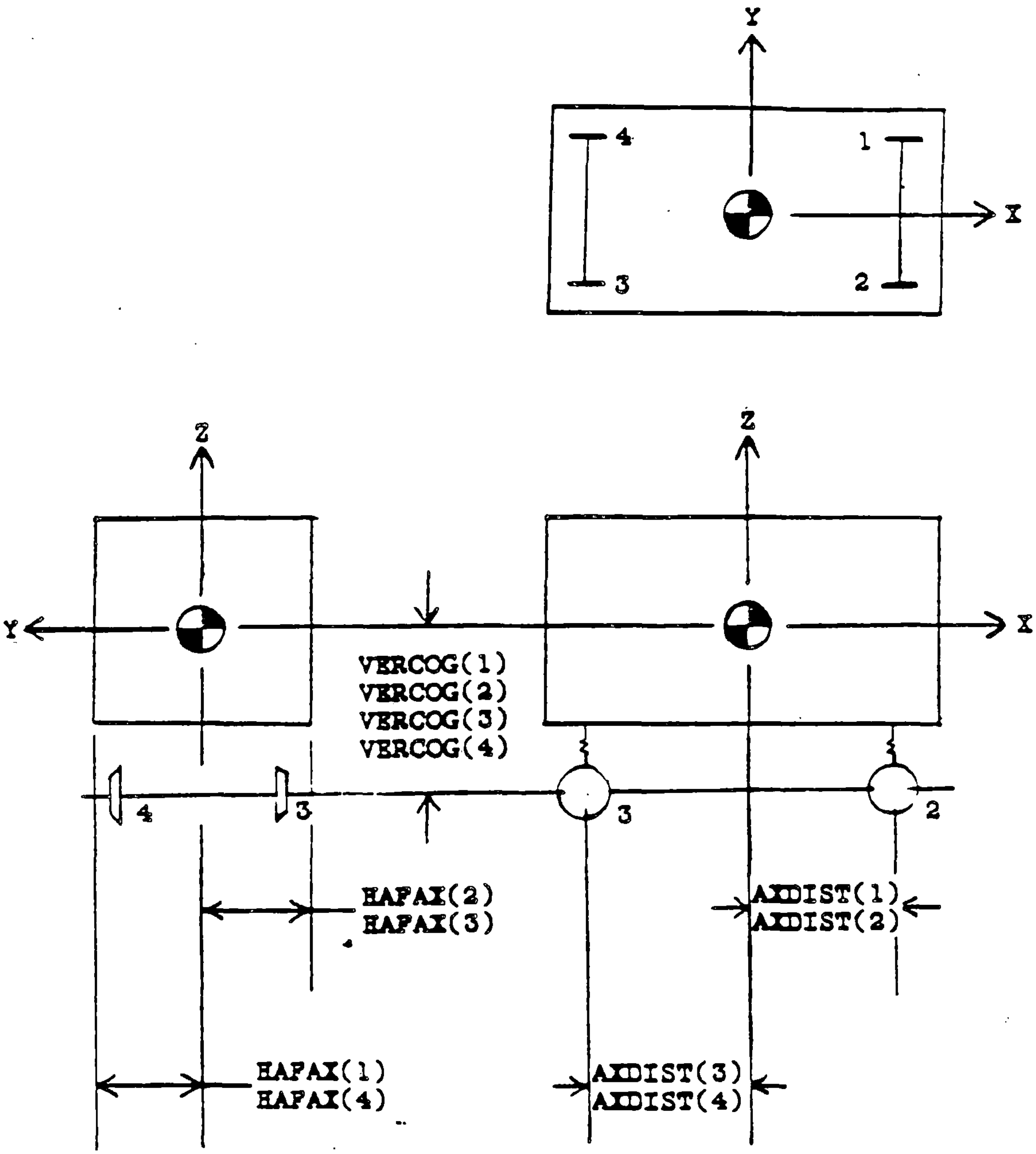

Figure C.1 Diagram showing the geometry of the suspension connections.

Terms starting with M_{OD} also have indices corresponding to the suspension numbering; these are the values of the mode shape functions at the suspension connection points, for each flexible body mode. M_{ODTW}, M_{ODVB}, and M_{ODLB} represent bending about the longitudinal (twist), lateral (vertical bending), and vertical (lateral bending) axes, respectively.

C.1.1 Longitudinal Strokes

The longitudinal suspension model depends upon both the stroke and stroke rates, so both will be shown below. Note that a yaw angle correction term ρA_{XDIST} is necessary because the wheelset frames of reference are rotated relative to the carbody frame about the vertical axis in a curve.

Longitudinal Suspension Strokes (C.1.1)

$$
\begin{aligned}
S_{LON1} &= -H_{AFAX1} \cdot (\psi_{W1} - \psi_C - \rho A_{XDIST1}) \\
S_{LON2} &= H_{AFAX2} \cdot (\psi_{W1} - \psi_C - \rho A_{XDIST2}) \\
S_{LON3} &= H_{AFAX3} \cdot (\psi_{W2} - \psi_C + \rho A_{XDIST3}) \\
S_{LON4} &= -H_{AFAX4} \cdot (\psi_{W2} - \psi_C + \rho A_{XDIST4})
\end{aligned}
$$

$$
\begin{aligned}
\dot{S}_{LON1} &= -H_{AFAX1} \cdot \left(\dot{\psi}_{W1} - \dot{\psi}_C\right) \\
\dot{S}_{LON2} &= H_{AFAX2} \cdot \left(\dot{\psi}_{W1} - \dot{\psi}_C\right) \\
\dot{S}_{LON3} &= H_{AFAX3} \cdot \left(\dot{\psi}_{W2} - \dot{\psi}_C\right) \\
\dot{S}_{LON4} &= -H_{AFAX4} \cdot \left(\dot{\psi}_{W2} - \dot{\psi}_C\right)
\end{aligned}
$$

C.1.2 Lateral Strokes

The lateral suspension model requires knowledge of both strokes and stroke rates, which are given below. Note that, in a curve, the wheelset frame of reference is offset laterally from the carbody by an amount equal to $\frac{1}{2}A_{XDIST}^{2}\rho$.

Lateral Suspension Strokes (C.1.2)

$$\begin{aligned}
S_{LAT1} &= -y_C + y_{W1} - r_o\phi_{CR1} - A_{XDIST1}\cdot(\psi_C + \rho\, A_{XDIST1}/2) \\
&\quad - V_{ERCOG1}\cdot\phi_C - M_{ODLB1}\cdot\zeta_Z - V_{ERCOG1}\cdot M_{ODTW1}\cdot\zeta_X \\
S_{LAT2} &= -y_C + y_{W1} - r_o\phi_{CR1} - A_{XDIST2}\cdot(\psi_C + \rho\, A_{XDIST2}/2) \\
&\quad - V_{ERCOG2}\cdot\phi_C - M_{ODLB2}\cdot\zeta_Z - V_{ERCOG2}\cdot M_{ODTW2}\cdot\zeta_X \\
S_{LAT3} &= -y_C + y_{W2} - r_o\phi_{CR2} + A_{XDIST3}\cdot(\psi_C - \rho\, A_{XDIST3}/2) \\
&\quad - V_{ERCOG3}\cdot\phi_C - M_{ODLB3}\cdot\zeta_Z - V_{ERCOG3}\cdot M_{ODTW3}\cdot\zeta_X \\
S_{LAT4} &= -y_C + y_{W2} - r_o\phi_{CR2} + A_{XDIST4}\cdot(\psi_C - \rho\, A_{XDIST4}/2) \\
&\quad - V_{ERCOG4}\cdot\phi_C - M_{ODLB4}\cdot\zeta_Z - V_{ERCOG4}\cdot M_{ODTW1}\cdot\zeta_X
\end{aligned}$$

$$\begin{aligned}
\dot{S}_{LAT1} &= -\dot{y}_C + \dot{y}_{W1} - r_o\dot{\phi}_{CR1} - A_{XDIST1}\cdot\dot{\psi}_C \\
&\quad - V_{ERCOG1}\cdot\dot{\phi}_C - M_{ODLB1}\cdot\dot{\zeta}_Z - V_{ERCOG1}\cdot M_{ODTW1}\cdot\dot{\zeta}_X \\
\dot{S}_{LAT2} &= -\dot{y}_C + \dot{y}_{W1} - r_o\dot{\phi}_{CR1} - A_{XDIST2}\cdot\dot{\psi}_C \\
&\quad - V_{ERCOG2}\cdot\dot{\phi}_C - M_{ODLB2}\cdot\dot{\zeta}_Z - V_{ERCOG2}\cdot M_{ODTW2}\cdot\dot{\zeta}_X \\
\dot{S}_{LAT3} &= -\dot{y}_C + \dot{y}_{W2} - r_o\dot{\phi}_{CR2} + A_{XDIST3}\cdot\dot{\psi}_C \\
&\quad - V_{ERCOG3}\cdot\dot{\phi}_C - M_{ODLB3}\cdot\dot{\zeta}_Z - V_{ERCOG3}\cdot M_{ODTW3}\cdot\dot{\zeta}_X \\
\dot{S}_{LAT4} &= -\dot{y}_C + \dot{y}_{W2} - r_o\dot{\phi}_{CR2} + A_{XDIST4}\cdot\dot{\psi}_C \\
&\quad - V_{ERCOG4}\cdot\dot{\phi}_C - M_{ODLB4}\cdot\dot{\zeta}_Z - V_{ERCOG4}\cdot M_{ODTW1}\cdot\dot{\zeta}_X
\end{aligned}$$

C.1.3 Vertical Strokes

In contrast to the longitudinal and lateral suspension models, the "beta" model for the vertical suspension (to be described below) requires only the strokes and not the stroke rates. This model will, however, require stroke values saved from the previous timestep. In the following, z_W represents the vertical track input to the wheelsets.

Vertical Suspension Strokes (C.1.3)

$$
\begin{aligned}
S_{VER1} = & -z_C - H_{AFAX1} \cdot \phi_C + A_{XDIST1} \cdot \theta_C \\
& - M_{ODVB1} \cdot \varsigma_Y - H_{AFAX1} \cdot M_{ODTW1} \cdot \varsigma_X + z_{W1} \\
S_{VER2} = & -z_C + H_{AFAX2} \cdot \phi_C + A_{XDIST2} \cdot \theta_C \\
& - M_{ODVB2} \cdot \varsigma_Y + H_{AFAX2} \cdot M_{ODTW2} \cdot \varsigma_X + z_{W2} \\
S_{VER3} = & -z_C + H_{AFAX3} \cdot \phi_C - A_{XDIST3} \cdot \theta_C \\
& - M_{ODVB3} \cdot \varsigma_Y + H_{AFAX3} \cdot M_{ODTW3} \cdot \varsigma_X + z_{W3} \\
S_{VER4} = & -z_C - H_{AFAX4} \cdot \phi_C - A_{XDIST4} \cdot \theta_C \\
& - M_{ODVB4} \cdot \varsigma_Y - H_{AFAX4} \cdot M_{ODTW4} \cdot \varsigma_X + z_{W4}
\end{aligned}
$$

C.2 Suspension Constitutive Relationships

Suspension elements act at each connection location along each of the three coordinate axes. Figure C.2 illustrates the notation used, where F_{LON}, F_{LAT}, and F_{VER} represent the forces acting on the carbody in the longitudinal, lateral, and vertical directions, respectively. Since wheelset longitudinal motion relative to the carbody is neglected, the differences between longitudinal forces on left and right sides result in yaw moments between the bodies.

C.2.1 Longitudinal Suspension Model

The longitudinal suspension model consists of a two-stage spring (representing the swing link stiffness) in parallel with both a Coulomb friction element (representing dry friction in the swing link) and a series spring-damper element (representing the yaw damper). The position of the junction between spring and damper of the series yaw damper element is integrated locally to obtain the force at each timestep. The total longitudinal force may be written as follows:

$$\boxed{F_{LON} = F_{STIFF} + F_{SERIES} + F_{COUL} \qquad \text{(C.2.1)}}$$

where

F_{LON}	total longitudinal suspension force
F_{STIFF}	swing link suspension force
F_{SERIES}	yaw damper force
F_{COUL}	swing link Coulomb friction

The force in the two-stage spring, representing the action of the swing link and its contact with the axle guard, is given as follows:

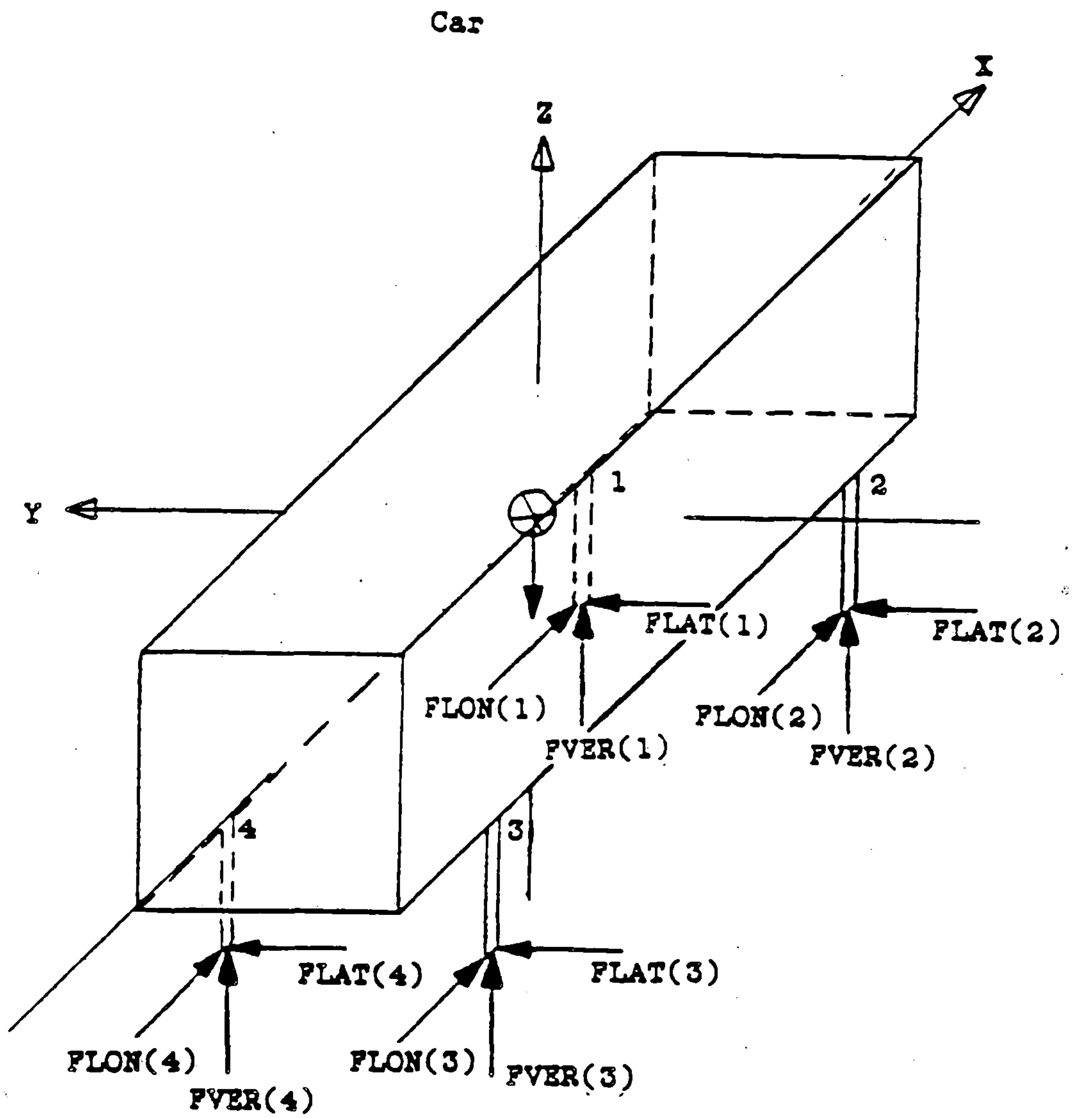

Figure C.2 Diagram showing the notation for the forces acting at each suspension connection.

$$
\begin{aligned}
&If \quad -L_{ONSTP} \leq S_{LON} \leq L_{ONSTP}: \\
&\quad F_{STIFF} = S_{LON} \cdot K_{LON1} \\
&ElseIf \quad S_{LON} > L_{ONSTP}: \\
&\quad F_{STIFF} = L_{ONSTP} \cdot K_{LON1} + (S_{LON} - L_{ONSTP}) \cdot K_{LON2} \\
&ElseIf \quad S_{LON} < L_{ONSTP}: \\
&\quad F_{STIFF} = -L_{ONSTP} \cdot K_{LON1} + (S_{LON} + L_{ONSTP}) \cdot K_{LON2}
\end{aligned}
\tag{C.2.2}
$$

where

L_{ONSTP}	longitudinal suspension clearance
S_{LON}	suspension stroke
K_{LON1}	first stage stiffness
K_{LON2}	second stage stiffness

The force in the yaw damper is found by integrating the time rate of change of displacement across the spring, using the fact that the force in the spring must be equal to that in the damper in the absence of inertial effects.

$$
\begin{aligned}
F_{SERIES}(t_i) = &\; F_{SERIES}(t_{i-1}) \\
&+ K_{BUSH} \cdot \left(\dot{S}_{LON} - \dot{x}_2(F_{SERIES}(t_i))\right) \cdot \Delta_T
\end{aligned}
\tag{C.2.3}
$$

where

K_{BUSH}	yaw damper bushing stiffness
$\dot{S}_{LON}$	longitudinal suspension stroke rate
$\dot{x}_2$	velocity of junction between spring and damping elements of the yaw damper
Δ_T	integration time step

The velocity of the junction between spring and damper is found by inverting the force - stroke rate relation of the damper, which is determined by a piecewise-linear relationship. If the current force in the yaw damper, F_{SERIES}, lies between two values F_{SC1} and F_{SC2} of the characteristic, then the velocity $\dot{x}_2$ is determined in the interval from V_{SC1} to V_{SC2} as follows:

$$\dot{x}_2 = V_{SC1} + \frac{V_{SC2} - V_{SC1}}{F_{SC2} - F_{SC1}} \cdot (F_{SERIES} - F_{SC1}) \tag{C.2.4}$$

Finally, the longitudinal Coulomb friction in the swing links, F_{COUL}, is calculated using the linear viscous band model:

$$F_{COUL} = \begin{cases} -F_{BREAK} & \text{if } \dot{S}_{LON} < -\delta \\ (\dot{S}_{LON}/\delta)F_{BREAK} & \text{if } -\delta < \dot{S}_{LON} < \delta \\ F_{BREAK} & \text{if } \dot{S}_{LON} > \delta \end{cases} \tag{C.2.5}$$

where

F_{BREAK}	breakout force level
δ	linear viscous half-bandwidth

C.2.2 Lateral Suspension Model

The lateral suspension force-deflection characteristic consists of a three-stage spring in parallel with Coulomb friction. The latter is represented by the linear viscous band model, which has a highly viscous region for low stroke rates and a breakout level for high stroke rates.

$$F_{LAT} = F_{STIFF} + F_{DAMP} \tag{C.2.6}$$

For suspensions 1 and 4, F_{STIFF} is calculated as follows:

$$\begin{aligned} F_{STIFF} = {} & K_{LAT} \cdot S_{LAT} \\ & + (K_{STPLA} - K_{LAT}) \cdot (\max(S_{LAT}, L_{STOP1}) - L_{STOP1}) \\ & + (K_{STRUC} - K_{STPLA}) \cdot (\max(S_{LAT}, L_{STOP2}) - L_{STOP2}) \end{aligned} \tag{C.2.7}$$

For suspensions 2 and 3, F_{STIFF} is calculated as follows:

$$\begin{aligned} F_{STIFF} = {} & K_{LAT} \cdot S_{LAT} \\ & + (K_{STPLA} - K_{LAT}) \cdot (\min(S_{LAT}, -L_{STOP1}) + L_{STOP1}) \\ & + (K_{STRUC} - K_{STPLA}) \cdot (\min(S_{LAT}, -L_{STOP2}) + L_{STOP2}) \end{aligned} \tag{C.2.8}$$

where

S_{LAT}	lateral suspension stroke
K_{LAT}	first stage stiffness
L_{STOP1}	clearance for second stage stiffness
K_{STPLA}	second stage stiffness
L_{STOP2}	clearance for third stage stiffness
K_{STRUC}	third stage (structural) stiffness

The damping force, modeled with the linear viscous band approximation to the Coulomb friction characteristic, is given as follows:

$$F_{DAMP} = \begin{cases} -F_{BREAK} & \text{if } \dot{S}_{LAT} < -\delta \\ (\dot{S}_{LAT}/\delta)F_{BREAK} & \text{if } -\delta < \dot{S}_{LAT} < \delta \\ F_{BREAK} & \text{if } \dot{S}_{LAT} > \delta \end{cases} \tag{C.2.9}$$

where

$\dot{S}_{LAT}$	lateral suspension stroke rate
F_{BREAK}	breakout force level
δ	linear viscous half-bandwidth

C.2.3 Vertical Suspension Model

The vertical suspension consists of a leaf spring, which is represented using a technique initially developed for truck suspensions. This method was first developed by Fancher, Ervin, MacAdam, and Winkler [14]. It has been modified by O'Connell [18] who found that the use of the current envelope characteristic evaluated at the previous displacement, $F^i_{ENV}(\delta_{i-1})$, eliminated a ramp-following error observed in experimental measurements.

$$\begin{aligned} F_{VER}(t_i) &= F^i_{ENV}(\delta_i) \\ &+ \left(F_{VER}(t_{i-1}) - F^i_{ENV}(\delta_{i-1})\right) \cdot \exp\left(-\frac{|S_{VER}(t_i) - S_{VER}(t_{i-1})|}{\beta}\right) \end{aligned} \tag{C.2.10}$$

where

$F_{VER}(t_i)$	suspension force, current timestep
$F_{VER}(t_{i-1})$	suspension force, previous timestep
$S_{VER}(t_i)$	suspension stroke, current timestep
$S_{VER}(t_{i-1})$	suspension stroke, previous timestep

$F^i_{ENV}(\delta_i)$	force for current envelope, at current displacement
$F^i_{ENV}(\delta_{i-1})$	force for current envelope, at previous displacement
β	"beta" parameter which describes the rate at which suspension force within hysteresis loop approaches envelope

The envelope force depends upon whether the leafspring is undergoing compression or extension, which is determined by comparing the current stroke with that saved from the previous timestep, as follows:

$$\begin{aligned}
&If \quad S_{VER,i} > S_{VER,i-1}: \\
&\quad F_{ENV} = C_1 \cdot S_{VER} + C_2 \\
&\qquad\qquad + \left(\max(S_{VER}, C_{HGSTR1}) - C_{HGSTR1}\right) \cdot (C_3 - C_1) \\
&ElseIf \quad S_{VER,i} \leq S_{VERi-1}: \\
&\quad F_{ENV} = C_1 \cdot S_{VER} + C_6 \\
&\qquad\qquad + \left(\max(S_{VER}, C_{HGSTR2}) - C_{HGSTR2}\right) \cdot (C_7 - C_1)
\end{aligned} \tag{C.2.11}$$

where

C_1	first stage leaf spring stiffness
C_{HGSTR1}	computed value of S_{VER} at which F_{VER} equals C_5 for increasing S_{VER}
C_5	value of F_{VER} for which leaf spring reaches the second stage stiffness
C_3	second stage leaf spring stiffness for increasing S_{VER}
C_2	Coulomb friction force for increasing S_{VER}
C_{HGSTR2}	computed value of S_{VER} at which F_{VER} equals C_5 for decreasing S_{VER}
C_7	second stage leaf spring stiffness for decreasing S_{VER}
C_6	Coulomb friction force for decreasing S_{VER}

C.3 Suspension Force and Moment Equations

In this section, the total forces and moments applied to the carbody and wheelsets are developed. The convention used here is that $F_{Q,Y}$, $F_{Q,Z}$, $M_{Q,X}$, $M_{Q,Y}$, and $M_{Q,Z}$ are the forces and moments acting on the body Q, where Q may be C for the carbody or $W1$ or $W2$ for the first and second wheelsets. The terms Ω_{LB}, Ω_{VB}, and Ω_{TW} are used to represent the lateral bending, vertical bending, and twisting moment loads.

C.3.1 Forces and Moments Acting on the Wheelsets

The net lateral and vertical forces, as well as the roll and yaw moments, resulting from the above suspension forces are presented below. Results are given first for the leading wheelset, then for the trailing wheelset.

Leading Wheelset (C.3.1)

$$
\begin{aligned}
F_{W1,Y} &= -F_{LAT1} - F_{LAT2} \\
F_{W1,Z} &= -F_{VER1} - F_{VER2} \\
M_{W1,X} &= -H_{AFAX1} \cdot F_{VER1} + H_{AFAX2} \cdot F_{VER2} \\
M_{W1,Z} &= H_{AFAX1} \cdot F_{LON1} - H_{AFAX2} \cdot F_{LON2}
\end{aligned}
$$

Trailing Wheelset (C.3.2)

$$
\begin{aligned}
F_{W2,Y} &= -F_{LAT3} - F_{LAT4} \\
F_{W2,Z} &= -F_{VER3} - F_{VER4} \\
M_{W2,X} &= -H_{AFAX4} \cdot F_{VER4} + H_{AFAX3} \cdot F_{VER3} \\
M_{W2,Z} &= -H_{AFAX3} \cdot F_{LON3} + H_{AFAX4} \cdot F_{LON4}
\end{aligned}
$$

C.3.2 Forces and Moments Acting on the Carbody

The suspension forces give rise to both rigid body and flexible body forces and moments. First, the total lateral and vertical forces acting on the carbody are given as follows:

Car Rigid Body Forces (C.3.3)

Lateral Force

$$F_{C,Y} = F_{LAT1} + F_{LAT2} + F_{LAT3} + F_{LAT4}$$

Vertical Force

$$F_{C,Z} = F_{VER1} + F_{VER2} + F_{VER3} + F_{VER4}$$

The rigid body moments are found in the usual manner by considering the effective moment arms about the center of gravity for each contributing force.

Car Rigid Body Moments (C.3.4)

Roll Moment

$$
\begin{aligned}
M_{C,X} = {} & V_{ERCOG1} \cdot F_{LAT1} + V_{ERCOG2} \cdot F_{LAT2} \\
& + V_{ERCOG3} \cdot F_{LAT3} + V_{ERCOG4} \cdot F_{LAT4} \\
& + (H_{AFAX1} + V_{ERCOG1} \cdot \phi_C + S_{LAT1}) \cdot F_{VER1} \\
& + (-H_{AFAX2} + V_{ERCOG2} \cdot \phi_C + S_{LAT2}) \cdot F_{VER2} \\
& + (-H_{AFAX3} + V_{ERCOG3} \cdot \phi_C + S_{LAT3}) \cdot F_{VER3} \\
& + (H_{AFAX4} + V_{ERCOG4} \cdot \phi_C + S_{LAT4}) \cdot F_{VER4}
\end{aligned}
$$

Pitch Moment

$$
\begin{aligned}
M_{C,Y} = {} & - A_{XDIST1} \cdot F_{VER1} - A_{XDIST2} \cdot F_{VER2} \\
& + A_{XDIST3} \cdot F_{VER3} + A_{XDIST4} \cdot F_{VER4}
\end{aligned}
$$

Yaw Moment

$$
\begin{aligned}
M_{C,Z} = {} & A_{XDIST1} \cdot F_{LAT1} - H_{AFAX1} \cdot F_{LON1} \\
& + A_{XDIST2} \cdot F_{LAT2} + H_{AFAX2} \cdot F_{LON2} \\
& - A_{XDIST3} \cdot F_{LAT3} + H_{AFAX3} \cdot F_{LON3} \\
& - A_{XDIST4} \cdot F_{LAT4} - H_{AFAX4} \cdot F_{LON4}
\end{aligned}
$$

The forces and moments for the three bending modes are generated by considering each contributing force and the value of the corresponding mode shape at each connection location. The results are as follows:

Car Flexible Body Forces and Moments (C.3.5)

Vertical Bending

$$\Omega_{VB} = M_{ODVB1} \cdot F_{VER1} + M_{ODVB2} \cdot F_{VER2} + M_{ODVB3} \cdot F_{VER3} + M_{ODVB4} \cdot F_{VER4}$$

Lateral Bending

$$\Omega_{LB} = M_{ODLB1} \cdot F_{LAT1} + M_{ODLB2} \cdot F_{LAT2} + M_{ODLB3} \cdot F_{LAT3} + M_{ODLB4} \cdot F_{LAT4}$$

Longitudinal Twist

$$\begin{aligned}\Omega_{TW} = {} & M_{ODTW1} \cdot [F_{VER1} \cdot H_{AFAX1} + F_{LAT1} \cdot V_{ERCOG1}] \\ & + M_{ODTW2} \cdot [-F_{VER2} \cdot H_{AFAX2} + F_{LAT2} \cdot V_{ERCOG2}] \\ & + M_{ODTW3} \cdot [-F_{VER3} \cdot H_{AFAX3} + F_{LAT3} \cdot V_{ERCOG3}] \\ & + M_{ODTW4} \cdot [F_{VER4} \cdot H_{AFAX4} + F_{LAT4} \cdot V_{ERCOG4}]\end{aligned}$$

C.4 Carbody State Equations

The analysis in Appendix A may be used to develop the carbody dynamic equations of motion, using the applied suspension forces and moments considered above. In the following, for the flexible modes ς, d is the carbody structural damping ratio, and w is the carbody fundamental natural frequency.

Car Rigid Body Equations (C.4.1)

Lateral Equation

$$m_c(\check{y}_C - ro_c\check{\phi}_{SE}) = -m_c g\phi_{SE} + m_c V^2\rho + F_{C,Y}$$

Vertical Equation

$$m_c(\check{z}_C + a\check{\phi}_{SE}) = -m_c g - m_c V^2\rho\phi_{SE} + F_{C,Z}$$

Roll Equation

$$I_{CX}(\check{\phi}_C + \check{\phi}_{SE}) = (I_{CY} - I_{CZ})\dot{\theta}_C(\dot{\psi}_C - V\rho) + M_{C,X}$$

Pitch Equation

$$I_{CY}\check{\theta}_C = (I_{CZ} - I_{CX})(\dot{\phi}_C + \dot{\phi}_{SE})(\dot{\psi}_C - V\rho) + M_{C,Y}$$

Yaw Equation

$$I_{CZ}(\check{\psi}_C - V\dot{\rho}) = (I_{CX} - I_{CY})\dot{\theta}_C(\dot{\phi}_C + \dot{\phi}_{SE}) + M_{C,Z}$$

Car Flexible Body Equations (C.4.2)

Vertical Bend Equation

$$m_c \ddot{\varsigma}_Y + 2 d_y w_y m_c \dot{\varsigma}_Y + {w_y}^2 m_c \varsigma_Y = \Omega_{VB}$$

Lateral Bend Equation

$$m_c \ddot{\varsigma}_Z + 2 d_z w_z m_c \dot{\varsigma}_Z + {w_z}^2 m_c \varsigma_Z = \Omega_{LB}$$

Longitudinal Twist Equation

$$I_{CX} \ddot{\varsigma}_X + 2 d_x w_x I_{CX} \dot{\varsigma}_X + {w_x}^2 I_{CX} \varsigma_X = \Omega_{TW}$$

Appendix D

Model Parameters

D.1 Vehicle Parameters

The parameters chosen to represent the unloaded two-axle vehicle are listed below. Most of these result from vehicle and truck characterization tests performed on a prototype vehicle at the Transportation Test Center, Pueblo, CO.

D.1.1 Inertial Parameters

$m_c g$ = car weight = 21520.0 lbf

I_{CX} = car x mass moment of inertia = 3.70E04 lbf-in-sec**2

I_{CY} = car y mass moment of inertia = 2.50E06 lbf-in-sec**2

I_{CZ} = car z mass moment of inertia = 2.25E06 lbf-in-sec**2

$m_w g$ = wheelset weight = 2222.0 lbf

I_{WX} = wheelset x mass moment of inertia = 2600.0 lbf-in-sec**2

I_{WY} = wheelset x mass moment of inertia = 1500.0 lbf-in-sec**2

g = gravitational acceleration = 386.04 in/sec**2

D.1.2 Geometric Parameters

VERCOG(1,2,3,4) = 16.0 in

AXDIST(1,2) = 224.3 in

AXDIST(3,4) = 213.7 in

HAFAX(1,2,3,4) = 39.0 in

RADIUS = wheel nominal rolling radius = 14.0 in

ROW = distance from track CS origin to wheelset cg = 14.0 in

ROC = distance from track CS origin to car cg = 30.0 in

HAFGAG = track half gauge = 29.75 in

RAILEN = nominal rail length = 39.0 ft

D.1.3 Structural Parameters

DAMPVB = car vertical bending modal damping ratio = .1

DAMPLB = car lateral bending modal damping ratio = .1

DAMPTW = car longitudinal twist modal damping ratio = .15

NATVB = car vertical bending natural frequency = 56.5 rad/s

NATLB = car lateral bending natural frequency = 55.0 rad/s

NATTW = car longitudinal twist natural frequency = 45.9 rad/s

D.1.4 Longitudinal Suspension

KLON1 = longitudinal swing stiffness = 789.0 lbf/in

LONSTP = longitudinal clearance = .875 in

KSTOP = longitudinal axle guard stiffness = 1.0E06 lbf/in

LTHLNK = nominal full swing link length = 12.6 in

LONCOU = longitudinal Coulomb friction = 200 lbf

LONBRK = linear viscous half-bandwidth = 0.5 in/sec

KBUSH = bushing stiffness = 20000 lbf/in

VSC(1,2,3,4) = yaw damper velocity = .020, 0.21, 0.663, 1.18 in/sec

FSC(1,2,3,4) = yaw damper force = 220, 310, 1200, 2023 lbf

D.1.5 Lateral Suspension

KLAT = lateral first stage stiffness = 498.2 lbf/in

LTHLAT = nominal lateral swing link length = 10.8 in

LSTOP1 = first stop = .97 in

KSTPLA = lateral second stage stiffness = 9600.0 lbf/in

LSTOP2 = second stop = 1.21 in

KSTRUC = lateral third stage stiffness = 23500.0 lbf/in

LATCOU = lateral Coulomb friction (FCOEFF*WGTCAR/4) = 390 lbf

LATBRK = linear viscous half-bandwidth = .06 in/sec

D.1.6 Vertical Suspension

CON(1) = 4020.0 lbf/in

CON(2) = 600 lbf

CON(3) = 15400.0 lbf/in

CON(4) (beta, compression) = .05

CON(5) = 10000.0 lbf

CON(6) = -600 lbf

CON(7) = 12000 lbf/in

CON(8) (beta, extension) = .05

D.2 Wheel / Rail and Track Parameters

The parameters affecting wheel/rail interactions include both the wheel/rail contact geometry and the track system inputs. The wheel/rail contact geometry is discussed in Chapter 2, where several different profiles are illustrated and their effects on system response is discussed.

Measured track data is used for the perturbed track analysis for those instances in which the data was available. This data was obtained from the Test Center and processed with the MIT "TRACK" program, which analyzes the data to generate coefficients for cubic splines. The output file of coefficients may then be read by the simulation program, using special software, in order to represent the actual measured track. This procedure has been done for several sections of track.

Table D.1 lists the vehicle test, the measured track data filename for that test, and the wheel/rail geometry filename used in the analysis. Note also that the nominal wheel/rail friction coefficient is $\mu = 0.5$.

Table D.1

Profile and Track Data for Simulations

Test	Track Data	Wheel/Rail Profile
Hunting	(none)	CNH136S.WRX
Curving (5 deg)	(none)	F5DEG.WRX (Front) R5DEG.WRX (Rear)
Curving (7.5 deg)	(none)	F5DEG.WRX (Front) R5DEG.WRX (Rear)
Curving (10 deg)	(none)	F10DEG.WRX (Front) R10DEG.WRX (Rear)
Yaw-Sway	PTTLAT.COF	FYAWSWAY.WRX (Front) RYAWSWAY.WRX (Rear)
Dynamic Curving	XNORTHY.COF	CNH136S.WRX
Roll-Twist	PTTRKRLL.COF	CNH136S.WRX
Bounce	PTTBOUNC.COF	CNH136S.WRX
Vertical Bump	(analytical)	CNH136S.WRX

A Comparison of Model and Field Test Dynamic Performance Data for a Two-Axle Freight Car, 1989
US DOT, FRA, DN Wormley, JR Bailey